

## Interactions between parallel carbon nanotube quantum dots

Karin Goß





Forschungszentrum Jülich GmbH  
Peter Grünberg Institut (PGI)  
Elektronische Eigenschaften (PGI-6)

# **Interactions between parallel carbon nanotube quantum dots**

Karin Goß



Bibliographic information published by the Deutsche Nationalbibliothek.  
The Deutsche Nationalbibliothek lists this publication in the Deutsche  
Nationalbibliografie; detailed bibliographic data are available in the  
Internet at <http://dnb.d-nb.de>.

Publisher and  
Distributor: Forschungszentrum Jülich GmbH  
Zentralbibliothek  
52425 Jülich  
Phone +49 (0) 24 61 61-53 68 · Fax +49 (0) 24 61 61-61 03  
e-mail: [zb-publikation@fz-juelich.de](mailto:zb-publikation@fz-juelich.de)  
Internet: <http://www.fz-juelich.de/zb>

Cover Design: Grafische Medien, Forschungszentrum Jülich GmbH

Printer: Grafische Medien, Forschungszentrum Jülich GmbH

Copyright: Forschungszentrum Jülich 2011

Schriften des Forschungszentrums Jülich  
Reihe Schlüsseltechnologien / Key Technologies Band / Volume 30

D 464 (Diss., Duisburg, Univ., 2011)

ISSN 1866-1807

ISBN 978-3-89336-740-5

The complete volume is freely available on the Internet on the Jülicher Open Access Server (JUWEL) at  
<http://www.fz-juelich.de/zb/juwel>

Neither this book nor any part of it may be reproduced or transmitted in any form or by any  
means, electronic or mechanical, including photocopying, microfilming, and recording, or by any  
information storage and retrieval system, without permission in writing from the publisher.

## Zusammenfassung

Das Thema dieser Dissertation sind molekulare Wechselwirkungen, untersucht am Beispiel von parallelen Quantenpunkten, die sich in den einzelnen Fasern eines sogenannten Seils von Kohlenstoff-Nanoröhren bilden. Auf dem Gebiet der molekularen Elektronik bieten Kohlenstoff-Nanoröhren eine Vielfalt an makromolekularen Strukturen und bei deren Kombination zu Seilen auch ein generisches System zur Untersuchung von molekularen Wechselwirkungen.

Zu Anfang wird die Struktur des kontaktierten Seils mit spitzenverstärkter Raman Spektroskopie (TERS) charakterisiert. Wir beobachten einen deutlichen Resonanzeffekt für den Raman Streuprozess, der bisher in der Literatur zu TERS an Kohlenstoff-Nanoröhren nicht untersucht wurde. Durch Bestimmung des Durchmessers, der Metallizität und der Chiralität werden sieben Nanoröhren innerhalb des Seils identifiziert. Eine Rotverschiebung der optischen Übergangsenergien wird den Wechselwirkungen zwischen den Fasern zugeschrieben.

In Quantentransport-Messungen stellt sich heraus, dass die Nanoröhren wechselwirkende, parallele Quantenpunkte bilden. Im Rahmen von *master equations* wird ein Modell aus parallelen, kapazitiv- und tunnel-gekoppelten Quantenpunkten entwickelt um den Transport durch das System zu beschreiben. Anhand ihrer Wechselwirkungen werden sieben parallele Quantenpunkte charakterisiert. Die meisten davon sind asymmetrisch kontaktiert, einhergehend mit unterschiedlichen Kopplungseigenschaften, die aus der TERS-Charakterisierung erwartet werden. Zusätzlich ist die Kopplung zur Gatter-Elektrode stark verschieden für einzelne Quantenpunkte. Dies ermöglicht es verschiedene Konfigurationen des Systems gezielt anzufahren und selektiv Elektronen zu bestimmten Fasern des Seils hinzuzufügen. Diesen differentiellen Gatter-Effekt nutzend kann die Stärke der molekularen Wechselwirkungen untersucht werden. Dabei sehen wir, dass einzelne Fasern innerhalb desselben Seils äußerst verschieden miteinander wechselwirken können. Unter den Quantenpunkten, die eine stärkere Wechselwirkung zeigen als bisher angenommen, finden wir auch welche, die nur kapazitiv gekoppelt oder vollständig ungekoppelt sind.

Die Tunnel-Kopplung ist eine Hybridisierung von Quantenpunkt-Zuständen, die prinzipiell aus den Molekülorbitalen bestehen. Im Speziellen enthält das Vorzeichen der Hybridisierung Informationen über die beteiligten Wellenfunktionen. Dabei findet sich in unserem Fall ein negatives Vorzeichen, was auf den Überlapp von Wellenfunktionen mit gleichem Vorzeichen deutet. Die Hybridisierung kann durch ein angelegtes Magnetfeld beeinflusst werden und in der Folge durch Spin-Effekte auch selektiv unterdrückt werden. In diesem Fall ermöglicht es der differentielle Gatter-Effekt bestimmte Spin-Konfigurationen des Systems einzustellen.

Zusammenfassend wird ein Quanten-Bauteil vorgestellt, das die Möglichkeit bietet molekulare Wechselwirkungen mithilfe von Quantentransport-Spektroskopie zu untersuchen. Die zusätzliche Charakterisierung durch TERS stellt eine neuartige Kombination aus zwei experimentellen Methoden mit großem Potential auf dem Gebiet der molekularen Elektronik dar.



## Abstract

The subject of this thesis is molecular interactions which are investigated using the example of parallel quantum dots formed in the individual strands of a carbon nanotube rope. For molecular electronics, carbon nanotubes offer a variety of macromolecular structures and by combining several nanotubes into a rope, also a generic system to probe molecular interactions.

First, the structure of the contacted rope is characterized by tip-enhanced Raman spectroscopy (TERS). We observe a clear resonance effect for the Raman scattering process, which is up to now not considered in the literature on TERS of carbon nanotubes. By extracting the diameter, metallicity and chirality, seven carbon nanotubes within the rope are identified. A redshift of their optical transition energies is attributed to interactions between the strands.

In quantum transport measurements, the nanotubes are found to form interacting parallel quantum dots. Within the framework of master equations, a model is developed to describe the transport via the quantum dot system, where the parallel dots are capacitively and tunnel coupled. Employing this model, seven parallel quantum dots are characterized by their interactions. Along with changing interface properties predicted by the TERS characterization, the coupling to the two contacts is very asymmetric for most of the quantum dots. Additionally, the coupling to the gate electrode is found to vary strongly for individual dots, allowing one to tune the quantum dot system into different configurations and selectively add electrons to individual strands of the rope. Exploiting this differential gating effect, the magnitude of the molecular interactions can be investigated. Here, we find that individual strands within one carbon nanotube rope can interact very distinctly. Amongst the coupled quantum dots with a coupling stronger than previously assumed, we also find only capacitively interacting or completely uncoupled quantum dots within the one device.

The tunnel coupling is a hybridization of quantum dot states which, in principle, are comprised of the molecular orbitals. In particular, the sign of the hybridization amplitude contains information about the involved wavefunctions, where we always find a negative amplitude denoting the overlap of wavefunctions with the same sign. The hybridization can be manipulated by an applied magnetic field and hence selectively suppressed due to spin effects. Here, the differential gating allows for tuning to distinct spin configurations of the quantum dot system.

In conclusion, we demonstrate a tunable quantum device which provides the possibility of probing molecular interactions by quantum transport spectroscopy. The additional characterization using TERS represents a novel combination of two experimental techniques with great potential in the field of molecular electronics.



# Contents

<b>1</b>	<b>Introduction</b>	<b>1</b>
<b>2</b>	<b>Introduction to carbon nanotubes</b>	<b>5</b>
2.1	Atomic structure . . . . .	5
2.2	The electronic band structure . . . . .	8
2.2.1	The zone-folding approximation . . . . .	10
2.2.2	Electronic transport properties . . . . .	10
2.2.3	Optical transition energies . . . . .	13
2.3	The phonon band structure . . . . .	15
2.3.1	Raman scattering . . . . .	15
2.3.2	A carbon nanotube Raman spectrum . . . . .	17
2.4	Conclusions . . . . .	23
<b>3</b>	<b>Tip-enhanced Raman spectroscopy on a contacted carbon nanotube rope</b>	<b>25</b>
3.1	Tip-enhanced Raman spectroscopy (TERS) . . . . .	26
3.1.1	The principles of TERS . . . . .	26
3.1.2	Experimental setup . . . . .	28
3.2	Device fabrication . . . . .	28
3.2.1	Carbon nanotube growth . . . . .	29
3.2.2	Electron beam lithography . . . . .	30
3.2.3	Process steps . . . . .	32
3.3	TERS on a contacted carbon nanotube rope . . . . .	32
3.3.1	Signal enhancement due to a metal tip . . . . .	33
3.3.2	Identifying individual strands of the nanotube rope . . . . .	35
3.3.3	Chiral index assignment . . . . .	39
3.3.4	Monitoring structural changes of the rope . . . . .	43
3.4	Conclusions . . . . .	44
<b>4</b>	<b>Single electron transport in carbon nanotube quantum dots</b>	<b>47</b>
4.1	Introduction to quantum dots . . . . .	47
4.1.1	The constant interaction model . . . . .	48

## CONTENTS

---

4.1.2	Linear transport and Coulomb blockade . . . . .	50
4.1.3	Non-linear transport – the stability diagram . . . . .	51
4.2	Carbon nanotubes as quantum dots . . . . .	53
4.3	Model of interacting parallel quantum dots . . . . .	56
4.3.1	Master equation modeling . . . . .	56
4.3.2	Transport via interacting parallel quantum dots . . . . .	58
4.3.3	The differential gating effect . . . . .	61
4.4	Conclusions . . . . .	62
<b>5</b>	<b>Electronic setup for quantum transport measurements</b>	<b>65</b>
5.1	Electrical characterization at room temperature . . . . .	65
5.2	Low-temperature electrical transport setup . . . . .	66
5.2.1	Device cooling . . . . .	66
5.2.2	Measurement electronics and filtering . . . . .	67
<b>6</b>	<b>Interacting parallel quantum dots in a carbon nanotube rope</b>	<b>73</b>
6.1	Parallel carbon nanotube quantum dots . . . . .	75
6.2	Quantum transport spectroscopy of carbon nanotube interactions . .	78
6.3	Shifting the potential of the main dot states . . . . .	83
6.4	Conclusions . . . . .	86
<b>7</b>	<b>Hybridization between quantum dot states</b>	<b>89</b>
7.1	The hybridization phase . . . . .	89
7.2	Spin-dependent hybridization . . . . .	92
7.3	Conclusions . . . . .	95
<b>8</b>	<b>Conclusions and Outlook</b>	<b>97</b>
	<b>Appendix</b>	<b>101</b>
A	Supplementary information for Raman spectroscopy . . . . .	101
B	Supplementary information for the device fabrication . . . . .	105
	<b>Bibliography</b>	<b>107</b>
	<b>List of Figures</b>	<b>127</b>
	<b>List of Tables</b>	<b>129</b>
	<b>List of Own Publications</b>	<b>131</b>
	<b>Acknowledgements</b>	<b>137</b>
	<b>Curriculum Vitae</b>	<b>139</b>

# 1 Introduction

The emerging fields of molecular electronics and spintronics aim at exploiting the chemical versatility of molecules to control charge and spin transport in nanoscale devices [Nitzan03, Bogani08, Tao06]. Molecules can be tailored to have desired optical, magnetic, electronic or electromechanical properties. Molecular electronics is expected to yield a large variety of new devices and applications, extending the performance that could possibly be achieved with conventional materials. Additionally, their intrinsically small size is a major advantage for an application in information technology, where the scalability of devices to nanometer sizes is a key issue.

Fabrication of molecular structures in junctions, especially single-molecule devices, controlled by electric and magnetic fields, however, is a challenging task [Park99, Ghosh05] and needs approaches different from the conventional fabrication of semiconductor devices. One major issue is the pronounced sensitivity of molecular structures to interactions with the environment influencing the transport properties. Fundamental aspects of single-molecule devices require an understanding of strong perturbations caused by environmental effects, such as the interaction with the substrate, contacts or neighbouring molecules [Osorio07, Osorio10, Kaasbjerg08].

Carbon nanotubes can provide a useful link between well-studied low-temperature transport in semiconductors and expected new phenomena in electronic devices based on single molecules. Nanotubes can be considered as organic macromolecules with versatile chemical properties. They form hollow cylinders composed of solely carbon atoms arranged in a hexagonal lattice. They have been first synthesized and imaged by Iijima [Iijima91], and found to exhibit outstanding mechanical and electronic properties. The bonds between the  $sp^2$ -hybridized carbon atoms make the nanotubes mechanically stronger than steel [Walters99]. At the same time, carbon nanotubes are of very light weight. The excellent flexibility perpendicular to the tube axis makes them interesting as nanoprobe in scanning probe microscopes [Dai96]. Owing to their quasi-one-dimensional nature, they exhibit very specific electronic behaviour due to the presence of van Hove singularities in the density of states, such as ballistic electron transport [Kong01, Liang01]. Current densities supported by carbon nanotubes exceed values of copper [Yao00, Wei01], which makes them promising as interconnects in electrical circuits [Talapatra06, Yokoyama07, Esconjauregui10].



The properties of carbon nanotubes can be further tuned by adding new components, which is done by chemical functionalization. For instance, the inner hollow of carbon nanotubes can be filled with fullerene molecules resulting in so-called peapods [Smith98, Sloan00]. Using metallofullerenes with a metal dopant inside the fullerene cage is of fundamental interest for the possibility to investigate one-dimensional spin chains [Benjamin06, Cantone08]. However, it is still not clearly understood, how empty  $C_{60}$  fullerenes influence the transport properties of a carbon nanotube [Shimada02, Utko06, Quay07, Eliassen10], therefore requiring detailed theoretical and experimental studies involving molecular interactions.

Similar to the delocalized  $\pi$ -electron system of carbon nanotubes, smaller molecules of interest for electronic transport contain in many cases a  $\pi$ -conjugated part [Tao06]. This similarity initiates the idea to fabricate molecular junctions involving carbon nanotubes as contacts to the molecules [Guo06, Guo07, Guo09]. Using metallic nanotubes as contacts, one expects good conduction from the  $\pi$ -bonded network of the nanotube to the  $\pi$ -bonded molecular orbital of the conjugated molecule [Ke07].

In the context of all the mentioned complex assemblies of molecules in junctions, nanotubes represent an ideal playground to investigate molecular interactions. Especially, carbon nanotubes bundled together in form of a rope represent a generic and readily available system to study the interactions between molecules. The subject of this work is the investigation of molecular interactions in a carbon nanotube rope device. The presented results gain substantial importance by a joint interpretation of data obtained by two independent measurement techniques.

Low-temperature transport experiments are sensitive to potential variations on the sub-meV scale, allowing the study of interactions between coupled nanoscale conductors. In this work, the carbon nanotubes in a rope are found to form parallel quantum dots interacting by a capacitive and a tunneling coupling exhibiting very different strength. The arbitrary combination of carbon nanotubes of various types represents a very general molecular transport device and the conclusions drawn here from the carbon nanotube example can readily be transferred to molecules of any other kind. Spotlighting deviations from an expected behaviour in quantum transport, this work reveals interactions in molecular systems, thereby contributing to a more detailed understanding of the transport properties of complex multi-molecular systems. The results may trigger a crucial awareness for the transport features in future studies on functionalized carbon nanotubes and other molecules.

Considering complex molecular transport devices and the issues concerning their assembly, an additional characterization of the devices becomes mandatory. For the identification and structural characterization of molecules embedded in a transport device, we use Raman spectroscopy – a powerful technique having at present a strong impact on carbon nanotube research [Reich04, Dresselhaus05]. Optical and electronic properties can be probed even at the single carbon nanotube level [Meyer05, Débarre08, Fouquet09] and are sensitive to interactions between adja-

---

cent nanotubes in a rope as well as to environmental effects [Henrard99, Fantini04, O’Connell04, Araujo08]. More precisely, we employ a more recently developed near-field technique of Raman spectroscopy – tip-enhanced Raman spectroscopy (TERS) [Hartschuh03, Hartschuh08, Cançado09a], which is perfectly suitable for the characterization of single-molecule junctions. It involves a Raman signal enhancement at a metallic tip and provides a spatial resolution of down to several nanometers [Anderson05].

The presented novel combination of tip-enhanced Raman spectroscopy and low-temperature electronic transport measurements performed on the very same molecular quantum dot device represents an ideal characterization concept for single-molecule transport devices. It presents an important step to understand interactions between molecules from the viewpoint of quantum transport while their molecular origin is unambiguously determined by the additional characterization.

The outline of the thesis is as follows:

**Chapter 2** introduces carbon nanotubes and explains their basic properties on the basis of the physical properties of graphene. Special emphasis is laid on the discussion of optical and vibrational properties that can be probed by Raman spectroscopy.

**Chapter 3** continues the topic of Raman scattering by explaining the principles of tip-enhanced Raman spectroscopy. In addition, it briefly explains the fabrication process of carbon nanotube devices structured for low-temperature transport measurements. The main part of the chapter presents experimental results obtained by TERS on a contacted carbon nanotube rope. The thorough characterization of the device includes a diameter evaluation, a chirality assignment and the monitoring of structural changes along the rope. This information forms the basis for interpreting the electronic transport through the device in later chapters.

In **chapter 4**, quantum transport will be explained starting from the basic constant interaction model and carrying on with the characteristic features of carbon nanotube quantum dots. Furthermore, a model of two interacting parallel quantum dots is developed within the framework of master equation modeling. The manifestations of the tunnel coupling and the capacitive coupling in the stability diagram of the quantum dot system are investigated and discussed using transport calculations.

**Chapter 5** introduces the electronic setup for low-temperature transport measurements and improvements thereon which were accomplished within the framework of this thesis.

The subsequent **chapter 6** presents quantum transport measurements on the same carbon nanotube rope device which was characterized in chapter 3 by Raman spectroscopy. The interactions between parallel quantum dots formed in the strands of the rope are examined employing the model from chapter 4.

**Chapter 7** is focused on the tunnel coupling, i.e., the electronic hybridization between quantum dot states. The phase and the spin-dependence of the hybridization is discussed.

The last **chapter 8** summarizes the results of this thesis and gives an outlook towards future experiments and possible interesting investigations.

The **Appendix** contains supplementary information on the device fabrication process and the evaluation of Raman spectra.

## 2 Introduction to carbon nanotubes

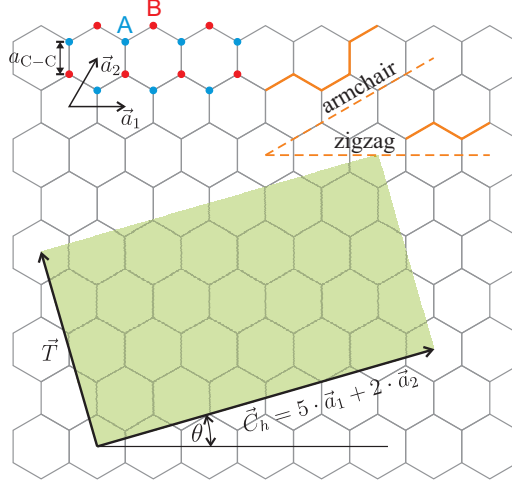
Carbon nanotubes are ideal one-dimensional conductors exhibiting ballistic transport – a property inherited from graphene which is the basic atomic lattice from which nanotubes are constructed. As such, they are perfectly suitable to be structured as quantum dots. Properties of carbon nanotube quantum dots are often compared to those of semiconductor quantum dots and models developed for these systems generally can be applied in a similar manner. On the other hand, carbon nanotubes offer a large variety of molecular structures. In contrast to the buried structures in III/V semiconductor quantum dots, nanotubes can interact with their environment, which is a key issue in molecular electronics. Thus, carbon nanotubes can be used to study molecular interactions and bridge the gap between semiconductor and single molecule quantum dots.

In order to understand the molecular properties of carbon nanotubes, this chapter gives an introduction to the basic properties of carbon nanotubes and how they can be characterized by Raman spectroscopy. In the beginning, the atomic structure of nanotubes is derived starting from a graphene lattice. Doing so, a variety of different families of carbon nanotubes can be defined, depending on the chirality of a nanotube. Next, the electronic band structure of nanotubes is derived from the graphene band structure and electrical transport phenomena occurring in nanotubes are discussed on the basis of this derivation. In the last section of the chapter, we discuss the phonon band structure and introduce Raman scattering as a tool to investigate the vibrational properties of carbon nanotubes. Therein, special emphasis is laid on the discussion of the diameter-dependent Raman modes, in order to provide a solid basis for the interpretation of the experimental data in chapter 3.

### 2.1 Atomic structure

A carbon nanotube (CNT) can be thought of as a graphene sheet – a single graphitic layer – being rolled up to form a tubular structure [Reich04]. The carbon atoms in graphene are arranged in a hexagonal lattice, where each atom has three nearest

**Figure 2.1:** Lattice structure of graphene with unit vectors  $\vec{a}_1$  and  $\vec{a}_2$ . The armchair and zigzag line is indicated. To obtain a carbon nanotube, the graphene sheet is rolled up, so that the start and the end of the chiral vector  $\vec{C}_h$  meet.  $\vec{C}_h$  and the vector  $\vec{T}$  pointing along the tube axis define the unit cell of the nanotube, in this case a (5, 2) nanotube.



neighbours with an interatomic distance of  $a_{C-C} = 1.421\text{\AA}$ . The  $sp^2$ -hybridized orbitals of the carbon atoms form  $\sigma$ -bonds, while the unhybridized  $p_z$ -orbitals form  $\pi$ -bonds with delocalized electrons, which are responsible for the unique electronic properties of graphene as will be discussed later. The unit cell is spanned by the unit vectors  $\vec{a}_1$  and  $\vec{a}_2$  and has a two-atomic basis. The C atoms are located on two different triangular sublattices labelled A and B in Fig. 2.1. In order to result in a seamless cylinder of a carbon nanotube, the graphene sheet has to be rolled up in such a way, that the circumference can be represented by a vector  $\vec{C}_h = n\vec{a}_1 + m\vec{a}_2$  called chiral vector, where the chiral indices  $n, m \geq 0$  are integers. The resulting nanotubes are categorized in armchair, zigzag or chiral carbon nanotubes. The first two categories are named after the armchair- or zigzag-like pattern of carbon atoms along their chiral vector. To obtain an armchair nanotube,  $n = m$  has to be fulfilled, while for a zigzag nanotube  $n = 0$ . The remaining combinations of indices  $n$  and  $m$  lead to chiral nanotubes exhibiting no specific periodicity along the chiral vector, but instead the arrangement of C atoms shape a spiral around the nanotube axis.

Besides the chiral indices, the tube diameter  $d$  and the chiral angle  $\theta$  are characteristic for a carbon nanotube. The diameter can be calculated from the chiral vector

$$d = \frac{|\vec{C}_h|}{\pi} = \frac{a_0}{\pi} \sqrt{n^2 + nm + m^2}, \quad (2.1)$$

where  $a_0 = \sqrt{3}a_{C-C}$  is the length of the unit vectors. The chiral angle  $\theta$  is defined by the angle between  $\vec{C}_h$  and the zigzag direction and is thus given by

$$\theta = \arccos \left( \frac{n + m/2}{\sqrt{n^2 + nm + m^2}} \right). \quad (2.2)$$

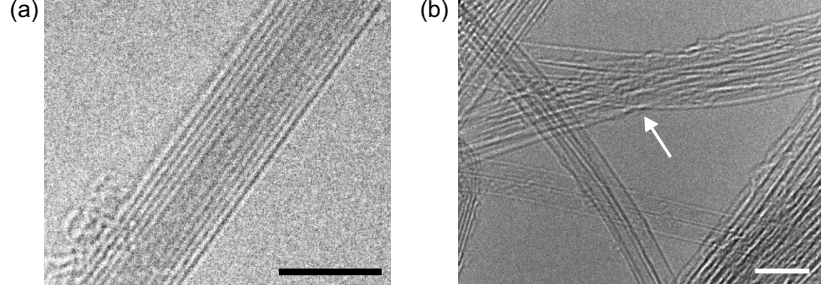


**Figure 2.2:** Transmission electron micrograph of (a) a multiwalled carbon nanotube containing six shells [Spudat10] and (b) many carbon nanotubes bundling together to form ropes, where they are not always perfectly aligned as indicated by the arrow. Scale bars are 5 nm.

Depending on the chiral indices, carbon nanotubes exhibit distinct properties, which will be discussed in the following sections. Many of these properties can be derived from graphene due to the similarities in the atomic structure.

Carbon nanotubes as they are described above are called single-walled carbon nanotubes (SWNTs), because they consist of only one graphitic cylinder. Several coaxially aligned SWNTs enclosing each other form a multiwalled carbon nanotube (see Fig. 2.2a). The individual walls are bound by van der Waals interactions and exhibit an intershell spacing of  $\sim 0.34$  nm [Kiang98] comparable to the interlayer distance of 0.344 nm in graphite. It is possible to synthesize carbon nanotubes with many walls and the chiralities can be combined arbitrarily.

Several carbon nanotubes can also be axially aligned next to each other to form ropes where the nanotubes bundle together due to intertube van der Waals interactions. The amount of nanotubes in one rope can vary from two up to several hundred. Within one rope, the nanotubes can form a hexagonal structure [Thess96]. However, in the view of a possible mechanical application, the van der Waals forces between nanotubes in a rope were found to be weak and the tubes can easily slide past each other [Salvetat99]. Because the ropes are composed of nanotubes of different diameters and chiralities, local distortions of the close-packed arrangement are to be expected. Also, individual carbon nanotubes may be axially bent due to defects in the atomic structure and the intertube forces can be too weak to stabilize a uniform structure. Furthermore, nanotubes can also be missing in a rope, resulting in vacancies in the hexagonal structure [Salvetat99].

With imaging techniques such as atomic force microscopy (AFM) or scanning electron microscopy (SEM), a single-walled nanotube can hardly be distinguished from a thin rope or a multiwalled carbon nanotube. Transmission electron mi-

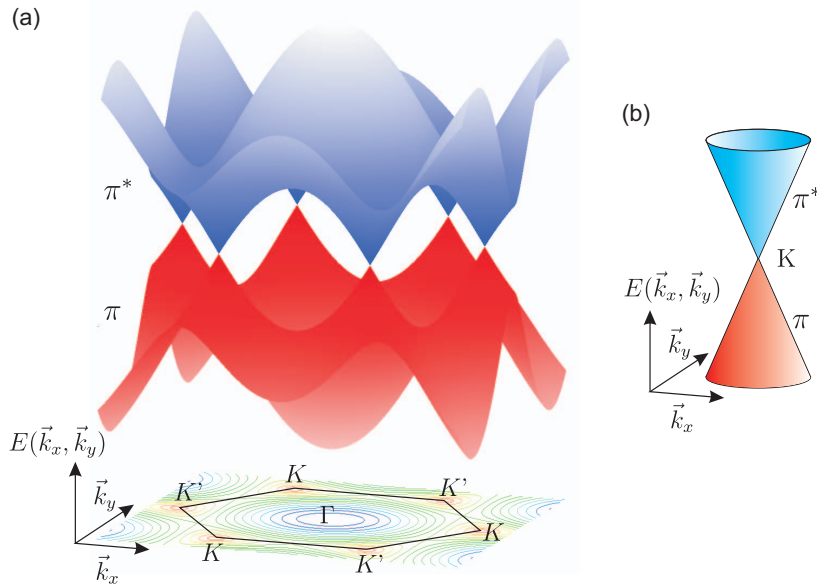


**Figure 2.3:** (a) Electronic band structure  $E(\vec{k}_x, \vec{k}_y)$  of graphene obtained by a tight-binding approximation.  $\pi^*$  is the conduction band and  $\pi$  the valence band. (b) Dirac cone. Linear approximation of the band structure around the  $K$  point.

croscopy (TEM), however, can resolve the individual walls of nanotubes and also distinguish between the nanotubes of a rope as shown in Fig. 2.2.

## 2.2 The electronic band structure

By a zone-folding approximation it is possible to deduce the electronic band structure of carbon nanotubes from the band structure of graphene, which will be discussed first. The graphene band structure shown in Fig. 2.3a is obtained by a tight-binding approximation [Wallace47, Reich02a] taking into account nearest-neighbour interactions, which leads to the dispersion relation for the conduction ( $E_+$ ) and the valence ( $E_-$ ) band

$$E_{\pm}(k_x, k_y) = \pm \gamma_0 \sqrt{1 + 4 \cos \frac{\sqrt{3}k_x a_0}{2} \cos \frac{k_y a_0}{2} + 4 \cos^2 \frac{k_y a_0}{2}}, \quad (2.3)$$

where  $\gamma_0$  is the transfer integral between nearest-neighbour  $\pi$  orbitals with typical values of 2.9–3.1 eV. The valence band  $\pi$  and the conduction band  $\pi^*$  touch each

---

## 2.2. THE ELECTRONIC BAND STRUCTURE

---

other at six points, denoted by  $K$  and  $K'$ , at the corners of the Brillouin zone. Consequently, graphene is a semimetal or zero-bandgap semiconductor with a Fermi surface containing two inequivalent points<sup>1</sup>. Around these high-symmetry points  $K$  and  $K'$  in the Brillouin zone, the dispersion relation is quasilinear for energies close to the Fermi energy ( $< 1$  eV). Expanding Eq. 2.3 around  $K$  or  $K'$  yields the linear dispersion relation of graphene

$$E_{\pm}(\vec{k}) = \pm \hbar v_F \vec{k}, \quad (2.4)$$

where  $\vec{k} = \vec{k} - K$  and  $v_F$  is the Fermi velocity given by

$$v_F = \sqrt{3} \frac{\gamma_0 a_0}{2\hbar}, \quad (2.5)$$

which has the value  $v_F \approx 1 \cdot 10^6$  m/s. The band structure is then reduced to two cones (see Fig. 2.3b), one at the  $K$  and one at the  $K'$  point.

The linear dispersion relation is better described by the Dirac equation rather than the usual Schrödinger equation [Geim07, Geim09]. The nonrelativistic Schrödinger equation

$$\hat{H} = \frac{\hat{p}^2}{2m^*} \quad (2.6)$$

normally describes charge carriers in condensed matter physics with an effective mass  $m^*$  different from the free electron mass and is applicable to semiconductors, which usually exhibit quadratic dispersion relations. In contrast, the Dirac equation describes relativistic particles in the limit of zero rest mass

$$\hat{H} = c \vec{\sigma} \cdot \hat{p}, \quad (2.7)$$

where  $c$  is the speed of light,  $\vec{\sigma}$  is the Pauli matrix and  $\hat{p}$  is the momentum operator. The linear dispersion given by Eq. 2.4 is the solution to the following effective Hamiltonian at the  $K$  or  $K'$  point

$$\hat{H} = \hbar v_F \vec{\sigma} \cdot \hat{k}, \quad (2.8)$$

which resembles the Dirac equation. This means, that the electrons in graphene mimic particles with zero mass and effective "speed of light"  $v_F$ , which is the Fermi velocity of graphene. In analogy to the spin matrices of the Dirac equation,  $\vec{\sigma}$  is called pseudospin matrix. Similar to the real spin that can be up or down, the pseudospin is an index that indicates on which of the two graphene cones a particle is located. Due to the similarities to Dirac fermions in the vicinity of  $K$  and  $K'$ , these points are also called Dirac points, and the conical sections of the energy spectrum are called Dirac cones. The ballistic transport observed in graphene devices can be understood by a suppressed backscattering mechanism due to its characteristic band structure. A similar mechanism is responsible for ballistic transport in carbon nanotubes and will be explained in section 2.2.2.

---

<sup>1</sup>One third of each of the six points contributes to the Fermi surface.



### 2.2.1 The zone-folding approximation

Knowing about the band structure of the two-dimensional graphene, the band structure of carbon nanotubes can be obtained by considering the additional confinement to one dimension. This is called the zone-folding approximation [Reich04]. Along the nanotube axis, the system is considered extended and the wave vectors  $\vec{k}_{\parallel}$  parallel to the tube axis can be assumed to be continuous. Perpendicular to the tube axis, the system is confined and the wave vectors have to fulfill periodic boundary conditions

$$\vec{C}_h \cdot \vec{k}_{\perp} = 2\pi p \quad (p \in \mathbb{N}). \quad (2.9)$$

This means, the  $k$  space is quantized into allowed states along  $\vec{k}_{\perp}$  separated by  $|\Delta\vec{k}_{\perp}|$  depending on  $|\vec{C}_h|$  and therefore depending on the diameter:

$$|\Delta\vec{k}_{\perp}| = 2/d. \quad (2.10)$$

The quantized  $\vec{k}_{\perp}$  are sketched as lines within a contour plot of the graphene band structure in Fig. 2.4a and b. The band structure of a particular nanotube as a function of  $\vec{k}_{\parallel}$  is sliced out of the graphene energy bands along each of these lines and plotted in Fig. 2.4c and d. A nanotube is metallic if the allowed  $\vec{k}_{\perp}$  values include the  $K$  point, and semiconducting if the  $K$  point is excluded. The classification into metallic or semiconducting nanotubes can be done with the family index  $\nu$ . This index is defined by  $\nu = [(n - m) \bmod 3]$  and hence yields three different families of nanotubes

$$\nu = \begin{cases} -1 & \text{semiconducting CNTs type I} \\ 0 & \text{(semi)metallic CNTs} \\ +1 & \text{semiconducting CNTs type II.} \end{cases} \quad (2.11)$$

The  $\nu = 0$  family includes all armchair nanotubes, which are truly metallic. The valence and the conduction band touch each other at the Fermi level at two different  $\vec{k}_{\parallel}$  in an armchair band structure. All other nanotubes in the  $\nu = 0$  family contain only one point where valence and conduction band are touching. Considering the dispersion of a graphene sheet, this would make them metallic. However, curvature effects due to the rolling of the graphene sheet play a crucial role in carbon nanotubes [Reich02b] and in this case, the curvature leads to an opening of a small bandgap on the order of several meV and makes the nanotubes semimetals, i. e. small-bandgap semiconductors. The nanotubes belonging to the  $\nu = \pm 1$  families have a larger bandgap which scales inversely with the tube diameter ( $E_{gap} \propto 1/d$ ) and is on the order of  $\sim 1$  eV [Misewich03].

### 2.2.2 Electronic transport properties

Another characteristic features of the electronic structure of carbon nanotubes caused by their one-dimensionality are van Hove singularities in the density of states as plotted in Fig. 2.5. These fingerprints of one-dimensional systems have been observed

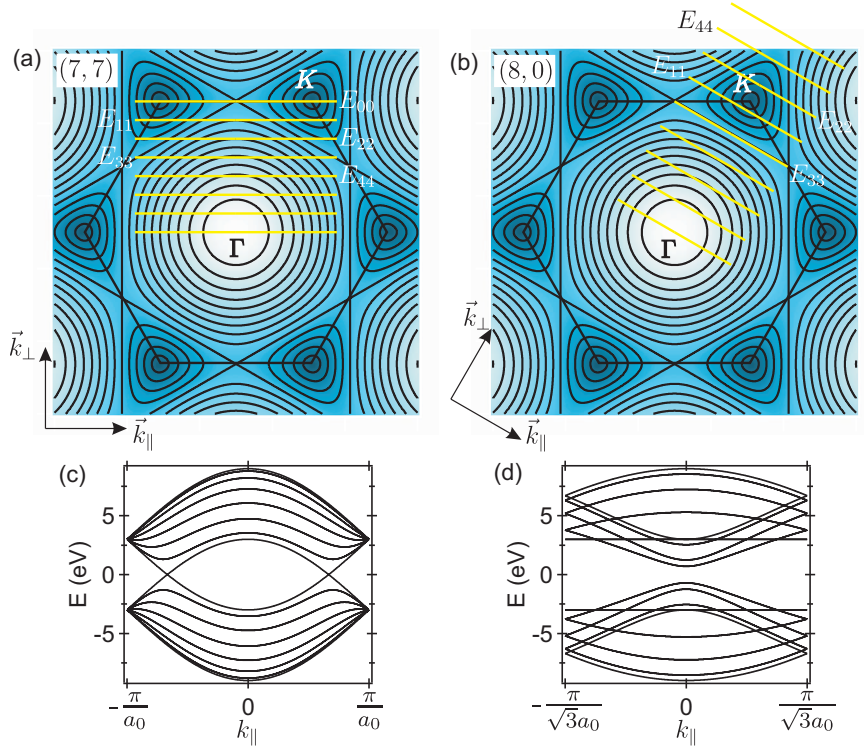
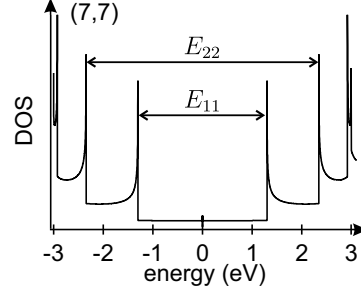


**Figure 2.4:** (a-b) Lines of allowed states perpendicular to the tube axis for a (7,7) armchair and a (8,0) zigzag nanotube plotted on top of a contour plot of the graphene band structure. Dark blue indicates energies close to the Fermi level, white indicates energies far from the Fermi level. (c-d) Resulting nanotube band structure from the zone-folding. The crossing of conduction and valence band for the (7,7) indicates a metallic nanotube. For the (8,0) nanotube a bandgap of 1.4 eV is obtained. [Yang99]

**Figure 2.5:** Density of states as function of energy relative to the Fermi energy of the (7,7) nanotube. The energy between the first and the second van Hove singularities are labelled  $E_{11}$  and  $E_{22}$ , respectively. [Yang99]



by scanning tunneling spectroscopy [Wildöer98] and were also probed by measuring the quantum capacitance of a carbon nanotube to a gate electrode [Ilani06]. Conductance measurements of device geometries similar to the field-effect transistor geometry with two leads and a gate electrode provide a direct means for identifying members of the different families of nanotubes outlined above. The gate voltage dependence of the nanotube conductance can be used to distinguish between metallic and small or large bandgap semiconductors.

Individual semiconducting nanotubes behave as field-effect transistors and have been reported to work with a high performance even at room temperature [Tans98b, Martel98]. In metallic nanotubes, ballistic transport has been detected [Kong01, Liang01], i.e. electrons travelling between two terminals without any scattering event. In this transport regime, the Landauer-Büttiker formula describing the conductance in quasi-one-dimensional systems predicts a conductance of  $G = 2e^2/h$  for one spin degenerate channel [Landauer57, Büttiker86]. In the case of nanotubes, two subbands, i.e. two channels, are available near the Fermi energy and taking spin degeneracy into account, the conductance of a nanotube is predicted to be

$$G = 4 \times \frac{e^2}{h} = \frac{1}{6.5 \text{ k}\Omega}. \quad (2.12)$$

A conductance less than the predicted value can arise from additional resistance due to either the contacts or intrinsic impurities of the nanotubes. Metallic nanotubes were found to approach this quantized conductance value even at room temperature [Kong01, Liang01] and the mean free path for defect scattering in single-walled nanotubes can be up to  $4 \mu\text{m}$  [Mann03]. If the contact resistances are low enough and the transmission approaches unity, the fourfold degenerate bands can also be observed in Fabry-Perot interferences at low temperatures [Kong01, Javey03]. In the case of contacts with a low transmission to the nanotube, Coulomb blockade effects govern the transport behaviour at low temperatures, which will be explained in detail in chapter 4.

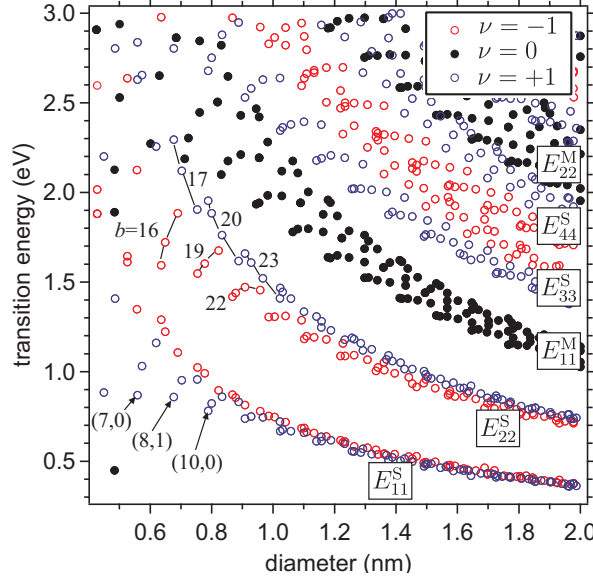


**Figure 2.6:** Optical transition energies as a function of nanotube diameter calculated within a non-orthogonal tight-binding model [Popov04]. Filled circles denote (semi)metallic nanotubes ( $\nu = 0$ ), open circles denote semiconducting nanotubes. The latter divide into two families  $\nu = -1$  and  $\nu = +1$  plotted red and blue, respectively. Several branches are labelled with the branch index  $b$  and some transition energies are labelled with the chiral indices  $(n, m)$ .

### 2.2.3 Optical transition energies

The electronic band structure of a nanotube can have many subbands, however an incident photon can only lead to transitions between particular bands. Only light which is polarized parallel to the tube axis can interact with the one-dimensional nanotube, because of the antenna effect [Ajiki95]. On the other hand, the band index can only be changed by light polarized perpendicular to the tube axis [Ajiki95, Damnjanović99]. Therefore, optical transitions are expected only between subbands with the same band index. The energy of an optical transition is labelled  $E_{ii}$ , where  $i$  is the index of the involved band and counting starts with the band closest to the Fermi level. In the case of negligible exciton binding energies, this corresponds to the energy between two van Hove singularities as plotted in Fig. 2.5.<sup>2</sup>

The transition energies  $E_{ii}$  plotted as a function of the tube diameter form a so-called Kataura plot as shown in Fig. 2.6. Each point in the plot represents the transition energy of a particular nanotube. The data points for a specific band index  $i$  are arranged together exhibiting a  $1/d$  dependence and are separated for metallic ( $E_{ii}^M$ ) and semiconducting ( $E_{ii}^S$ ) nanotubes. The metallic groups are made up from nanotubes of the  $\nu = 0$  family and therefore also include semimetallic nanotubes. Within one of these groups, "V"-shaped branches are formed pointing towards both

<sup>2</sup>In fact, the exciton binding energy in carbon nanotube can be large (0.1 eV to 1 eV [Bachilo02]). However, the principle of the band-to-band transitions as explained here stays valid also when considering excitons [Thomsen07].

sides of the group. For the semiconducting groups, a separation between the families  $\nu = +1$  and  $\nu = -1$  can be seen. The energies of one family always point onto one side of the  $1/d$  dependence. Which one points upwards or downwards alters for subsequent groups.

The nanotubes within one branch have the same branch index

$$b = 2n + m. \quad (2.13)$$

For a given branch, the adjacent transition energies belong to nanotubes, whose chiral indices relate as

$$(n_2, m_2) = (n_1 - 1, m_1 + 2). \quad (2.14)$$

Here, the  $(n_1, m_1)$  are the chiral indices of the nanotube with smaller diameter, i. e. on the left side of the  $(n_2, m_2)$  nanotube in the Kataura plot.

The transition energies plotted in Fig. 2.6 are calculated within a symmetry-adapted non-orthogonal tight-binding model by Popov *et al.* [Popov04]. This model includes curvature induced effects on the electronic band structure in contrast to Kataura plots obtained by the zone-folding approximation of tight-binding models for graphene [Reich02a, Reich04, Thomsen07] and therefore provides a good database of carbon nanotube transition energies. Excitonic effects and electron correlations can be included by rigidly up-shifting the energies by 0.32 eV [Popov04, Maultzsch05], which leads to a good agreement between calculations and experimentally obtained transition energies.

Experimental Kataura plots are obtained by pattern recognition of the optical transitions found by resonant Raman scattering on bulk samples containing many different chiralities [Telg04]. However, the optical transitions are influenced by environmental effects. The intertube van der Waals interactions that promote bundling to carbon nanotube ropes [Girifalco00, Chen03], results in a significant perturbation of the nanotube electronic structure. An additional red-shift of the transition energies for bundled nanotubes has been found [O'Connell04, Débarre08, Michel09, Fouquet09] and attributed to a mutual dielectric screening of the nanotubes within a rope [Wang06]. The magnitude of the shift is under debate and ranges between 50 and 160 meV. A screening by several walls within a multiwalled carbon nanotube is also conceivable [Michel09].

Nevertheless, Kataura plots can be used to identify a particular carbon nanotube with a given diameter, whose transition energy is obtained by resonant Raman scattering or Rayleigh scattering [Fouquet09]. The reliability of this index identification depends strongly on the experimental conditions and on the accuracy of the input values: the tube diameter and the optical transition energy.

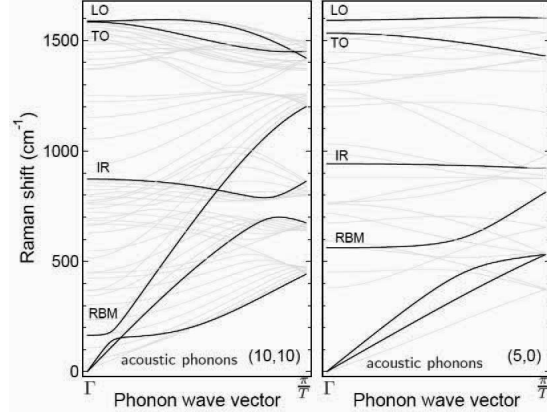


**Figure 2.7:** Phonon band structure of a (10,10) and a (5,0) obtained by valence force field modeling. (Taken from [Telg09])

## 2.3 The phonon band structure – vibrational properties and Raman scattering

The phonon band structure of carbon nanotubes can be obtained from valence force field models [Saito98, Popov00] and yields mainly six phonon bands. Figure 2.7 shows the band structure for two particular nanotubes. In principle, it should be possible to obtain a phonon band structure by the same zone-folding approximation, as used for the electronic band structure (cf. section 2.2.1). However, the curvature for carbon nanotubes is strongly influencing the phonon energies as compared to graphene, so some basic characteristics cannot be explained by a zone-folded band structure [Sauvajol02]. One tool to investigate a phonon spectrum of molecules is Raman spectroscopy, which has been extensively used to characterize carbon nanotube samples [Jorio03a, Dresselhaus05, Thomsen07]. Before we discuss the individual modes of the phonon band structure in Fig. 2.7, we give a brief introduction to Raman spectroscopy.

### 2.3.1 Raman scattering

Light travelling through medium is scattered both elastically and inelastically. An elastic scattering process leaves the energy of the photon unaffected and is called Rayleigh scattering. On the other hand, Raman scattering [Raman28] describes the inelastic scattering processes, where the photon energy  $\hbar\omega_i$  is changed by the energy  $\hbar\omega_{ph}$  of a generated phonon (Stokes process) or an annihilated phonon (anti-Stokes process). Hence, the spectrum of light scattered by a sample contains three components:

- (i) the Rayleigh peak having the same energy as the incident light due to elastically scattered photons:  $\hbar\omega_i$
- (ii) the Stokes spectrum at the low-energy side of the Rayleigh peak due to a generated phonon:  $\hbar(\omega_i - \omega_{ph})$
- (iii) the anti-Stokes spectrum at the high-energy side of the Rayleigh peak due to an annihilated phonon:  $\hbar(\omega_i + \omega_{ph})$

Generally, both the Stokes and the anti-Stokes spectra contain information about the phonon spectrum of the sample, yet, the Stokes spectrum is mostly used due to the higher intensity.<sup>3</sup>

During the Raman scattering process, energy and momentum has to be conserved. The maximum momentum that can be possibly transferred from a photon to a phonon is  $2\vec{k}_i$  in the case of backscattering. Probing with light in the visible range, the resulting phonon momentum  $q$  is about three orders of magnitude smaller than the extent of the Brillouin zone. Therefore, only phonons in the zone-center (at the  $\Gamma$  point in Fig. 2.7) can be observed in Raman experiments.<sup>4</sup>

Having a closer look at the Raman scattering process, electron excitations are involved in an intermediate state. Now three cases of Raman scattering can be distinguished, which are sketched in Fig. 2.8. In the non-resonant case the energy of the incoming photon is far away from an optical transition and the intermediate state involves a "virtual" electronic state. Two resonant cases are possible where the intermediate state involves a real state: either the incoming photon energy ( $\hbar\omega_i$ ) matches an optical transition energy or the outgoing one ( $\hbar\omega_s$ ). The resonant processes result in a higher scattering efficiency and hence in an enhanced Raman signal (by a factor of  $\sim 10^3$  [Dresselhaus05]), so that the non-resonant contributions can be neglected. Matching the resonance condition allows for the observation of an individual nanotube in a Raman setup [Meyer05, Fouquet09].

In resonant Raman spectroscopy of carbon nanotubes, the goal is to find the resonance energy and correlate it with the optical transition energy for a particular  $(n, m)$  nanotube in the Kataura plot. The resonance width depends on the phonon mode involved in the scattering process. For modes with small energy, such as the radial breathing mode, which will be discussed in the following, the resonance width can be as small as 8 meV [Jorio01b], while for the high energy mode the resonance width is in the range of  $\sim 250$  meV [Telg09].

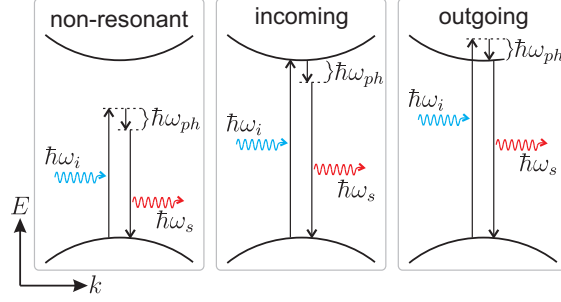


**Figure 2.8:** Sketch of three possible Stokes Raman processes: a non-resonant Raman process, a Raman process with incoming resonance and one with outgoing resonance. A dashed (solid) line indicates a virtual (real) electronic state.  $\hbar\omega_i$  and  $\hbar\omega_s$  denote the energy of the incoming and of the scattered light, respectively.  $\hbar\omega_{ph}$  is the energy of the phonon.

### 2.3.2 A carbon nanotube Raman spectrum

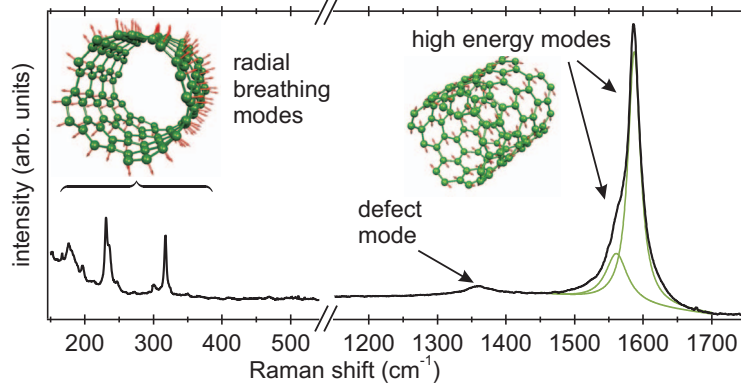
From the six phonon branches in the phonon band structure of a carbon nanotube in Fig. 2.7, the infrared-active phonon (IR) and the acoustic phonons are not expected to be visible in Raman spectroscopy. Limited to first-order Raman processes, the remaining three modes make up a carbon nanotube Raman spectrum. The two phonon branches at high energies correspond to the  $G$  mode in graphite [Tuinstra70]. In the case of the longitudinal optical (LO) phonon, the C atoms vibrate parallel to the tube axis, whereas they vibrate perpendicular to the axis in case of the transverse optical (TO) phonon. Due to their high energy, these modes are called high energy modes (HEMs) or  $G^-$  and  $G^+$  mode according to the  $G$ -mode in graphite. The phonon at low energy corresponds to a coherent radial vibration of the C atoms, as if the tube were breathing, giving rise to the name radial breathing mode (RBM).

Figure 2.9 shows a Raman spectrum of an ensemble of carbon nanotubes grown by chemical vapour deposition (see section 3.2.1), where several RBM peaks and two HEM peaks can be observed. The RBM frequency is strongly diameter dependent, hence we can observe several nanotubes of different diameter within one Raman spectrum, provided that the laser excitation energy fulfills the resonance condition. In addition to the expected phonon frequencies, one mode is observed at  $\sim 1350 \text{ cm}^{-1}$ , which is correlated to a Raman process with two scattering events involving phonons with a wave vector  $q \neq 0$  [Thomsen00]. First-order Raman processes only access phonons in the Brillouin zone center, but by involving two phonons or one phonon together with one elastic scattering event, non-zone-center phonon modes can be accessed. An elastic scattering event involves defects or disorder in the crystal structure, hence the mode is called the defect-induced  $D$ -mode and can

<sup>3</sup>For the observation of an anti-Stokes process, the system has to be initially in an excited state, which is less likely than starting with the system in the ground state, as it is the case for the Stokes process.

<sup>4</sup>This is true, if only one-phonon processes are considered.





**Figure 2.9:** Typical Raman spectrum of an ensemble of carbon nanotubes. Several radial breathing modes are present at low Raman shifts. A defect-induced mode is observed at  $\sim 1350 \text{ cm}^{-1}$  and two high energy modes are found at  $\sim 1600 \text{ cm}^{-1}$ . (Schematics of the RBM and the HEM are adapted from [Telg09])

be used to characterize the quality of nanotubes, which is expressed in the  $D/G$  ratio of the peaks' intensities. Owing to the double resonance process, the  $D$ -mode exhibits a linear upshift of the position with increasing excitation energy [Kürti02]. In the following, the RBM and the HEM will be discussed in more detail, because a carbon nanotube sample can be thoroughly characterized investigating these two modes.

### The radial breathing mode

The radial breathing mode can be modeled by a harmonic oscillation of a cylinder, yielding that the eigenfrequency  $\omega^R \propto 1/r$  is inversely proportional to the radius. In fact, the proportionality constant contains only material constants and is independent of the chirality of the nanotube [Jishi93]. Hence, in the ideal case, the RBM frequency is solely dependent on the diameter. However, environmental effects were found to have strong impact on the phonon energy and an additional additive parameter  $B$  is introduced to describe these effects:

$$\omega^R = \frac{A}{d} + B. \quad (2.15)$$

Depending on the sample conditions, i.e. the growth process (HiPCO, CVD, laser ablation; see section 3.2.1 for nanotube growth) and the environment (free-standing, in solution, on substrate, isolated vs bundled), different values for both parameters are empirically determined. An overview of values found for  $A$  and  $B$  is given

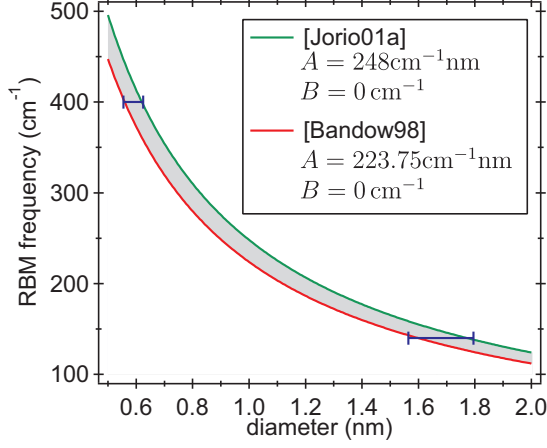


**Figure 2.10:** Radial breathing mode frequency as function of nanotube diameter according to Eq. 2.15. Parameters  $A$  and  $B$  obtained for carbon nanotubes on Si/SiO<sub>2</sub> [Jorio01a] and for carbon nanotube ropes [Bandow98] are used. The error for diameters evaluated from two different RBM frequencies is indicated in blue.

in Tab. A.1 in Appendix A. Generally, these values are obtained by finding the best fit for the RBM frequencies of an ensemble of nanotubes, whose diameters are obtained independently, e.g. by electron diffraction [Meyer05] or using the Kataura plot transition energies obtained by resonant Raman scattering [Araujo08]. Typical values vary between 204 and 248 cm<sup>-1</sup>nm for  $A$  and between 0 and 27 cm<sup>-1</sup> for  $B$ , respectively.

The majority of Raman experiments are performed on ensembles of isolated carbon nanotubes grown by the high-pressure CO method (HiPCO) [Bachilo02, Fantini04, Telg04, Jorio05]. HiPCO nanotubes are believed to be mainly single-walled and grow in thick ropes. For Raman experiments, they are isolated by ultrasonication in aqueous suspension and wrapped with a surfactant to prevent them from rebundling. This heavy treatment may change the nanotubes' phonon energies substantially in comparison to as-grown carbon nanotubes, both on substrate [Jorio01a] and freestanding [Meyer05].

The difference in sample conditions hampers a correlation of Raman spectroscopy and transport experiments. When Raman spectroscopy is used for an additional characterization of transport devices, a careful analysis of the Raman spectra has to consider this aspect. Figure 2.10 plots the RBM frequency as a function of the nanotube diameter taking different values for parameters  $A$  and  $B$ . For details on sample conditions and parameters for various publications that predict frequencies in between the two plotted examples, see Tab. A.1 in Appendix A. Depending on the parameters, a nanotube diameter evaluated solely from an RBM peak can exhibit an error between 0.07 nm and 0.23 nm as indicated in Fig. 2.10. For a carbon nanotube containing more than two walls, we have found strong deviations from the

frequencies of corresponding single-walled nanotubes. These can be ascribed to van der Waals interactions between the shells of the multiwalled nanotube [Spudat10].

Assigning chiral indices to individual carbon nanotubes using the Kataura plot with diameters obtained solely from the RBM frequency, the issues mentioned above have to be considered in order to avoid a wrong assignment. Therefore, the aim should be to gain a picture as complete as possible from the Raman spectrum of a nanotube, e.g. by additionally investigating the HEM, which will be explained in the following.

### The high energy mode

Although the high energy mode in carbon nanotubes is split into two features in contrast to the graphitic  $G$  mode in graphene, the origin is similar. The modes are associated with a vibration of the two different C atoms on the graphene lattice (see Fig. 2.1) against each other. Due to the curvature of carbon nanotubes, the vibration along the tube axis – the longitudinal optical (LO) phonon – has different energy than the one along the circumference – the transverse optical (TO) phonon. In a nanotube Raman spectrum, the lower energy peak around  $1510 - 1570 \text{ cm}^{-1}$  is referred to as the  $G^-$  peak, and the higher energy peak around  $1570 - 1600 \text{ cm}^{-1}$  is labelled  $G^+$ . The assignment of the peaks to LO and TO phonons together with the origin of their distinct peak linewidth has been controversially discussed in literature [Kempa02, Dubay02, Jorio02a, Oron-Carl05, Telg05, Lazzeri06, Piscanec07, Wu07, Fouquet09]. Two typical spectra observed for a metallic and a semiconducting nanotube are shown in Fig. 2.11 [Michel09]. The metallic nanotubes exhibit a noticeably broad lineshape of the  $G^-$  mode.

Phonon-plasmon interactions were proposed as the origin of the broad and asymmetric  $G^-$  lineshape of metallic nanotubes in several reports [Brown01, Kempa02, Bose05] and the peak was attributed to the TO phonon as the phonon band structure suggests. This explanation also involves an increasing linewidth with the thickness of a nanotube bundle [Kempa02]. However, frequencies proposed by the theory do not match experimentally observed  $G^-$  frequencies and moreover, the calculations cannot explain the broadening of the peak observed for isolated, freestanding nanotubes [Michel09]. These latter Raman measurements and a recent combination of Rayleigh scattering with Raman resonance profiles of the RBM and the HEM [Fouquet09] resolve the debate about the downshift and broadening of metallic  $G^-$  peaks by unambiguously attributing it to a strong electron-phonon coupling in accordance with density functional theory (DFT) calculations [Piscanec07, Lazzeri06, Dubay02].

According to the calculations of Piscanec *et al.*, the two HEM peaks are ascribed to the TO or the LO phonon depending on the metallicity of the nanotube [Piscanec07], sketched in Fig. 2.11. In the case of semiconducting nanotubes, the  $G^-$  peak is assigned to the TO phonon and the  $G^+$  peak to the LO phonon, whereas in the case of metallic nanotubes this assignment is opposite: the  $G^-$  peak originates

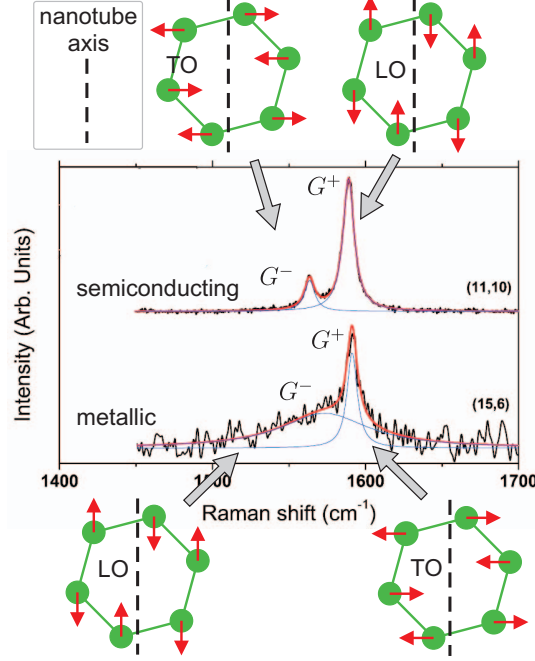


**Figure 2.11:** High energy modes of a semiconducting (11,10) and a metallic (15,6) nanotube with a narrow and a broad  $G^-$  peak, respectively. Spectra are adapted from [Michel09]. The peaks are allocated to TO and LO phonons according to the theory in [Piscanec07]. The sketched vibrations do not consider the particular atomic structure of the nanotubes measured.

from the LO phonon, while the  $G^+$  peak originates from the TO phonon. In both cases, the  $G^-$  peaks exhibit a strong decrease of frequency with decreasing tube diameter, as plotted in Fig. 2.12. Also the  $G^+$  peak is predicted to reasonably depend on the diameter.

The assignment of the peaks can be understood as follows. Theory predicts a strong coupling between the LO phonon and electronic excitations in metallic nanotubes, which leads to a substantial softening of the LO phonon, causing its frequency to drop below the frequency of the TO phonon [Piscanec07, Lazzeri06, Dubay02]. An additional effect is a broadening of the Raman line, which can then be used as a fingerprint to distinguish the Raman signal of metallic nanotubes from semiconducting ones.

Typical linewidths for semiconducting  $G^-$  peaks are  $\sigma \sim 10 \text{ cm}^{-1}$  while for metallic nanotubes the  $G^-$  peak exhibits linewidths of  $\sigma \sim 60 \text{ cm}^{-1}$  [Oron-Carl05]. However, it has been shown that the peak width for metallic nanotubes can vary significantly as a function of the chiral structure due to a variable electron-phonon coupling [Wu07]. According to these results,  $(n,0)$  nanotubes exhibit the broadest  $G^-$ , and the broadening decreases for nanotubes with increasing chiral angle until it is minimal for  $(n,n)$  nanotubes. Therefore, a broadened  $G^-$  peak is a sufficient but not a necessary signature to identify a metallic nanotube.

**Figure 2.12:** Diameter dependence of the  $G^+$  and the  $G^-$  frequency for metallic and semiconducting nanotubes. Shaded areas are a guide to the eye to mark  $G^+$  and  $G^-$ . Calculations for the LO and the TO phonon frequencies are from [Piscanec07] and [Dubay02]. [Jorio03b] is a best fit  $\omega^G \propto 1/d^{1.4}$  for a large set of experimental data points. All other data points are measured frequencies of particular nanotubes.

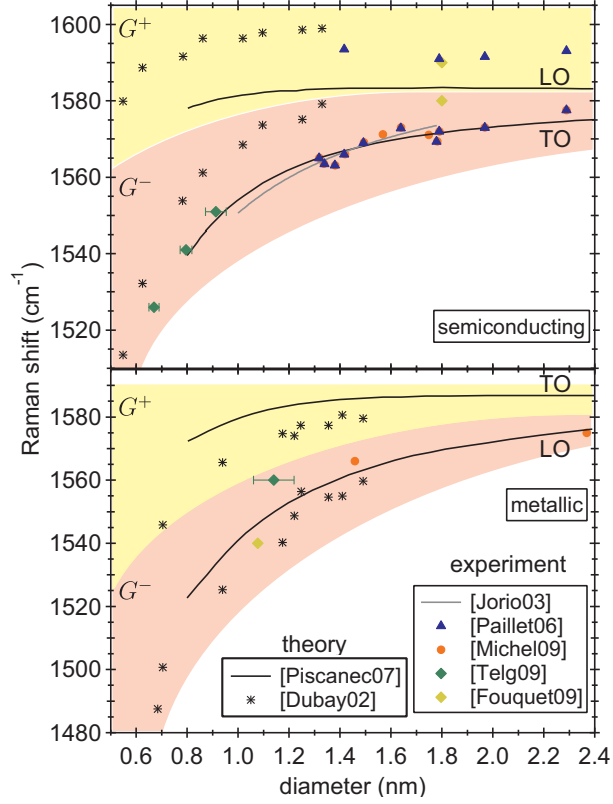


Figure 2.12 gives an overview of experimentally observed HEM frequencies, that were assigned to specific nanotubes and relates these results to calculations by Dubay *et al.* and Piscanec *et al.*, both considering an electron-phonon coupling [Dubay02, Piscanec07]. The experiments compare very different kinds of nanotubes. Jorio *et al.* [Jorio03b] found a best fit for a large data set of  $G^-$  frequencies observed on isolated, semiconducting nanotubes grown by the CVD method on Si/SiO<sub>2</sub> substrate ( $\omega^G = 1592\text{cm}^{-1} - 41.4\text{cm}^{-1}\text{nm}^{1.4}/d_t^{1.4}$ ). Paillet *et al.* and Michel *et al.* performed measurements on spatially isolated, freestanding nanotubes (CVD grown) [Paillet06, Michel09]. Telg *et al.* provides data on individual HiPCO-produced nanotubes wrapped in sodium dodecyl sulfate (SDS) in solution [Telg05, Telg09] and Fouquet *et al.* presented data on a small bundle of suspended CVD carbon nanotubes [Fouquet09]. Especially for the semiconducting nanotubes, the experimental observations for  $G^-$  compare favourably with the predictions by

Piscanec *et al.*<sup>5</sup> From few experiments observing the metallic LO phonon, it seems that data from freestanding nanotubes agrees well with the predictions of the same theory [Michel09, Fouquet09]. The theoretically overestimated phonon softening in the case of Telg *et al.* can be explained by a doping of the nanotube by the surfactant, which weakens the electron-phonon coupling [Telg05, Telg09].

Concluding this brief summary of literature, Piscanec *et al.* provide calculations explaining the HEM frequency for different kinds of nanotubes and therefore also a way to determine the diameter of a nanotube of known metallicity by the frequency of its  $G^-$  peak with a reasonable reliability. The  $G^+$  peak is not suitable for a diameter determination, because experimentally it is found to be essentially diameter independent [Jorio02b, Paillet06], while calculations predict a reasonable dependence. In evaluating the diameter and assigning a chiral index to a nanotube via its Raman spectrum, it is important to interpret the HEM features with the view on a consistent picture of the whole Raman spectrum, i. e. including the RBM frequency and the optical transition energy.

## 2.4 Conclusions

This chapter explained the fundamental characteristics of carbon nanotubes on the basis of the atomic and electronic structure of graphene. The electrical and optical properties, e.g. the metallicity and optical transition energies, can vary strongly depending on the chirality of the nanotubes, providing a variety of macromolecules. Multiwalled nanotubes or a carbon nanotube rope, where different nanotubes may be combined arbitrarily, offer a generic system to probe molecular interactions.

Raman spectroscopy was introduced as a technique capable of identifying phonon modes and the chirality of nanotubes. Furthermore, it was shown to be sensitive to interactions between nanotubes in ropes and multiwalled tubes, as well as to environmental effects such as substrate conditions or doping. Optical transition energies, phonon energies and peak linewidths of the Raman spectra can be used to detect and characterize molecular interactions of nanotubes.

---

<sup>5</sup>[Piscanec07] includes dynamic effects in the DFT calculations, in contrast to [Dubay02].



### 3 Tip-enhanced Raman spectroscopy on a contacted carbon nanotube rope

In molecular electronics, the interpretation of experimental results relies mainly on imaging techniques such as atomic force or scanning electron microscopy (AFM or SEM, respectively) as the only additional characterization. This can easily lead to a misinterpretation, even considering the comparatively rather well-studied carbon nanotubes. The previous chapter explained, how strongly carbon nanotube properties can vary with the chirality, which cannot be detected by means of the mentioned imaging techniques. Also, a small bundle of two or three nanotubes cannot be distinguished from an isolated nanotube on the basis of AFM or SEM imaging only. Furthermore, carbon nanotubes are often assumed to be single-walled relying solely on a statistical characterization of bulk material, whereas the particular nanotube embedded in an electronic device may be of a different kind.

Especially when it comes to functionalized carbon nanotubes, an additional characterization becomes mandatory, because functionalization is usually a statistical process. A functionalization of nanotubes by attaching nanoparticles to the nanotube side walls might still be imaged by AFM scanning [Bogani10]<sup>1</sup>, in contrast to a functionalization by filling the inner hollow of carbon nanotubes as it is done for peapods, which are nanotubes filled with fullerene molecules [Smith98]. For the latter example, quantum transport measurements reported in [Quay07] and [Eliassen10] exhibit features similar to the observations made in this work for a rope. However, the reported samples are claimed to be peapod devices on a statistical basis without any additional characterization of the specific device and thus their interpretation omits the possibility of a carbon nanotube rope as the origin.

Raman spectroscopy probes the vibrational spectrum of a sample and thus reflects its molecular structure. For example, the spectrum of carbon nanotubes allows for determining the diameter, chiral index and electronic structure as discussed in the previous chapter. Their vibrational properties change with functionaliza-

---

<sup>1</sup>However, no information about the chemical bonding can be gained.



tion and also the functionalizing groups may be detected in the Raman spectra [Fantini07, Souza03, Pichler01, Zou07]. These features make Raman spectroscopy suitable as an additional characterization technique of nanoscaled transport devices.

To further enhance the technique sensitivity and to overcome the diffraction limit of light, near-field techniques of optical microscopy can be merged with Raman spectroscopy. One of these techniques, tip-enhanced Raman spectroscopy (TERS), evolved into a powerful experimental tool for probing nanoscaled samples because of a spatial resolution down to 10 nm and an enormous signal enhancement of the order of  $\sim 10^7$  [Hartschuh03, Hartschuh08]. Recently, TERS was reported being able to probe even localized defects in carbon nanotubes [Georgi10]. In contrast to resonant Raman scattering experiments, TERS is, up to now, mostly performed employing only one excitation energy, because a resonance effect is considered to be less pronounced.

This chapter demonstrates the potential of TERS as additional characterization method for molecular electronic devices by presenting results on the TERS characterization of a contacted carbon nanotube rope in a three-terminal setup, which is suitable for quantum transport measurements. More precisely, we use TERS to ensure a correct correlation of Raman and transport data (shown in chapter 6 and chapter 7) by exploiting the local character of this technique. Furthermore, by employing different excitation energies and evaluating the diameter dependent Raman modes, which were introduced in the previous chapter, we can extract not only the diameter and the metallicity of the nanotubes in the rope, but also perform a chiral index assignment with a small group of possible chiralities. The information gained from this characterization method is far beyond what can possibly be achieved by the imaging techniques mentioned above.

The chapter begins with an introduction to the principles of TERS and the setup employed for the measurements. After a section covering the device fabrication, which involves the growth of carbon nanotubes and electron beam lithography for patterning, section 3.3 presents the results of the tip-enhanced Raman experiments.

## 3.1 Tip-enhanced Raman spectroscopy (TERS)

### 3.1.1 The principles of TERS

As discussed in section 2.3, Raman spectroscopy is a powerful tool to characterize nanotubes via their vibrational modes. For nanoscaled devices with individual nanotubes, it is desirable to have a higher spatial resolution than what is offered by the usual confocal Raman setup. In a confocal setup, the incident laser beam is focused onto the sample by an objective lens and only reflected light which is in focus is collected into a spectrometer by blocking out-of-focus light with a pinhole. The resulting probe area of such a setup is  $\sim 1 \mu\text{m}$ .

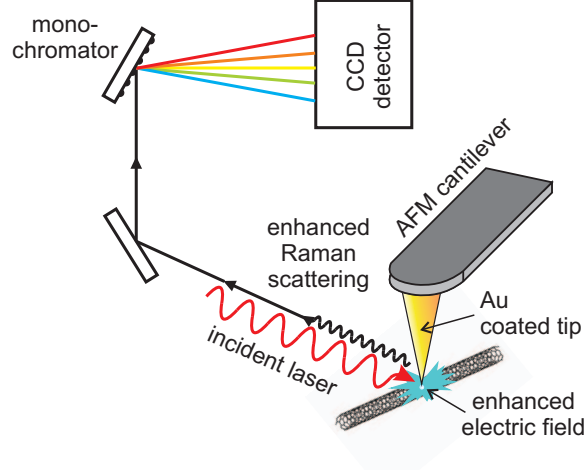


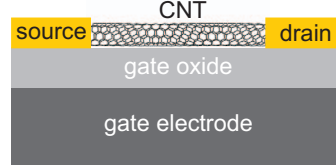
**Figure 3.1:** Schematic of the TERS setup. The Au coated AFM tip is positioned at the region of interest on the sample. The laser illuminates the tip and the sample from the side. The reflected light travels through a monochromator and is detected by a CCD camera.

In contrast, near-field optical microscopy achieves a high spatial resolution by means of interactions between a pointed probe and the electromagnetic near-field of the sample [Hartschuh08]. The enhanced electromagnetic fields are localized at the apex of the pointed probe [Notingher05, Cançado09a]. The enhancement at a metal structure contains three contributions:

- (i) The electrostatic lightning-rod effect caused by geometric singularities leads to localized surface-charge densities enhancing the electromagnetic field in the vicinity of a pointed metal object.
- (ii) Surface plasmon resonances of metal particles enhance the field, depending on the particle shape and dielectric properties.
- (iii) Antenna resonances become relevant when the length of the metal structure matches multiples of half of the wavelength of the laser light.

Basically, there are two ways of enhancing the Raman signal by near-field optics. One technique is called surface-enhanced Raman scattering (SERS) and involves arranging metal particles on the surface in the close vicinity of the area under investigation [Nie97, Kneipp00]. A more flexible technique is tip-enhanced Raman scattering (TERS) [Hartschuh03, Hartschuh08, Cançado09a], where a metal tip can be scanned over the sample surface and brought close to the region of interest. The experimentally determined signal enhancement is based on the Raman scattering signal in the presence and absence of the tip and can reach factors of  $\sim 10^7$  [Roth06]. A spatial resolution of about 10 nm has been reported for TERS [Anderson05].

**Figure 3.2:** Schematic drawing of a carbon nanotube three-terminal device with source and drain contact and a gate electrode.



### 3.1.2 Experimental setup

For the Raman measurements in this work, a tip-enhanced Raman spectroscopy (TERS) setup at the Technische Universität Berlin in the group of J. Maultzsch is used. It is a commercially available combination of an XE-100 (Park Systems) atomic force microscope with a LabRam HR-800 spectrometer (Horiba-Jobin-Yvon). The  $\text{Si}_3\text{N}_4$  AFM tips are purchased from Veeco with a gold coating of 60 nm. For a reduced Au roughness and to avoid the  $\text{Si}_3\text{N}_4$  vibrational signature in the final spectrum, they are additionally coated with 20 nm Au by thermal evaporation in a vacuum chamber [Peica10]. In contact mode, the tip can be positioned on the sample with a lateral resolution of  $\sim 50\text{-}70\text{ nm}$  limited by the tip quality, i.e. its sharpness, and is kept at a distance of  $\sim 1\text{ nm}$  above the surface. The incident laser passes through a microscope objective, which is mounted at  $60^\circ$  to the surface normal, hence illuminating the AFM tip and the sample from the side, as sketched in Fig. 3.1. Spectra are taken in backscattering geometry and recorded with a Peltier-cooled CCD camera. The spectral resolution is  $2\text{ cm}^{-1}$ . Two different laser energies are available for excitation: 2.33 eV from a double-frequency Nd:YAG laser (532.2 nm) and 1.96 eV from a He-Ne laser (632.8 nm). Total near-field enhancement factors of  $10^3 - 10^4$  for Raman spectra of carbon nanotubes have been previously found for this setup [Peica10]. The signal enhancement depends on the shape and the material of the tip and the substrate [Hartschuh08] and provides possibilities for improvements on this new TERS setup.

## 3.2 Device fabrication

Carbon nanotubes can be contacted by metal electrodes to form three-terminal devices in a field-effect transistor geometry. Two metal electrodes – source and drain – are lithographically patterned to contact a nanotube lying on a substrate consisting of an insulating gate oxide on the top and a back gate electrode on the bottom as sketched in Fig. 3.2. In addition to the source and drain contacts, complex gate structures may be patterned. This section describes the fabrication of carbon nanotube devices starting with the nanotube growth. Subsequently, the lithography process is explained, which was established within this work.

### 3.2.1 Carbon nanotube growth

Carbon nanotubes can be synthesized by various methods, with the following three being the most prominent in literature: carbon arc discharge [Ebbesen92, Bethune93], pulsed-laser vaporization (laser ablation) [Thess96] and chemical vapor deposition (CVD). The first two methods involve the evaporation of solid carbon and allow the synthesis of large amounts of nanotubes resulting in powdered samples, where the nanotubes are bundled together. Similar results are obtained by the high-pressure CO (HiPCO) decomposition process, which is a subspecies in the group of CVD methods in which CO gas is used as carbon source instead of graphite [Bronikowski01]. For Raman spectroscopy, mainly bulk carbon nanotube samples produced by the HiPCO method are used. An isolation of individual carbon nanotubes from the ropes can be achieved by ultrasonication in solution, which also shortens the nanotubes drastically. Wrapping the isolated nanotubes subsequently with a surfactant, e.g. sodium dodecyl sulfate (SDS), prevents them from rebundling. Since the phonon modes probed by Raman spectroscopy can be strongly dependent on the environment of the nanotube, this treatment can substantially change the observations in comparison to isolated as-grown nanotubes on substrate or suspended.

For nanoscale transport devices with individual carbon nanotubes, the CVD method is favourable, because it can provide high-quality single-walled nanotubes growing well-separated from spatially defined positions with a length of several tens of micrometers. The various CVD methods differ by the carbon precursor (methane, CO, alcohol) and the catalyst (mainly transition metals: Ni, Fe, Mo, Co) [Moisala03]. In this work, the growth of carbon nanotubes follows a route established by Kong *et al.*, where bimetallic (Fe/Mo) catalytic islands are patterned by means of electron beam lithography on silicon substrates and methane is used as the feed gas during the CVD-growth process [Kong98].

The catalyst solution is produced by suspending  $\text{Fe}(\text{NO}_3)_3$  and  $\text{MoO}_2(\text{C}_5\text{H}_5\text{O}_2)_2$  together with alumina nanoparticles as support material in methanol. Sonication for several hours ensures a good homogeneity of the solution. A silicon substrate is lithographically patterned with holes ( $0.5 \times 0.5 \mu\text{m}^2$ ) in the PMMA, as described in the following section. The catalyst solution is dripped onto the masked substrate and the solvent is evaporated at  $150^\circ\text{C}$ . The subsequent removal of the PMMA mask is performed in heated acetone ( $\sim 50^\circ\text{C}$ ) while sonicating at low power for 30 s and results in catalyst islands at defined positions.

For carbon nanotube growth, the substrate with the patterned catalyst islands is then heated in a tube furnace in an argon flow of 1.52 l/min. When the growth temperature is reached, the argon flow is replaced by methane (0.52 l/min) and hydrogen (0.70 l/min) for 10 min, during which the nanotube growth takes place. The number of walls of the nanotubes was found to depend on the final growth temperature [Spudat09]. For the samples in this work a temperature  $\sim 920^\circ\text{C}$  was chosen, for which the process results mainly in single-walled and few double-walled

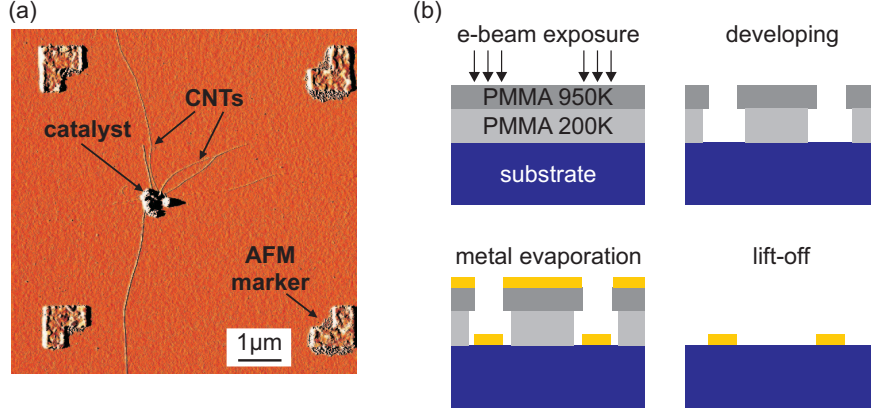


**Figure 3.3:** (a) Atomic force micrograph of several nanotubes grown from one catalyst island on a prepatterned Si substrate. (b) Schematics of the individual steps of electron beam lithography. An undercut is formed after exposing and developing the PMMA bilayer. This avoids a coating of the sidewalls upon metal evaporation.

carbon nanotubes. After growth, the sample is cooled down to room temperature under argon flow. Typically, several nanotubes grow from each catalyst island, as shown in the AFM image in Fig. 3.3a. Diameters of individual nanotubes as determined from height profiles of the AFM images vary roughly between 1 nm and 2 nm.

### 3.2.2 Electron beam lithography

Patterning of microstructures usually involves several lithography processes, i. e. either photolithography or electron beam lithography (EBL). The main advantage of EBL over photolithography is the possibility to write nanometer-sized structures, because it is not limited by the diffraction limit of light. Moreover, it offers the flexibility to write individually designed contact patterns for particular devices, which is crucial, since the carbon nanotubes grow in random directions. For patterning the samples in this work, only EBL was used.

For an EBL process, a beam of electrons is scanned across the sample which is covered with a resist. The result is a pattern with regions of exposed resist which are subsequently removed in a developing process. The remaining resist acts as a mask for the following step, which can be metal evaporation, catalyst deposition or an etching process. At last, a lift-off process in acetone removes the remaining resist together with the spare metal on top of it.

As resist, we use the polymer polymethylmethacrylate (PMMA) diluted in ethyl lactate. PMMA is available with different molecular weights of the polymer and

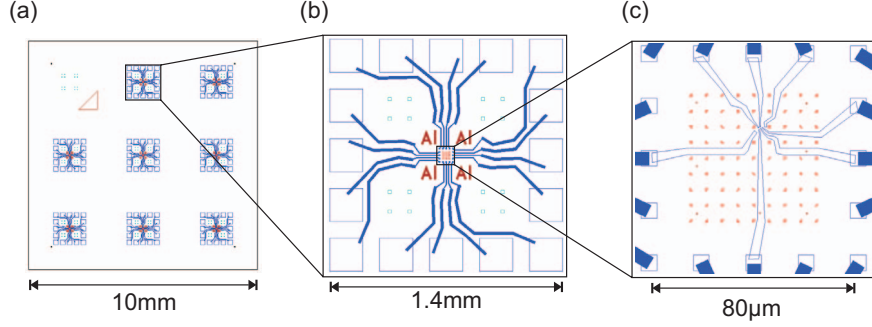


**Figure 3.4:** Sample pattern at the end of the fabrication process. (a) Complete sample with contacts. Eight similar cells are patterned. (b) Zoom into one cell labelled *A1* with bonding pads and coarse contact lines in dark blue. Alignment markers for the electron beam are light blue. Each cell contains several catalyst islands. (c) Region of the fine contacts individually designed for each nanotube. The nanotubes are located by AFM imaging relative to the red AFM markers.

different solids content in the solvent. A lower molecular weight leads to a higher sensitivity to electron exposure, and with an identical incident dose the structures will be broader after developing. By this means, a so-called undercut can be formed, if a bilayer PMMA is used with a bottom layer containing the lower molecular weight polymer. This avoids a coating of the sidewalls during metal evaporation and facilitates the subsequent lift-off process (see Fig. 3.3b).

In our case, the bottom layer consists of PMMA with a molecular weight of 200K (AR-P 649.04 from Allresist GmbH) while the top layer consists of 950K PMMA (AR-P 679.02). Both PMMA layers are spin-coated onto the substrate with 3000 rpm for 60 s and baked for 15 min at 180°C. For the bottom layer with 4% solid content, this leads to a thickness of 180 nm, while the top layer is 100 nm thick (2% solid content). The exposed PMMA is developed for 120 s (AR 600-55 from Allresist GmbH) and the developing process is stopped by isopropanol.

The most important parameters for EBL are the current, which correlates to the beam size, the beam step size, the dose and the acceleration voltage. While the acceleration voltage is kept constant at 50 keV, the other parameters have to be varied according to the structure size and the desired resolution. Dose tests were carried out with metal test structures of different sizes and the resulting ideal parameters are given in Appendix B in Tab. B.2.

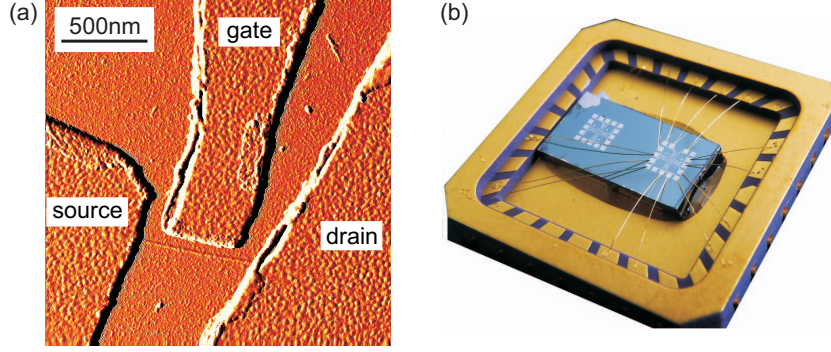


**Figure 3.5:** (a) Atomic force micrograph of a carbon nanotube device with contacts and a side gate (5 nm Ti/60 nm Au). (b) Photograph of a sample containing two cells glued into a chip carrier and wire bonded. (Picture taken by B. Küpper.)

### 3.2.3 Process steps

Starting from a highly doped Si substrate ( $10 \times 10 \text{ mm}^2$ ) with a thermal  $\text{SiO}_2$  layer of 200 nm thickness on both sides, the markers (5 nm Ti/60 nm Pt) are patterned in a first EBL step. As shown in Fig. 3.4, the sample consists of eight cells with alignment markers and markers for AFM imaging. A second EBL step is made for patterning the catalyst islands within the AFM field. After the CVD growth process, the carbon nanotubes are located by AFM. Subsequently, contacts are patterned with a third electron beam step. Bonding pads and coarse contact lines are similar in each cell (see Fig. 3.4b), whereas the fine contacts within an area of  $80 \times 80 \mu\text{m}^2$  are individually designed as in Fig. 3.4c. Typically, contacts consist of a thin adhesion layer of 2-5 nm Ti with the actual contact material on top (60 nm Au), as is the case for the device shown in Fig. 3.5a. The contacted CNT devices are glued into a chip carrier and wire bonded (see Fig. 3.5b). The highly doped Si substrate acts as a back gate and is contacted by scratching through the  $\text{SiO}_2$  layer on top and connecting the doped Si with the bonded inside of the chip carrier by silver epoxy.

## 3.3 TERS on a contacted carbon nanotube rope

The following sections present Raman spectra of a contacted carbon nanotube rope obtained in the TERS setup described in section 3.1. An AFM image in Fig. 3.6a shows the device, where source and drain electrodes (5 nm Ti/60 nm Au) are patterned onto the nanotubes with a separation of 360 nm. The height image in Fig. 3.6b shows a height of  $\sim 7 \text{ nm}$ , suggesting that the device consists of a nanotube rope rather than an individual nanotube. Next to the contacted region, one or more

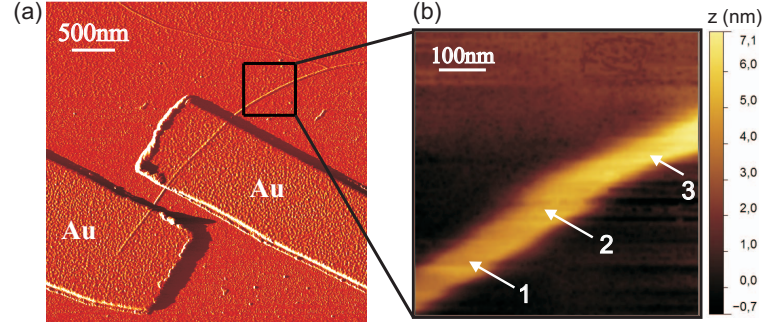


**Figure 3.6:** (a) Atomic force micrograph of the CNT rope with Au contacts taken in tapping mode AFM with a Si tip (amplitude signal). (b) Atomic force micrograph of the CNT rope next to one of the contacts taken in contact mode with a gold-coated  $\text{Si}_3\text{N}_4$  tip (height signal). Raman spectra are taken at the three different positions labelled by arrows.

nanotubes of the rope branch off, further evidencing that we most likely do not deal with a single multiwalled carbon nanotube. The same device is used for low-temperature transport measurements presented in chapter 6 and chapter 7.

### 3.3.1 Signal enhancement due to a metal tip

Before taking a Raman spectrum, first a topographic image is taken by scanning the AFM tip across the surface in contact mode (see Fig. 3.6b). Having the spatial and the height information about the sample, the AFM tip is kept at a distance of  $\sim 1$  nm above the sample surface at the position of interest as indicated in the figure and Raman spectra are obtained. The lateral resolution of  $\sim 50$ – $70$  nm is determined by the tip apex. The diameter of the enhanced light field is similar to the diameter of the tip apex providing the local character of the measurement technique. A theory developed for the near-field Raman enhancement in one-dimensional systems predicts that the signal enhancement caused by the presence of a gold tip is inversely proportional to the 10th power of the tip-sample distance [Cançado09b]. Experimentally, the enhancement decays to zero if the distance of the tip reaches  $\sim 10$ – $15$  nm [Roth06, Cançado09b]. Because it was not possible to obtain a carbon nanotube signal with the tip located in between the two contacts, TERS spectra were taken in the close vicinity of one of them (see Fig. 3.6). Here, the height of the rope is measured to be the same as in between the two contacts ( $\sim 7$  nm), ensuring that the rope does not undergo significant structural changes and that any Raman signal obtained originates from contacted nanotubes. The local character of TERS



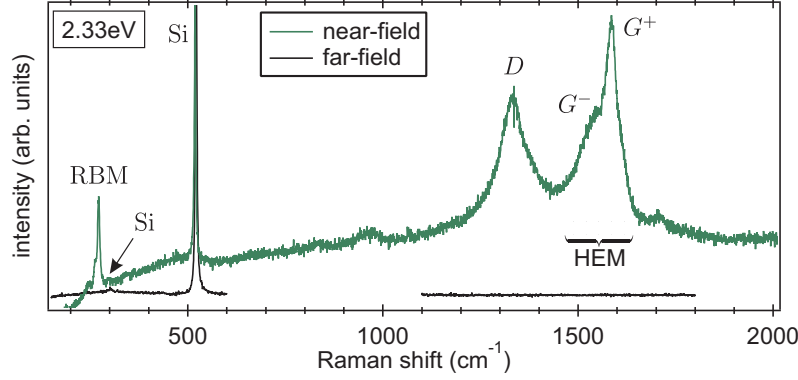


**Figure 3.7:** Near-field and confocal far-field Raman spectra at position 1 as marked in Fig. 3.6b with an excitation energy of 2.33 eV. The substrate peaks (Si) and the CNT-related Raman modes (RBM,  $D$ ,  $G^-$ ,  $G^+$ ,  $D^*$ ) are labelled.

also excludes that one of the nanotubes branching off before the contacted region can possibly interfere with the Raman signal from the rope.

Figure 3.7 shows the confocal far-field and the near-field signal of the contacted rope at position 1, as marked in Fig. 3.6b, for an excitation energy of 2.33 eV. For the confocal far-field spectra, the tip is retracted from the sample. The far-field spectra exclusively show peaks of the Si substrate with no Raman mode characteristic for nanotubes at the given experimental conditions (laser power and integration time). On the other hand, the near-field signal clearly shows CNT-related phonons for two different excitation energies (see Fig. 3.8 and Fig. 3.10 in section 3.3.2). Generally, the signal enhancement is measured as the ratio between enhanced near-field signal and far-field signal. TERS spectra obtained at the same experimental setup on non-contacted carbon nanotube bundles showed CNT Raman modes in far-field and in near-field configuration and total enhancement factors of  $10^3 - 10^4$  were measured [Peica10]. A very weak nanotube signal without tip-enhancement has been reported [Yano06], however a reason for the complete vanishing in our case remains unclear. One possibility is a quenching of the modes due to the contacts on top of the rope and hence a too low intensity of the modes to be observable within the noise. On the other hand, confocal Raman measurements on contacted CNTs are reported [Oron-Carl05, Rintala09, Frielinghaus11]<sup>2</sup>, where a signal of individual nanotubes was obtained without tip enhancement. Most likely, a nanotube signal could be obtained by increasing the integration time or tuning the incident laser energy closer to the resonance energy for a particular nanotube.

<sup>2</sup>Here, [Oron-Carl05] and [Rintala09] present data of carbon nanotubes on substrate, whereas we obtained Raman spectra of contacted, freestanding carbon nanotubes[Frielinghaus11].

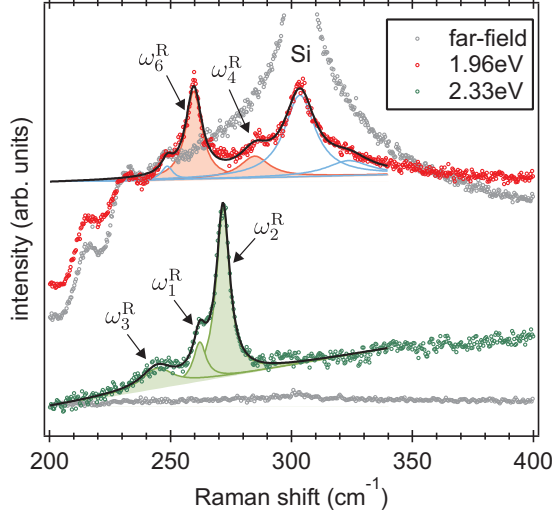


**Figure 3.8:** Confocal far-field and near-field TERS spectra measured at position 1 of the CNT rope for 1.96 eV (red) and 2.33 eV (green) excitation energy. The signal from the Si substrate (at 302 and 325  $\text{cm}^{-1}$ ) and artefacts from the cut-off of the spectrometer (at 248  $\text{cm}^{-1}$ ) in the red spectrum are fitted in blue. RBMs originating from different CNTs are fitted with a Lorentzian lineprofile and labelled  $\omega_i^{\text{R}}$ , where  $i$  is the CNT index.

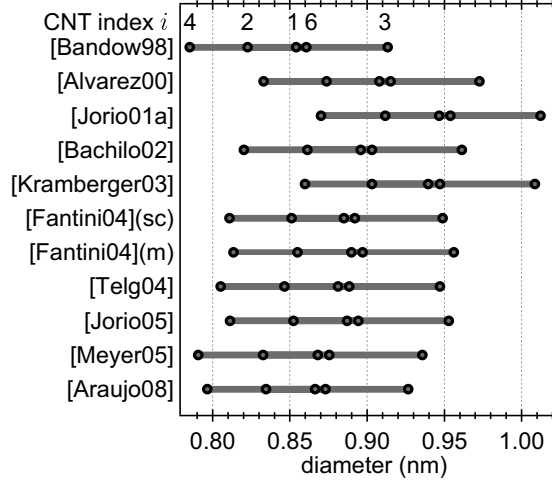
The most prominent mode in Fig. 3.7 is the high energy mode (HEM) between 1500 and 1600  $\text{cm}^{-1}$  consisting of two parts: the  $G^-$  and the  $G^+$  peak at lower and higher Raman shifts, respectively. The defect-induced  $D$  peak at 1333  $\text{cm}^{-1}$  exhibits a rather high intensity, atypical for CVD-grown carbon nanotubes. Usually, a  $D/G$  ratio below 0.1 is observed for our as-grown CVD nanotubes [Spudat08]. This high intensity may be induced by a signal enhancement, which can be selectively higher for individual modes [Peica10]. On the other hand, it hints at an increased defect density, possibly induced by extensive transport measurements and temperature cycles which the sample was subjected to. Radial breathing modes (RBMs) arise next to the Si substrate peaks at frequencies between 200 and 300  $\text{cm}^{-1}$ . For the identification of individual strands within the rope, we focus on the two diameter-dependent modes, i. e. the RBM and the  $G^-$  mode, as discussed in section 2.3.2.

### 3.3.2 Identifying individual strands of the nanotube rope

In Fig. 3.8 two RBMs at frequencies  $\omega_6^{\text{R}} = 260 \text{ cm}^{-1}$  and  $\omega_4^{\text{R}} = 285 \text{ cm}^{-1}$  can be observed using an excitation energy of 1.96 eV. At an excitation energy of 2.33 eV three different RBM frequencies ( $\omega_3^{\text{R}} = 245 \text{ cm}^{-1}$ ,  $\omega_1^{\text{R}} = 262 \text{ cm}^{-1}$  and  $\omega_2^{\text{R}} = 272 \text{ cm}^{-1}$ ) are found. None of the modes is found at both excitation energies, indicating a clear resonance effect present also in tip-enhanced Raman spectroscopy.

As mentioned earlier in section 2.3.2, the diameter dependence of the RBM frequency (see Eq. 2.15) is strongly associated with environmental effects leading to a change in the parameters  $A$  and  $B$ . Figure 3.9 gives an overview of the spread of

**Figure 3.9:** Comparison of CNT diameters evaluated by taking different parameters  $A$  and  $B$  for the diameter dependence of the RBM frequency (see Eq. 2.15). The numbers mark the CNT index  $i$ . The specific parameters for each reference are given in Tab. A.1 in Appendix A.



the diameters obtained for the observed RBM frequencies taking different literature values. The smallest diameters are obtained taking parameters by Bandow *et al.* found for nanotube ropes grown by the laser ablation method [Bandow98]. These values differ by  $\sim 0.09$  nm from the maximal ones evaluated taking parameters by Jorio *et al.* found for individual CNTs on a Si/SiO<sub>2</sub> substrate [Jorio01a]. For the  $(n, m)$  indexing of the nanotubes in the rope later on (see section 3.3.3), diameters in the intermediate range (0.81...0.95 nm) obtained with parameters from [Telg04] are taken. These are given in Tab. 3.1, including a systematic error of  $\pm 0.01$  nm due to the spectrometer resolution of  $\pm 2$  cm<sup>-1</sup>. The used parameters  $A = 215$  cm<sup>-1</sup>nm and  $B = 18$  cm<sup>-1</sup> are obtained from SDS-wrapped nanotubes in solution [Telg04]. Although these sample conditions are in contrast to the situation of unwrapped nanotubes on a substrate here, a comprehensive study of the Raman spectra including a chiral-index assignment of more than 50 chiral indices [Telg04, Maultzsch05] provides a reliable basis for the evaluation of the Raman data here.

Figure 3.10 shows the Raman spectra of the nanotube rope device in the HEM region. At both excitation energies, a splitting into a  $G^+$  part and a  $G^-$  part is observable, where the red spectrum shows an additional splitting into several  $G^-$  peaks at different frequencies. Additionally, both spectra exhibit a peak at 1610 cm<sup>-1</sup>, which involves two scattering events and is defect-induced similar to the  $D$  peak. In contrast to the  $D$  peak, the  $D'$  peak at the observed energy involves intravalley scattering with small phonon wavevectors [Pimenta07].

According to the calculations of Piscanec *et al.* [Piscanec07] the two HEM peaks are ascribed to the transverse optical (TO) or the longitudinal optical (LO) phonon depending on the metallicity of the nanotube (see the discussion in section 2.3.2). In

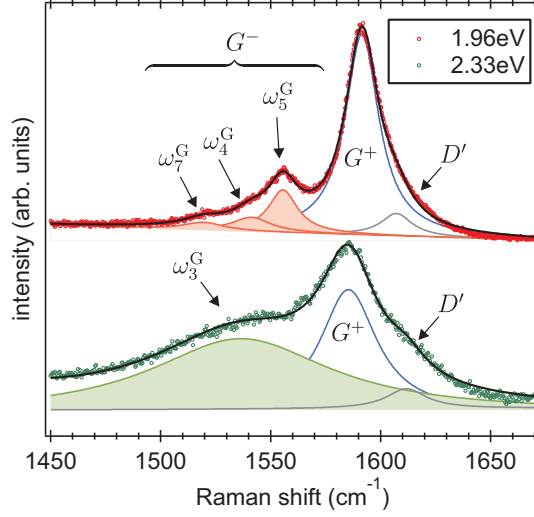
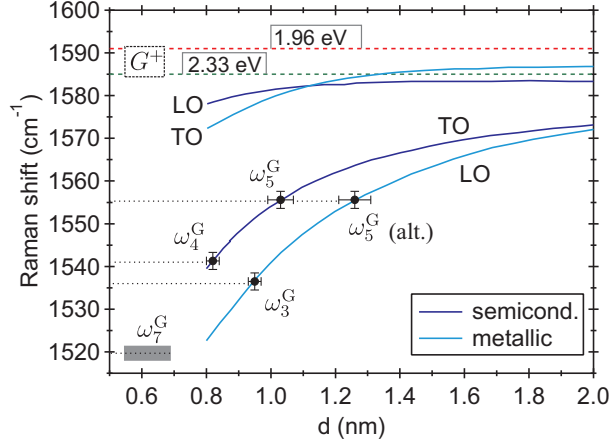


**Figure 3.10:** Near-field TERS spectra measured at position 1 of the CNT rope for two excitation energies. A splitting of the HEM in a  $G^+$  (blue) and a  $G^-$  part is observed.  $G^-$  peaks originating from different CNTs are fitted with a Lorentzian lineprofile and labelled  $\omega_i^G$ , where  $i$  is the CNT index. The defect-induced  $D'$  peak at  $\sim 1610 \text{ cm}^{-1}$  (grey) is labelled.

the case of semiconducting nanotubes, the  $G^-$  peak is assigned to the TO phonon and the  $G^+$  peak to the LO phonon, whereas in the case of metallic nanotubes this assignment is opposite: the  $G^-$  peak originates from the LO phonon, while the  $G^+$  peak originates from the TO phonon. In both cases the  $G^-$  peaks exhibit a reasonable decrease of frequency with decreasing CNT diameter, whereas the  $G^+$  peak is substantially diameter independent [Piscanec07, Jorio02b, Paillet06]. Due to a strong coupling between the LO phonon and electronic excitations in metallic nanotubes, the Raman line of the LO phonon is downshifted and broadened. Here, we will use this broad linewidth as a fingerprint to distinguish the Raman signal of metallic and semiconducting nanotubes. However, it has been shown, that the peak width for metallic CNTs can vary significantly as a function of the chiral structure due to a variable electron-phonon coupling [Wu07] (see the discussion in section 2.3.2). Thus, a narrow  $G^-$  peak alone does not necessarily indicate a semiconducting CNT.

In order to deduce nanotube diameters from the frequencies of the observed  $G^-$  peaks, the metallicity of the particular nanotube has to be extracted. Considering the linewidth of the  $G^-$  peaks, we ascribe  $\omega_3^G$  in the spectrum at 2.33 eV to a metallic nanotube ( $\sigma = 102 \text{ cm}^{-1}$ ), and the three modes of the red spectrum ( $\omega_7^G$ ,  $\omega_4^G$  and  $\omega_5^G$ ) tentatively to semiconducting nanotubes ( $\sigma = 16 \dots 30 \text{ cm}^{-1}$ ). The corresponding diameters of the CNTs are then extracted from the diameter dependence of the  $G^-$  frequency according to Piscanec *et al.* in Fig. 3.11 ( $d_3 = 0.95 \text{ nm}$ ,  $d_4 = 0.82 \text{ nm}$ ,  $d_5^{\text{sc}} = 1.03 \text{ nm}$ ,  $d_7 = 0.62 \text{ nm}$ ; see also Tab. 3.1). For CNT 5, a diameter of 1.03 nm

**Figure 3.11:** Diameter dependence of the HEM for metallic and semiconducting CNTs [Piscanec07]. Observed HEM frequencies are plotted and the diameter corresponding to the  $G^-$  peaks is extracted with a systematic error from the spectral resolution. For  $\omega_5^G$  an alternative diameter evaluation is drawn (see section 3.3.3 for details). The diameter estimation for  $\omega_7^G$  is indicated in grey.



is found assuming the nanotube to be semiconducting. However, in section 3.3.3 it will be shown that this diameter of a semiconducting CNT is not compatible with a chiral index assignment. Thus, an alternative diameter  $d_5^m = 1.26$  nm is evaluated considering the nanotube to be metallic. The lowest  $G^-$  peak  $\omega_7^G$  happens to be beyond the calculated range. An estimate of the respective CNT diameter ( $\approx 0.62$  nm  $\pm$  0.07 nm) can be made, taking into account the experimental extension of the plot [Telg09] (see Fig. 2.12 in section 2.3.2).

For completion, the locations of the  $G^+$  peaks are plotted in Fig. 3.11. Due to the very weak diameter dependence of this mode, the observed peaks are likely to be a superposition of several different CNTs within the rope. Hence, no information about the diameters of the CNTs can be gained from this mode.

Comparing the diameters evaluated from both diameter dependent Raman modes in Tab. 3.1, only for CNT 3 and CNT 4 both modes can be observed. The RBM corresponding to  $\omega_5^G$  in the red spectrum is predicted at frequencies below the cut-off frequency of the spectrometer in the setup for both diameter assignments and thus not observable ( $227$  cm $^{-1}$  for  $d_5 = 1.03$  nm;  $189$  cm $^{-1}$  for  $d_5 = 1.26$  nm). The RBM of CNT 7 ( $\sim 376$  cm $^{-1}$ ) is expected in the region of the broad Si peak and therefore is most likely hidden. Additionally, a low intensity compared to the Si signal is expected for this RBM with regard to the intensity of the respective  $G^-$  mode  $\omega_7^G$ .

The two missing  $G^-$  peaks of CNT 1 and CNT 2 in the green spectrum are expected at similar Raman shifts ( $\sim 1530$  cm $^{-1}$  and  $\sim 1527$  cm $^{-1}$ , respectively) close to  $\omega_3^G$  and with a broad linewidth due to the metallic character of these CNTs (evaluated in section 3.3.3). Considering these linewidths, the Lorentzian fits are not able to resolve the individual  $G^-$  modes of the different diameters. Accordingly, the  $G^-$  mode of CNT 6 (expected at  $\sim 1548$  cm $^{-1}$ ) could easily be hidden by the several  $G^-$  modes observed in the red spectrum.

### 3.3. TERS ON A CONTACTED CARBON NANOTUBE ROPE

$i$	$\omega_i^{\text{R}} (\text{cm}^{-1})$	$\omega_i^{\text{G}} (\text{cm}^{-1})$	$d_i (\text{nm})$	$(2n + m)$	$(n, m)$
1	262	–	0.88	21	(8, 5) (9, 3)
2	272	–	0.85	21	(9, 3) (10, 1)
3	245	1537	0.95	24	(12, 0) (11, 2) (10, 4)
4	285	1541	0.81/0.82	19, 20	(8, 4) (9, 2) (7, 5)
5	–	1556	1.26	30	(13, 4) (12, 6) (11, 8)
6	260	–	0.89	20, 23	(7, 6) (11, 1)
7	–	1520	$0.62 \pm 0.07$	16	(7, 2) (6, 4)

**Table 3.1:** All nanotubes (index  $i$ ) with the observed frequencies for the RBM ( $\omega_i^{\text{R}}$ ) and the  $G^-$  mode ( $\omega_i^{\text{G}}$ ). Evaluated diameters  $d_i$  are given. Nanotube branches are assigned and possible chiral indices  $(n, m)$  are given.

In summary, we find Raman modes corresponding to seven nanotubes with different diameters that exclude the possibility of one thick multiwalled nanotube, considering a diameter difference of 0.68 nm for nanotubes enclosing each other [Kiang98]. Solely from the AFM image, which is in many cases the only characterization of a transport device, the device could misleadingly be assumed to consist of a single multiwalled nanotube. The possibility of double-walled carbon nanotubes being present within the rope has to be considered, especially with the assumption that  $\omega_5^{\text{G}}$  originates from a metallic nanotube, which then could be the outer shell of a double-walled nanotube enclosing CNT 7.

#### 3.3.3 Chiral index assignment

The Raman spectra in Fig. 3.8 and Fig. 3.10 obviously reveal modes of different carbon nanotubes depending on the excitation energy. For varying positions on the rope, the Raman shifts of the modes are reproducible (see section 3.3.4), which excludes a drift of the tip as reason for the distinct spectra. Instead, this indicates that a resonance effect is involved also for tip-enhanced Raman spectroscopy, which has not been considered to play a crucial role so far. In the following, we will ascribe the nanotubes that we identified by our analysis of the diameter dependent Raman modes to branches in the Kataura plot and make a tentative chiral index  $(n, m)$  assignment considering a resonance effect. An overview of the assignments is given in Tab. 3.1.

The Kataura plot in Fig. 3.12 shows optical transition energies  $E_{ii}^{M/S}$  (open and solid circles) for  $(n, m)$  nanotubes as function of their diameter, calculated in the framework of a non-orthogonal tight-binding model [Popov04]. Excitonic effects and

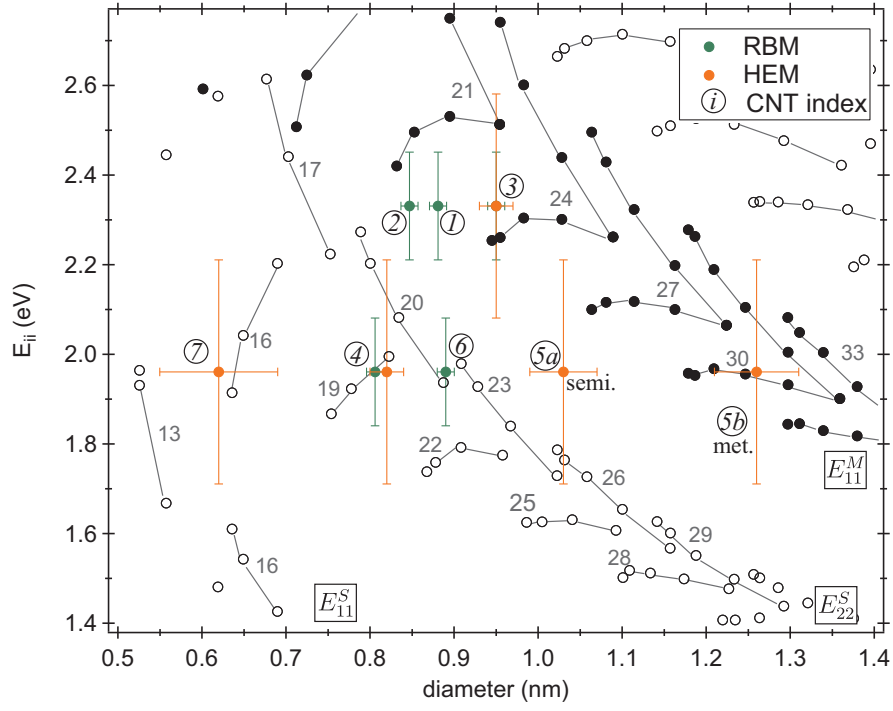


**Figure 3.12:** Kataura plot. Optical transition energies  $E_{ii}^{M/S}$  as function of the diameter of  $(n, m)$  nanotubes [Popov04]. Solid circles denote metallic nanotubes, open circles denote semiconducting ones. Solid lines connect nanotubes belonging to one branch index  $b = (2n + m) = \text{const}$  given by the numbers. Experimental data points are indicated by the CNT index  $i$ . For specific  $(n, m)$  values see Fig. A.1 in Appendix A.

electron correlations are taken into account by rigidly shifting the calculated values by 0.32 eV [Popov04, Maultzsch05]. The evaluated nanotube diameters are drawn at the respective excitation energies. The typical width of the resonance window for RBMs in nanotube ropes is  $\approx 120$  meV [Fantini04], while it is  $\approx 250$  meV for the HEM [Telg09], as known from resonant Raman scattering. Up to now, the influence of the tip enhancement on the resonance window is unknown. Yano *et al.* reported on the possibility to detect nonresonant CNTs without tuning the excitation wavelength to the resonant condition [Yano06]. The resonance window could be strongly affected by the near-field effect. Additionally, a mode can be enhanced by several orders of magnitude in TERS, albeit being excited at the very edge of the resonance window. Hence, we assume large errors for our data points on the  $y$ -axis for  $E_{ii}$  ( $\pm$  the according resonance width). The errors for the nanotube diameters are extracted considering the spectrometer resolution. An estimate of the error in the diameters due to the chosen parameters of the RBM formula in Appendix A reveals that this does not substantially change the following family assignment.

Indexing the observed nanotube modes, an additional redshift of the optical transition energies for nanotube ropes has to be considered. Raman experiments [O’Connell04, Débarre08, Michel09, Fouquet09] and Rayleigh experiments [Wang06] carried out on individual and bundled nanotubes showed that the interaction between the nanotubes bundled in ropes redshifts the transition energies between 50 meV and 160 meV. A redshift of transition energies has been predicted by *ab initio* calculations [Reich02b] and can be attributed to a mutual dielectric screening of the nanotubes in a rope [Wang06]. How this screening would affect the transition energies of nanotubes enclosing each other, e.g. in a DWNT, is not known, but expected to lead to a further redshift [Michel09].

The modes observed for 2.33 eV excitation energy can be clearly assigned to a specific branch. Considering a redshift of the transition energies, CNT 1 and CNT 2 can unambiguously be assigned to the "21"-branch ( $(2n + m) = 21$ ). Possible chiral indices for CNT 1 are (8, 5) and (9, 3) and for CNT 2 the chiral indices (9, 3) and (10, 1) are likely. Note that (9, 3) can not be simultaneously assigned to both nanotubes due to their different Raman shifts of the RBM. For a better clarity of the plot, the specific chiral indices are not marked here. These can be found in Fig. A.1 in Appendix A. In the case of the metallic CNT 3, the "21"-branch can be excluded, because for the only candidate, the (7, 7) armchair nanotube, the LO phonon is forbidden by symmetry [Damjanović99, Reich04]. Thus a  $G^-$  mode would not be observable. Instead, we assign CNT 3 to the adjacent "24"-branch, where three chiral indices are possible considering the mentioned redshift.

The assignment of CNT 4 to one specific branch is not possible, although both of its modes are observed at 1.96 eV excitation energy. However, considering the redshifted transition energies, we tentatively assign the nanotube to the "20"-branch,



rather than to the "19"-branch. Out of the "20"-branch (9, 2) or (8, 4) are candidates for CNT 4, while (7, 5) out of the "19"-branch cannot be excluded.

The assignment for CNT 5 is more difficult. A diameter of 1.03 nm is found assuming  $\omega_5^G$  to be the TO phonon of a semiconducting nanotube. In that case, the nanotube has to be out of the lower  $E_{22}^S$ -branch of semiconducting tubes, i. e. from the "23"- or the "26"-branch. However, considering the additional redshift of energies, the intensity of the mode is higher than expected for a nanotube excited at the edge of resonance. In principle, this could be caused by the high field enhancement at the AFM tip. An alternative route for assigning this mode is to assume it to be the LO phonon of a metallic nanotube despite the small linewidth of  $18 \text{ cm}^{-1}$  as discussed in section 3.3.2. Assuming a metallic CNT 5, its diameter is extracted to be 1.26 nm from Fig. 3.11. This alternative diameter (labelled  $5b$  in Fig. 3.12) hits directly the  $E_{11}^M$ -group of metallic tubes at the "30"-branch. Within this branch, the nanotubes with a large chiral angle are favourably assigned to the mode due to their smaller electron-phonon coupling [Wu07]. This latter assignment for CNT 5 is favourable due to its clear consistency.

$\omega_6^R$  originates either from a nanotube within the "20"-branch or from one within the neighbouring "23"-branch ((7, 6) or (11, 1)). Only the  $G^-$  mode is observed for CNT 7 and the fact that the calculations in Fig. 3.11 do not include such low frequencies, leads to a large error for the diameter of this nanotube. Therefore, despite the fact that the Kataura plot does not give many possibilities at such small diameters, the assignment is difficult. Considering once more the redshift of transition energies due to bundling, an assignment to the "16"-branch is reasonable. Within this branch we can again exclude the (8, 0) nanotube for symmetry reasons<sup>3</sup> [Damjanović99, Reich04]. The (7, 2) and the (6, 4) nanotube remain as possible assignments. However, a previously observed TO phonon frequency at a Raman shift  $6 \text{ cm}^{-1}$  higher than the one here has been assigned to the same nanotubes (see Fig. 2.12 in section 2.3.2) [Telg05]. This discrepancy in the  $G^-$  frequency may be due to different environments (SDS-wrapped HiPCO nanotubes in solution [Telg05] in contrast to CVD-grown nanotubes on Si/SiO<sub>2</sub> substrate here). This interpretation is consistent with the weakened electron-phonon coupling for nanotubes enclosed by a surfactant [Telg05, Telg09] mentioned in section 2.3.2.

In summary, we assigned each of the carbon nanotube strands a nanotube branch index and chiral indices within the Kataura plot, assuming a broad resonance effect for the near-field spectra. We found four metallic and three semiconducting nanotubes. For all carbon nanotubes, the optical transition energies are consistently found to be redshifted due to interactions of the strands in the rope. Additionally, the diameters suggest that the largest metallic nanotube could incorporate one of the semiconducting nanotubes and form a double-walled carbon nanotube. The

---

<sup>3</sup>The TO phonon for zigzag nanotubes ( $n, 0$ ) is forbidden by symmetry.

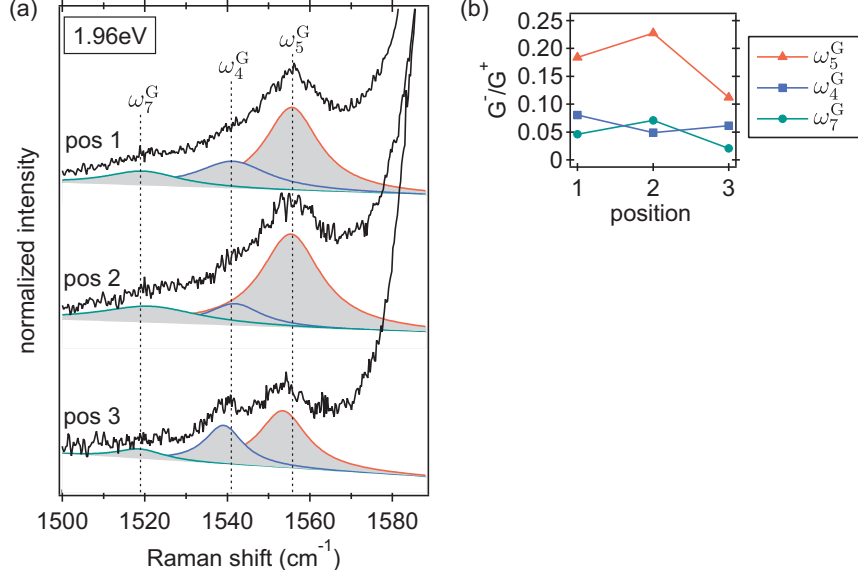


**Figure 3.13:** (a)  $G^-$  modes excited at 1.96 eV for three different tip positions marked in Fig. 3.6. The spectra are normalized to the  $G^+$  mode and offset for clarity. Lorentzian fits for the different modes are plotted shaded. The HEM spectrum at position 3 appears left-shifted by  $\sim 2 \text{ cm}^{-1}$  due to the instrumental resolution. (b)  $G^-/G^+$  intensity ratios (integrated areas) for the respective Raman modes at different tip positions.

classification of the nanotubes into families and branches is a prerequisite to initiate theoretical transport modeling coming from the atomistic side.

### 3.3.4 Monitoring structural changes of the rope

Exploiting the local character of TERS, it is possible to gain spatial information about the rope. Within an AFM window of  $600 \times 600 \text{ nm}^2$ , Raman spectra are taken at three different tip positions marked in Fig. 3.6, with a constant tip height of  $\sim 1 \text{ nm}$  above the rope surface. Figure 3.13 plots the  $G^-$  modes at 1.96 eV excitation energy at these tip positions normalized to the  $G^+$  mode.

The effect of a change in the signal enhancement is most clearly visible for the  $G^-$  modes of CNT 4 and CNT 5.  $\omega_5^G$  clearly decreases in comparison to  $\omega_4^G$  as the tip is moved from position 1 to position 3. The plot of the intensities  $G^-/G^+$  in Fig. 3.13b shows that, while  $\omega_5^G$  is twice as intense as  $\omega_4^G$  at position 1, it is only slightly larger at position 3. This observation suggests that CNT 5 is vertically winding away from the tip, while CNT 4 stays at a similar distance to the tip and

thus maintains a similar vertical position within the rope. It is difficult to interpret the change of the signal enhancement of  $\omega_7^G$  in the same plot due to its low intensity. However, the mode is clearly observable at positions 1 and 2, whereas it is almost vanished at position 3. The plot of  $G^-/G^+$  resembles a similar evolution of CNT 7 compared to CNT 5, which is consistent with the previous interpretation of these two nanotubes forming a DWNT.  $\omega_4^R$  is expected to evolve qualitatively similar to  $\omega_4^G$  since both modes originate from the same CNT. However, the increase of this RBM is overestimated due to an increasing Si peak for different tip positions at whose shoulder the RBM is located (spectra not shown).

For an excitation energy of 2.33 eV, only one  $G^-$  mode is observed, which is thus difficult to evaluate in terms of a spatial intensity change. Furthermore, a comparison of relative intensities for the RBMs at this wavelength is again hampered by the superimposed Si peak.

The signal enhancement is inversely proportional to the 10th power of the tip-sample distance [Cançado09b]. This holds selectively for each strand within the nanotube rope. If an individual nanotube strand changes its vertical position within the rope, this will be visible as a change in the enhancement, i.e. the intensity measured as the integrated area of the Raman signal, specific to this one nanotube, assuming a constant distance of the tip to the rope surface. The selective enhancement can be used for near-field Raman imaging [Hartschuh03, Anderson07] and was shown to reveal the spatial diameter distribution of nanotubes within a rope [Yano06].

Observing a clear change of signal enhancement for the modes of the individual nanotube strands relative to each other at different tip positions, we conclude a non-uniformity of the rope along its axis. Such a structural change of nanotube ropes is observed by transmission electron microscopy (see section 2.1). Although this evaluation is not performed in the region between the two contacts, it is reasonable to assume that the rope behaves similarly there. This may lead to changing interface properties at the two contacts for individual strands.

### 3.4 Conclusions

We found that the tip-enhancement and local character of TERS is crucial to obtain Raman spectra of a contacted carbon nanotube rope. Seven individual nanotubes are identified by their diameter-dependent phonons, the radial breathing mode and the high energy mode, excluding the possibility of a single multiwalled nanotube.

We observe a clear resonance effect for the Raman scattering process, which is up to now not considered in the literature on tip-enhanced carbon nanotube Raman spectroscopy. Considering this resonance effect, we assign each of the observed nanotubes a nanotube branch within the Kataura plot and can narrow the possible chiral indices therein. For all carbon nanotubes, the optical transition energies are consis-

tently found to be redshifted due to interactions between the strands in the rope. In order to extract the magnitude of this energy shift precisely, more information on the resonance width for the investigated Raman modes is required. Employing two different excitation energies, we unambiguously evidenced the important role of the resonance effect in TERS, hence triggering the demand for TERS experiments including tunable excitation energies in order to investigate this effect in detail.

Characterizing the individual strands of the nanotube rope, we find four metallic and three semiconducting nanotubes and can consistently interpret two of the identified nanotubes as forming a double-walled carbon nanotube. The information on the metallicity and chirality of the involved nanotubes gained by Raman spectroscopy can substantially support the interpretation of the electronic transport through the reported device.

In addition, we found that individual strands may change their vertical positions within the rope. The local character of the employed spectroscopic method is a necessary feature to ensure a correct correlation of the Raman and the transport data. Ultimately, our results reveal TERS as being capable to detect single functionalizing molecules connected to a carbon nanotube within a transport device, where standard confocal Raman spectroscopy lacks the crucial local character.



## 4 Single electron transport in carbon nanotube quantum dots

Following elementary quantum mechanics, when electrons in quantum dots are spatially confined to a small region, both charge and orbital degrees of freedom become quantized. In semiconductor quantum dots it is possible to trap individual electrons and investigate their quantum-mechanical properties by electrical transport measurements [Kouwenhoven01, Hanson07]. These devices can hold a fixed but tunable number of electrons and hence provide a control over individual electrons.

Carbon nanotube quantum dots fall in the class of molecular quantum dots [Dekker99, Park02, Nitzan03], which offer a variety and tunability of electrical and magnetic properties in a bottom-up approach by chemical processing. Strong interactions with the environment are peculiar to molecular quantum dots, in contrast to semiconductor quantum dots. Nevertheless, the physical picture explaining the basic features in quantum transport can be adopted from semiconducting dots. Therefore, the concepts of quantum dots and quantum transport are in the beginning introduced in general using the constant interaction model. Subsequently, the characteristics of carbon nanotube quantum dots are addressed.

In the last section of this chapter, a generic model of two parallel quantum dots interacting with each other is introduced and studied within the framework of master equations adapted to carbon nanotube quantum dots. This theoretical model was developed in collaboration with M. R. Wegewijs, S. Smerat and M. Leijnse. Transport calculations employing it reveal the manifestations of molecular interactions in the stability diagram of a coupled dot system. The parallel quantum dot model developed here forms the basis for the interpretation and evaluation of quantum transport measurements on a carbon nanotube rope in this work.

### 4.1 Introduction to quantum dots

A quantum dot (QD) is a small region of material forming a quasi-zero-dimensional system. The "classical" material for quantum dots is a semiconductor heterostructure, where the dot is defined either vertically or laterally [Johnson92, Tarucha96,

Ashoori96, Kouwenhoven97, Kouwenhoven01]. Quantum dots can also be fabricated from semiconducting nanowires [Björk04], or from other materials such as metal nanoparticles [Ralph95, Petta01], superconducting materials [Ralph95], carbon nanotubes [Dekker99], graphene [Ponomarenko08, Stampfer08] or single molecules [Park02, Osorio07].<sup>1</sup> In order to investigate the electronic properties, the quantum dot is connected to leads via tunnel junctions. In such a setup, electrons can be exchanged with the environment via the leads. Additionally, a gate electrode is capacitively coupled to the dot, which allows for tuning its electrostatic potential. A circuit diagram representing a quantum dot connected with tunnel junctions (tunnel resistance  $R$  and capacitance  $C$ ) to source and drain and electrostatically ( $C_{\text{gt}}$ ) to a gate electrode is sketched in Fig. 4.1.

The low-dimensionality of quantum dots induces two predominant effects. First, the Coulomb repulsion between electrons causes an energy cost for adding an additional electron onto the dot – the charging energy  $E_C = e^2/C$ . Second, a discrete energy spectrum arises due to the spatial confinement. This energy spectrum leads to a behaviour similar to atoms and hence quantum dots are sometimes called "artificial atoms" [Kastner93].

In order to observe single-electron charging effects, two requirements have to be met. First, the charging energy of the dot has to be much larger than the thermal fluctuations

$$e^2/C \gg k_B T. \quad (4.1)$$

Second, the tunnel barriers must be sufficiently opaque, so that quantum fluctuations do not influence the number of electrons on the dot. A condition for the minimal tunnel resistance  $R$  of the barriers can be found by considering the Heisenberg uncertainty  $\Delta E \Delta t \sim h$ . The typical time to charge or discharge a capacitance is  $\Delta t = RC$  and with the requirement that  $\Delta E \ll e^2/C$  we obtain for the tunnel resistance

$$R \gg h/e^2. \quad (4.2)$$

To meet these two requirements, quantum transport measurements are performed at low temperatures and efforts are made to fabricate suitable contacts to the dot.

#### 4.1.1 The constant interaction model

Electrical measurements of a quantum dot setup as it is sketched in Fig. 4.1 can be understood employing a constant interaction model [Averin91, Beenakker91, Kouwenhoven97, Kouwenhoven01]. This model is based on two assumptions:

- (i) The Coulomb interactions between electrons are parameterized by a single, constant capacitance  $C$ . This includes interactions among the electrons on the

---

<sup>1</sup>In addition to this listing of electronically accessible quantum dots, self-assembled quantum dots made from e.g. CdSe or InAs/GaAs exist, which are optically accessible [Dabbousi95, Atatüre06].

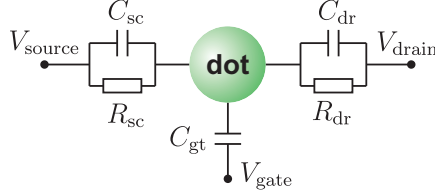


**Figure 4.1:** Circuit diagram of a quantum dot connected to two leads – source (sc) and drain (dr) – via tunnel barriers, represented by a capacitance  $C_{sc/dr}$  and a tunnel resistance  $R_{sc/dr}$ . A gate electrode is capacitively coupled to the dot ( $C_{gt}$ ). A bias voltage can be applied via  $V_{source}$  and  $V_{drain}$  and the electrostatic potential on the dot can be tuned by  $V_{gate}$ .

dot and also interactions between the electrons on the dot and the electrons in the environment. The capacitance is the sum of the capacitances to all leads  $C = C_{sc} + C_{dr} + C_{gt}$ .

- (ii) The discrete, single-particle energy spectrum, calculated for non-interacting electrons, is unaffected by the interactions and hence does not depend on the number of electrons on the dot.

Then, the total ground state energy  $U(N)$  of a dot with  $N$  electrons is

$$U(N) = \frac{(-|e|(N - N_0) + \sum_r C_r V_r)^2}{2C} + \sum_{n=1}^N E_n(B), \quad (4.3)$$

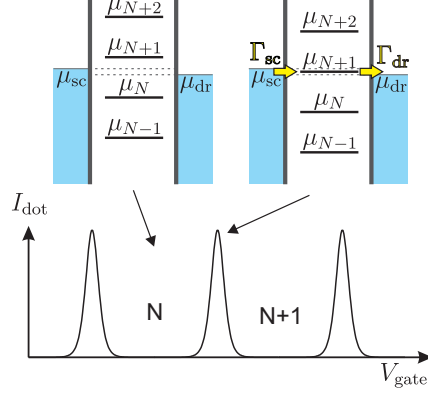
where  $r = sc, dr, gt$  denotes the leads and the gate electrode. The terms  $C_r V_r$  can be changed continuously in a quantum dot setup and represent an effective induced charge.  $-|e|N_0$  is the charge in the dot compensating the positive background charge originating from the donors in the heterostructure of semiconducting quantum dots. The last term is a sum over the occupied single-particle energy levels  $E_n(B)$ , which are specific for each quantum dot and can depend on a magnetic field. The electrochemical potential  $\mu_{dot}(N)$  of the dot is defined as

$$\mu_{dot}(N) \equiv U(N) - U(N - 1) = (N - N_0 - \frac{1}{2})E_C - \frac{E_C}{|e|} \sum_r C_r V_r + E_N. \quad (4.4)$$

Here,  $E_C = e^2/C$  is again the charging energy and  $E_N$  is the topmost filled single-particle state for an  $N$  electron dot. While the energy in Eq. 4.3 depends quadratically on the voltages  $V_r$ , the electrochemical potential varies linearly. Let us for the moment assume that the terms  $C_r V_r$  are considerably smaller for source and drain than for gate, which is mostly the case in experiments. Then, the quantized states of the electrochemical potential as depicted in the sketches of Fig. 4.2 can be moved by the gate voltage while the distance between the levels remains constant. However, deviations from the model can occur. The capacitances may depend on



**Figure 4.2:** Schematic of the quantized states of the electrochemical potential of a quantum dot. If there is no dot chemical potential aligned within the bias window, the number of electrons on the dot is fixed ( $N$ ) and it is in Coulomb blockade. No current can be measured. Increasing  $V_{\text{gate}}$  lowers the dot chemical potentials and when  $\mu_{N+1}$  aligns within the bias window, electrons tunnel with tunneling rates  $\Gamma_{\text{sc/dr}}$  across the dot and a non-zero current  $I_{\text{dot}}$  is measured.



the charge state and vary with the applied gate voltage, as it was observed for e.g. single-molecule quantum dots [Osorio07] or carbon nanotubes [Tans98a].

The addition energy  $E_{\text{add}}$  is the difference between the electrochemical potentials of two ground states

$$E_{\text{add}} \equiv \mu(N+1) - \mu(N) = E_C + \Delta, \quad (4.5)$$

and is independent of the number of electrons on the dot. It consists solely of the charging energy  $E_C$  and the energy spacing between two discrete quantum levels  $\Delta$ .

Quantum transport measurements study the current as a function of the applied voltages, i.e. the conductance across the quantum dot. The difference between the source and the drain voltage defines the applied bias voltage  $V_{\text{bias}} = V_{\text{source}} - V_{\text{drain}}$  and opens up an energy window between the electrochemical potentials of source and drain  $\mu_{\text{sc}} - \mu_{\text{dr}} = -|e|V_{\text{bias}}$ , called the bias window. Generally, transport across the quantum dot occurs if there are available states of the dot within the bias window.<sup>2</sup> In the following, the transport effects occurring in quantum transport measurements will be explained.

#### 4.1.2 Linear transport and Coulomb blockade

In the linear response regime, the source and the drain voltage are considered to be equal ( $V_{\text{source}} = V_{\text{drain}}$ ) and the current is measured as function of gate voltage. In an experiment, a very small bias voltage is applied for observing the explained effects. If no available state is aligned within the small bias window between  $\mu_{\text{sc}}$  and  $\mu_{\text{dr}}$ , as sketched in the left panel of Fig. 4.2, the number of electrons on the dot is fixed to  $N$  and no current flows across the dot. The system is in the so-called Coulomb blockade [van Houten92].

<sup>2</sup>This holds if co-tunneling and Kondo effects are neglected.

According to Eq. 4.4, increasing the gate voltage  $V_{\text{gate}}$  lowers the dot electrochemical potentials, and when  $\mu_{N+1}$  is aligned within the bias window, one electron can tunnel from the source onto the dot, increasing the number of electrons to  $N+1$ . After it has tunneled out to the drain, another electron can tunnel across the quantum dot via  $\mu_{N+1}$ . Such a cycle is called single-electron tunneling or sequential electron tunneling (SET). Tunneling rates  $\Gamma_{\text{sc}}$  and  $\Gamma_{\text{dr}}$  involved in these tunneling events are given by the properties of the tunnel barriers between the leads and the dot. In this regime, a non-zero conductance is measured. Increasing  $V_{\text{gate}}$  further lowers  $\mu_{N+1}$  below  $\mu_{\text{sc}}$  and  $\mu_{\text{dr}}$ , the electron cannot tunnel to the drain any more, and the dot is filled with one more electron. Sweeping the quantized states through the small bias window, the dot is subsequently filled with electrons, and the conductance measurement exhibits so-called Coulomb oscillations, plotted in Fig. 4.2. According to [Beenakker91], the Coulomb oscillations are visible at temperatures  $k_B T < 0.3e^2/C$  and when tunneling occurs through one single level, the lineshape of one conductance peak is given by

$$\frac{G}{G_0} = \frac{\Delta E}{4k_B T} \cosh^{-2} \left( \frac{\delta}{2.5k_B T} \right), \quad (4.6)$$

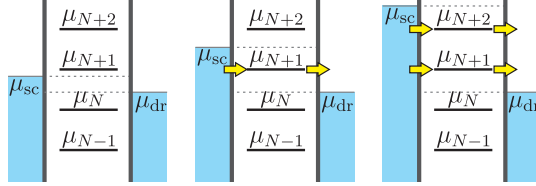
where  $\delta = e(C_{\text{gt}}/C) \cdot |V_{G_0} - V_G|$  measures the distance to the center of the peak (at  $V_{G_0}$ ) in units of energy. The prefactor  $\alpha_{\text{gt}} \equiv C_{\text{gt}}/C$  is the dimensionless coupling parameter of the gate, which converts the gate voltage to an energy. Equivalent coupling parameters  $\alpha_r \equiv C_r/C$  can be defined for source and drain. Using Eq. 4.6, the electron temperature can be extracted from quantum transport measurements.

### 4.1.3 Non-linear transport – the stability diagram

Another way to measure transport via the quantum dot is by applying a higher bias voltage. Keeping the gate voltage constant and increasing the bias voltage, the changes in the number of available states in the bias window can be monitored by the conductance. Whenever one additional dot level falls into the bias window, one more transport channel opens up and the current increases (see Fig. 4.3). Therefore, steps in  $I_{\text{dot}}$  are observed in a bias voltage sweep, a so-called Coulomb staircase.

Varying both the gate and the bias voltage, a conductance map can be constructed. The conductance plotted as function of gate and bias voltage forms a stability diagram. As sketched in Fig. 4.4, the diagram consists of diamond-shaped regions, where the number of electrons on the dot is fixed – the Coulomb diamonds. Outside the diamonds, the system is in the single-electron tunneling regime, where a non-zero current is measured. From the stability diagram, the addition energy  $E_{\text{add}}$  and the gate coupling parameter  $\alpha_{\text{gt}}$  can be extracted from the height and the width of the Coulomb diamonds, as indicated in Fig. 4.4. Since the charging energy is independent of  $N$ , a variation in the size of the diamonds reflects the characteristics of the single-particle energy levels of the particular quantum dot.

**Figure 4.3:** Schematic of the quantized states of the electrochemical potential of a quantum dot. At a small bias voltage (left panel), there is no dot chemical potential within the bias window and no electrons can tunnel across the dot. With increasing bias window, first one tunneling channel opens up (center panel), followed by more channels (right panel).



In general, the two slopes forming the edges of the Coulomb diamonds are not symmetric and depend on the dimensionless coupling parameters  $\alpha_r$ . Typically, the electrochemical potential of only one lead, e.g., the source, is changed, while the drain potential is kept fixed and grounded in experiments, i. e.,

$$\begin{aligned} V_{\text{drain}} &\equiv 0 \\ V_{\text{source}} &= V_{\text{bias}} = -|e|\mu_{\text{sc}}. \end{aligned} \quad (4.7)$$

Then, displaying  $I_{\text{dot}}$  as function of  $V_{\text{bias}}$  and  $V_{\text{gate}}$ , the slopes of the diamonds are given as

$$V_{\text{bias}} \propto \begin{cases} \frac{\alpha_{\text{gt}}}{1 - \alpha_{\text{sc}}} V_{\text{gate}} & \text{source resonance} \\ -\frac{\alpha_{\text{gt}}}{\alpha_{\text{sc}}} V_{\text{gate}} & \text{drain resonance} \end{cases} \quad (4.8)$$

The edge of the diamond with positive slope is the one where the dot level is aligned with  $\mu_{\text{sc}}$  and hence called source resonance. Along the diamond edge with negative slope, the level is aligned with  $\mu_{\text{dr}}$  and called drain resonance. Typically, not the dot current, but the differential conductance  $dI_{\text{dot}}/dV_{\text{bias}}$  is plotted in a stability diagram. Each change in the dot current will appear as a resonance line in the  $dI/dV$  plot. According to Eq. 4.8, the coupling parameters  $\alpha_r$  of a quantum dot can be extracted from its stability diagram.

Up to now, we only considered ground state (GS) energies of the quantum dot, but transitions involving excited states of the single-particle energy spectrum can also be observed in a stability diagram. One example is shown in Fig. 4.5. In the inset of the figure, we plot the possible transitions involving excited states (ES). These transitions are found as resonance lines running parallel to the diamond edges in the SET region of the stability diagram. The energy-level spacing can be extracted from the bias window at the meeting point of an excited state resonance line with a diamond edge.

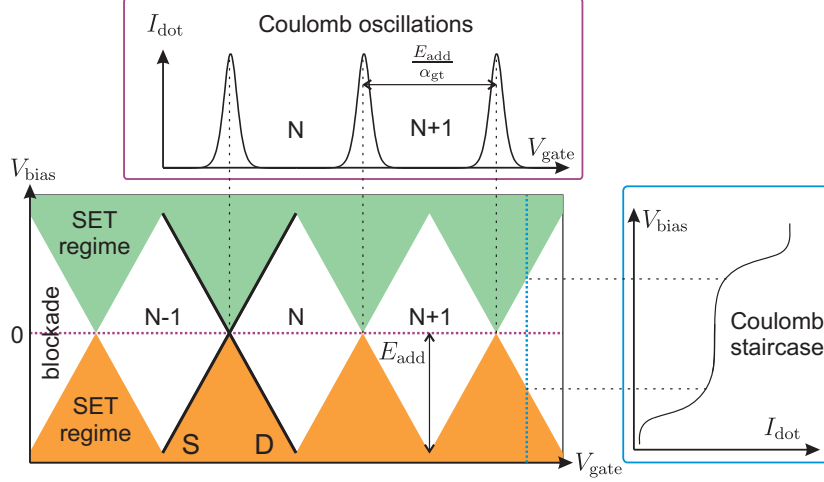


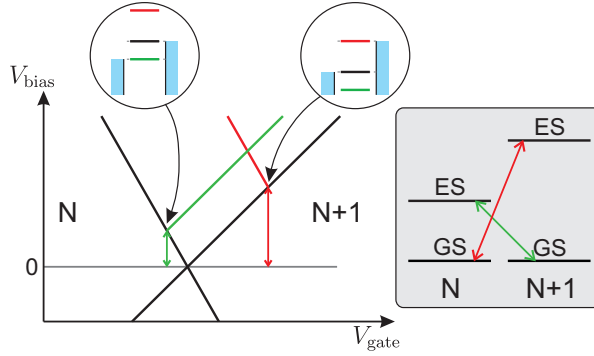
**Figure 4.4:** Schematic stability diagram of a quantum dot. The dot current  $I_{\text{dot}}$  is plotted as function of the bias and the gate voltage ( $V_{\text{bias}}$ ,  $V_{\text{gate}}$ ). Coulomb oscillations are observed along the purple line and a Coulomb staircase along the blue line. The stability diagram consists of white Coulomb diamonds, where the dot is blocked for transport. Outside the diamonds, in the single-electron tunneling (SET) regime, electrons tunnel sequentially across the dot and a current is observable (green and orange). The distance from  $V_{\text{bias}} = 0$  to the diamond tips is the addition energy  $E_{\text{add}}$ .  $E_{\text{add}}$  and the gate coupling parameter  $\alpha_{\text{gt}}$  also determine the width of the diamonds.

In summary, it is possible to fully characterize a quantum dot from its stability diagram. The capacitances which couple the dot to the environment can be determined, as well as the quantum level structure and the excited state spectrum.

## 4.2 Carbon nanotubes as quantum dots

Fundamental properties of carbon nanotubes have been discussed in chapter 2. Here, we describe characteristics of carbon nanotubes when they are structured to form quantum dots. The first quantum dots from carbon nanotubes were realized by Bockrath *et al.* and Tans *et al.* in a rope [Bockrath97] and an individual nanotube [Tans97], respectively. The devices are fabricated in a three-terminal configuration. First, the nanotubes are located on the substrate by AFM imaging and subsequently, contacts designed for particular nanotubes are fabricated on top. The usual contact

**Figure 4.5:** Schematic  $dI_{\text{dot}}/dV_{\text{bias}}$  diagram as function of  $V_{\text{bias}}$  and  $V_{\text{gate}}$ . The green and red lines are the resonances of the corresponding transitions shown in the inset involving excited states of two different charge states on the quantum dot. At the positions where the lines meet with the diamond edge, the energy-level spacing can be extracted.



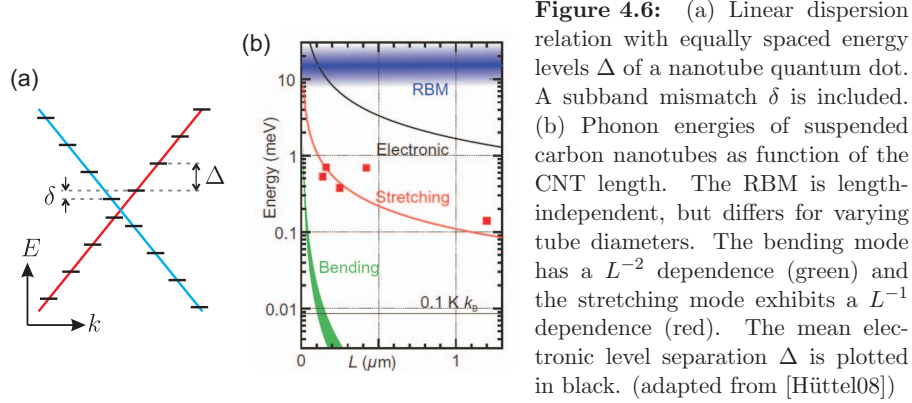
material is gold<sup>3</sup>, which forms tunnel barriers at low temperatures. This device geometry corresponds to the schematic circuit diagram sketched in Fig. 4.1. The separation of the two contacts and hence the length of the nanotube dot is typically between 100 nm and 1  $\mu\text{m}$ . Typical addition energies are a few meV, depending on the length of the nanotube.

The fourfold degenerate band structure of nanotubes is reflected in quantum transport by a fourfold periodicity of the addition energy [Cobden02]. When a quantum dot is formed, the quantization along the nanotube axis leads to a set of equally spaced single-particle states (see Fig. 4.6a). To describe carbon nanotube quantum dots, the constant-interaction model has been extended by additional parameters [Oreg00, Sapmaz05]. Then, the model includes the known charging energy  $E_C$ , the quantum energy-level separation  $\Delta$ , the splitting  $\delta$  between the two subbands, the exchange energy  $J$  and the excess Coulomb energy  $dU$ , which corrects the charging energy when a subband is doubly occupied. The fourfold degeneracy is often observed to be lifted ( $\delta \neq 0$ ). The quantum energy-level spacing, which is usually the largest contribution to the addition energy, can be estimated from the length of the nanotube [Tans97]

$$\Delta = \frac{\hbar v_F}{2L}, \quad (4.9)$$

where  $\hbar$  is the Planck constant,  $v_F = 8.2 \times 10^5 \text{ ms}^{-1}$  is the Fermi velocity of carbon nanotubes [Lemay01] and  $L$  the length of the contacted nanotube. Usually, the exchange energy and the excess Coulomb energy are small compared to the other energies [Sapmaz05]. For a complete analysis of the electronic spectrum, at least two resonances involving excited states are necessary [Sapmaz05].

<sup>3</sup>Other possible materials are platinum, palladium or tungsten alloys. Ferromagnetic [Sahoo05] and superconducting [Grove-Rasmussen09] contacts have been studied as well.



Creating tunnel barriers to the nanotube quantum dot by the resistance of the contact is easy, but the tunnel resistance for a particular device is unpredictable and not tunable. It varies with the particular interface properties, i. e. the coating of the nanotube [Zhang00], and depends on the work function mismatch when Schottky barriers are formed at the interface between a metal contact and a semiconducting nanotube [Heinze02, Kim05]. Furthermore, this device setup lacks the possibility of fabricating multi-dot devices, where electrons tunnel via several serial quantum dots. Tunable quantum dots in nanotubes can be fabricated by depositing metallic gates isolated by a dielectric layer on top of a nanotube [Mason04, Biercuk05, Sapmaz06b, Gräber06]. The top gates are used to produce localized depletion regions in the nanotube, by which the quantum dot is defined. The voltages of the top gates tune the transparencies of the tunnel barriers and also the electrostatic energy within the quantum dot, comparable to the tuning of lateral semiconductor quantum dots.

As molecules, carbon nanotubes are susceptible to environmental effects and interactions with their surrounding. In contrast to quantum dots formed in semiconductor heterostructures, these molecular interactions can arise in quantum transport and complicate the stability diagram of carbon nanotube quantum dots. One example is the observation of phonon-assisted tunneling in devices where the nanotubes are freestanding [Sapmaz06a, Leturcq09]. The origin of this tunneling effect is the electron-phonon coupling which was already discussed with regard to Raman scattering in section 2.3.2. The accessible energy in transport measurements, however, limits the number of phonon modes that are possible to observe (see Fig. 4.6b). From the vibrational modes discussed in section 2.3.2, only the radial breathing mode has an energy small enough to be excited by electronic transport, which has been observed by tunneling via an scanning tunneling microscopy (STM) tip [LeRoy04]. The energy of the bending and the stretching mode of a suspended nanotube is lower

than the RBM energy and depends on the suspended length. Both modes have been observed in three-terminal devices [Sapmaz06a, Leturcq09, Hüttel09b, Hüttel09a].

This example illustrates that the carbon nanotube stability diagram can become very complex due to the molecular character of the system. The previous chapter 3 concentrated on the vibrational properties of a rope of carbon nanotubes and probed molecular interactions using Raman spectroscopy. Similar interactions may arise in quantum transport of the rope and are the subject of the following section, where a model of interacting parallel quantum dots is developed and employed in transport calculations using master equations.

### 4.3 Model of interacting parallel quantum dots

#### 4.3.1 Master equation modeling

The current through a quantum dot system can be calculated using a master equation model employing the constant interaction picture. The following general description of the model Hamiltonian and the master equation approach for the calculation of single electron transport follows closely the presentation by Bruus and Flensberg in [Bruus04] and is also reported in [Smerat11]. It is not yet specified to a particular quantum dot setup.

##### The model Hamiltonian

The Hamiltonian describing the whole quantum dot setup can be written as

$$H = H_L + H_R + H_D + H_T, \quad (4.10)$$

where  $H_{L/R}$  denotes the left lead (source) and the right lead (drain) Hamiltonian, respectively.  $H_D$  is the dot Hamiltonian, a many-body Hamiltonian containing the specific properties of the quantum dot system, which has to be diagonalized.  $H_T = H_{TL} + H_{TR}$  is the tunnel Hamiltonian consisting of tunneling to/from the left lead ( $H_{TL}$ ) and to/from the right lead ( $H_{TR}$ ).  $H_{TL}$  is given by:

$$H_{TL} = \sum_{\nu_L, \nu_D} (t_{L, \nu_L, \nu_D} c_{\nu_L}^\dagger c_{\nu_D} + t_{L, \nu_L, \nu_D}^* c_{\nu_D}^\dagger c_{\nu_L}). \quad (4.11)$$

Here  $c_{\nu_L}^{(\dagger)}$  annihilates (creates) an electron in the state  $|\nu_L\rangle$  in the left lead and  $c_{\nu_D}^{(\dagger)}$  annihilates (creates) one in the state  $|\nu_D\rangle$  on the dot.  $t_{L, \nu_L, \nu_D}$  is the corresponding tunnel matrix element from the dot to the lead and  $t_{L, \nu_L, \nu_D}^*$  is the one from the lead to the dot.  $H_{TR}$  is defined correspondingly. The left lead Hamiltonian is defined as

$$H_L = \sum_{\nu_L} \epsilon_L c_{\nu_L}^\dagger c_{\nu_L}, \quad (4.12)$$

where  $\epsilon_L$  is the energy of the state  $|\nu_L\rangle$ . The right lead Hamiltonian is defined correspondingly.

### The master equations of single electron transport

The goal of the calculations is to find the probability  $P(\alpha)$  for the general state  $|\alpha\rangle$  in which the system resides. In equilibrium, the probability is given by the Boltzmann distribution, whereas in non-equilibrium, the tunneling rates into all states have to be considered. Since the tunneling rates are small (we assume sequential tunneling), coherent processes corresponding to higher order tunneling processes are suppressed. Hence, we can limit the calculations to the first order in the tunneling rates described by Fermi's Golden Rule. The rate of a tunnel event from a state  $|\nu_D\rangle$  on the dot into a state  $|\nu_L\rangle$  in the left lead is then given by

$$\Gamma_{\nu_L \leftarrow \nu_D}^L = 2\pi \sum_{f_{\nu_L}, i_{\nu_D}} |\langle f_{\nu_L} | H_{TL} | i_{\nu_D} \rangle|^2 W_{i_{\nu_D}} \delta(E_{f_{\nu_L}} - E_{i_{\nu_D}}), \quad (4.13)$$

where  $|i_{\nu_D}\rangle$  is an initial state and  $|f_{\nu_L}\rangle$  a final state with eigenenergies  $E_{i_{\nu_D}}$  and  $E_{f_{\nu_L}}$ .  $W_{i_{\nu_D}}$  is the thermal distribution function of the leads, i. e. the Fermi function. Equation 4.13 can be specified with regard to an arbitrary quantum dot considering single many-body states. Such calculations are beyond the scope of this thesis and detailed information can be obtained from [Smerat11].

After determining the rates, the master equation can be formulated as

$$\frac{d}{dt}P(\nu_D) = - \sum_{\nu_L} \Gamma_{\nu_L \leftarrow \nu_D} P(\nu_D) + \sum_{\nu_L} \Gamma_{\nu_D \leftarrow \nu_L} P(\nu_L), \quad (4.14)$$

where the first term on the right side describes the tunneling out of state  $|\nu_D\rangle$  and the second term describes the tunneling into state  $|\nu_D\rangle$ . This description has to be regarded as a semi-classical equation, because the probabilities involved are classical probabilities. For the calculation, we are only interested in the steady state of the system, i. e., we set

$$\frac{d}{dt}P(\nu_D) \equiv 0. \quad (4.15)$$

Under the restriction  $\sum_{\nu_D} P(\nu_D) = 1$ , this set of linear equations is solved numerically. To do so, the tunnel matrix elements have to be put in manually and demand reasonable estimates.

Transport calculations employing this method successfully interpreted complicated stability diagrams of single-molecule quantum dots [Heersche06, Osorio07] and carbon nanotube quantum dots [Hüttel09b]. Now, the master equation modeling will be used to calculate the tunneling through interacting parallel quantum dots, as will be shown in the following section. Calculations of stability diagrams shown in this work are performed by S. Smerat, M. Leijnse and M. R. Wegewijs.



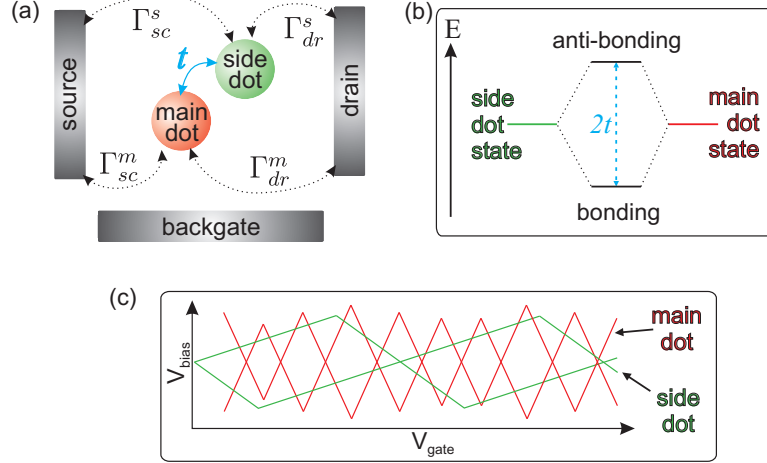


**Figure 4.7:** (a) Sketch of the transport model: Two QDs are contacted in parallel with different gate coupling strengths. Electrons tunnel with rates  $\Gamma$  from the leads onto and out of the QDs. The QDs are connected by a hybridization with an amplitude  $t$ . (b) The hybridization of two orbitals generates a bonding and an anti-bonding eigenstate with a gap of  $2t$ . (c) Sketch of two overlaying diamond patterns formed by two differently gate-coupled, parallel QDs: a strongly gate-coupled main dot and a weakly gate-coupled side dot.

### 4.3.2 Transport via interacting parallel quantum dots

The calculations consider the model sketched in Fig. 4.7a, where two quantum dots are contacted in parallel. We assume a different gate coupling strength for the two dots. A similar model has been used by Eliassen *et al.* to explain the quantum transport in a peapod device [Eliassen10]. In general, this setup leads to a stability diagram with two overlaying patterns of Coulomb diamonds as sketched in Fig. 4.7c. One pattern contains small diamonds originating from a quantum dot referred to as the main dot (indexed  $m$ ) from here on. Because of the weaker gate coupling of the side dot (indexed  $s$ ), the second diamond pattern contains larger diamonds (see Eq. 4.8). The different gate couplings allow for a tunability of the parallel quantum dots which will be discussed in detail in section 4.3.3.

The quantum dots are described within the constant interaction model extended by the characteristics for carbon nanotubes [Oreg00, Sapmaz05] as introduced in section 4.2. Within this model, the energy of a state on one carbon nanotube quantum dot  $i$  is

$$E^i = \sum_{\tau,l,\sigma} \epsilon_{l\tau} n_{\tau,l,\sigma}^i + E_C^i (N^i)^2 + dU \sum_{\tau,l} n_{\tau l \uparrow}^i n_{\tau l \downarrow}^i + J \sum_{\tau,\tau'} N_{\tau \uparrow}^i N_{\tau' \downarrow}^i, \quad (4.16)$$

#### 4.3. MODEL OF INTERACTING PARALLEL QUANTUM DOTS

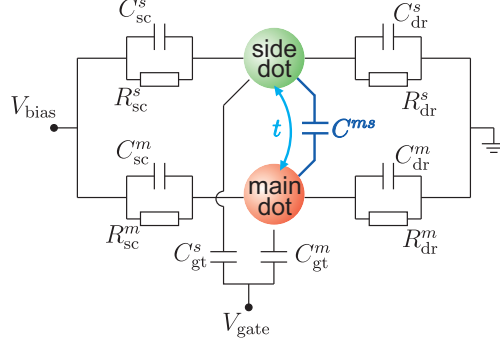


**Figure 4.8:** Circuit diagram representing the parallel quantum dots and their interactions by which they are characterized. A tunnel barrier (consisting of a capacitance  $C_{sc/dr}^i$  and a resistance  $R_{sc/dr}^i$ ) connects dot  $i$  to the leads. A capacitive coupling to the back gate is denoted by  $C_{gt}^i$  and the capacitive coupling between the dots by  $C^{ms}$ . Additionally, tunneling between the two dots is denoted by the hybridization amplitude  $t$ .

where  $l$  denotes the states on subband  $\tau = A, B$  and  $\sigma = \uparrow, \downarrow$  is the spin index.  $n_{\tau,l,\sigma}^i$  is the number of electrons on the nanotube in state  $l$  on subband  $\tau$  with spin  $\sigma$ . The orbital energy is

$$\epsilon_{l\tau} = \begin{cases} l \cdot \Delta & \tau = A \\ l \cdot \Delta + \delta & \tau = B \end{cases}, \quad (4.17)$$

where  $\Delta$  is the quantum energy level spacing and  $\delta$  is the subband mismatch.  $E_C^i$  is the charging energy and  $N^i = \sum_{\tau,l,\sigma} n_{\tau,l,\sigma}^i$  is the total number of electrons.

Each dot contributes an energy according to Eq. 4.16 to the energy in a system of two parallel, but non-interacting quantum dots:

$$E = E^m + E^s. \quad (4.18)$$

Following the experimental situation, calculations are performed according to an asymmetrically applied bias voltage, i. e., the drain electrode is grounded and the full bias voltage is applied to the source electrode (see Eq. 4.7). The electrochemical potential  $\mu_\nu^i$  for adding an electron to orbital  $\nu$  on dot  $i$  depends on the specific, initial many-body state of the system given in Eq. 4.16, and always depends linearly on the voltages:

$$\mu_\nu^i \propto -|e|\alpha_{sc}^i V_{bias} - |e|\alpha_{gt}^i V_{gate}, \quad (4.19)$$

where  $\alpha_{sc,gt}^i = C_{sc,gt}^i/C^i$  is the capacitive coupling strength of dot  $i$  to the source and the gate electrode and  $C^i$  is the capacitance of the dot according to the constant interaction model (cf. section 4.1.1). This term describing the bias and gate voltage dependence of the energy of a state adds to the energy given in Eq. 4.18.

A capacitive coupling between the two dots is introduced to the model via a charging term  $U^{ms} n_{\tau,l,\sigma}^s n_{\tau,l,\sigma}^m$  added to the energy in Eq. 4.18. This leads to an additional energy contribution for any state which has electrons on both the main dot and the side dot.

The model is additionally extended to account for a finite hybridization integral  $t$  between many-body states of the two dots, thus allowing electrons to hop between

the quantum dots. The phenomenon of hybridization is well-known in molecular physics, where atomic orbitals hybridize to form molecular orbitals. A hybridization of states is introduced as off-diagonal matrix elements in the Hamiltonian:

$$H = \begin{pmatrix} \ddots & & & & \\ & E_j(V_{\text{bias}}, V_{\text{gate}}) & \cdots & & t_{jk} \\ & \vdots & \ddots & & \vdots \\ & t_{jk} & \cdots & E_k(V_{\text{bias}}, V_{\text{gate}}) & \\ & & & & \ddots \end{pmatrix}. \quad (4.20)$$

Here  $E_j(V_{\text{bias}}, V_{\text{gate}})$  and  $E_k(V_{\text{bias}}, V_{\text{gate}})$  hybridize with the hybridization amplitude  $t_{jk}$ . When two hybridizing states are in resonance, a bonding and an anti-bonding state is created with an energy gap of  $2t$ , which is sketched in Fig. 4.7b. As a result of the differential gating effect,  $E_j(V_{\text{bias}}, V_{\text{gate}})$  and  $E_k(V_{\text{bias}}, V_{\text{gate}})$  depend differently on  $V_{\text{bias}}$  and  $V_{\text{gate}}$ , thus allowing us to tune the energies into resonance (see section 4.3.3).

The circuit diagram in Fig. 4.8 sketches how the parallel quantum dots interact with the environment. It shows the setup of two parallel quantum dots connected to source and drain leads via a tunnel barrier represented by a capacitance  $C_{\text{sc/dr}}^i$  and a resistance  $R_{\text{sc/dr}}^i$ , where only the capacitance plays a role for the coupling.  $C_{\text{sc/dr}}^i$  together with the capacitive coupling to the back gate  $C_{\text{gt}}^i$  define the slopes of the diamond patterns in the stability diagram (see Eq. 4.8). The effect of the additional interactions, the capacitive inter-dot coupling via the capacitance  $C^{ms}$  and the tunnel coupling via the hybridization amplitude  $t$ , will be shown by the following transport calculations.

A stability diagram calculated according to our model is shown in Fig. 4.9. A Coulomb diamond originating from the main dot is visible. A secondary resonance with a small slope crosses the Coulomb blocked region as part of the second diamond pattern originating from the side dot. When two resonance lines originating from different dots but with the same sign of the slope, meet within the stability diagram, the energy levels are aligned with one of the leads (cf. section 4.1.3) and at resonance with each other. Then, anticrossings with a gap between a bonding and an anti-bonding state appear, if the hybridization amplitude is significant compared to thermal and tunnel broadening. The calculations include only thermal broadening, while tunnel broadening is neglected. If the hybridization were negligible compared to thermal and tunnel broadening, the conduction lines should show a crossing at the diamond edges, as observed for molecules contacted in parallel [Osorio07, Osorio10].

The impact of the capacitive coupling between the two dots through the inter-dot charging energy  $U^{ms}$  is also visible in Fig. 4.9. With each Coulomb diamond, proceeding in the positive  $V_{\text{gate}}$  direction, the main dot is charged with an additional electron. This leads to a discrete change in the electrostatic potential on the side dot and thus to a voltage offset in the stability diagram, as can be seen in Fig. 4.9.

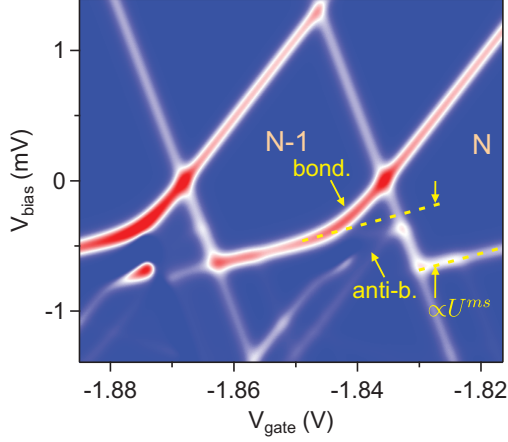


**Figure 4.9:** Calculated stability diagram using the model of Fig. 4.7a. The bonding and anti-bonding state at the anticrossing gap and the voltage offset due to the capacitive coupling  $U_{ms}$  are indicated.

### 4.3.3 The differential gating effect

Although the parallel configuration of two quantum dots differs substantially from the serial one, an analogy can be drawn. For a serial double quantum dot system, usually a conductance map is plotted versus two gate voltages, which couple differently to the dots. The result is a honeycomb pattern of specific charge states on the quantum dot system.

In our case, we have only one gate electrode acting on both dots, yet with a different coupling strength. We can use the conductance map plotted versus the bias and the gate voltage to specify charge states on the parallel quantum dot system within the Coulomb diamond patterns, as it is sketched in Fig. 4.10. In the sketch, we consider only ground states and neglect all couplings between the two quantum dots. We want to stress here that this is considered to be a high-bias measurement where the charge states are not equilibrium electron numbers on the quantum dots in contrast to the honeycomb conductance map.

Starting in the  $|N, M\rangle$  configuration with a fixed number of electrons on either dot at a given bias voltage, the gate voltage can be changed so that the main dot diamond edge is crossed and one electron can tunnel via the main dot ( $|N+1, M\rangle$ ). Increasing the bias voltage instead of the gate voltage starting from the  $|N, M\rangle$  configuration, will allow tunneling of an electron via the side dot as soon as the bias voltage crosses the secondary resonance (side dot diamond edge). From either configuration with one additional electron on the parallel dot system, the voltages can be adjusted to drive the system into a configuration with one electron on each dot ( $|N+1, M+1\rangle$ ). Hence, charges can be added selectively to the parallel quantum dots due to the differential gating effect by adjusting the gate and bias voltages. This

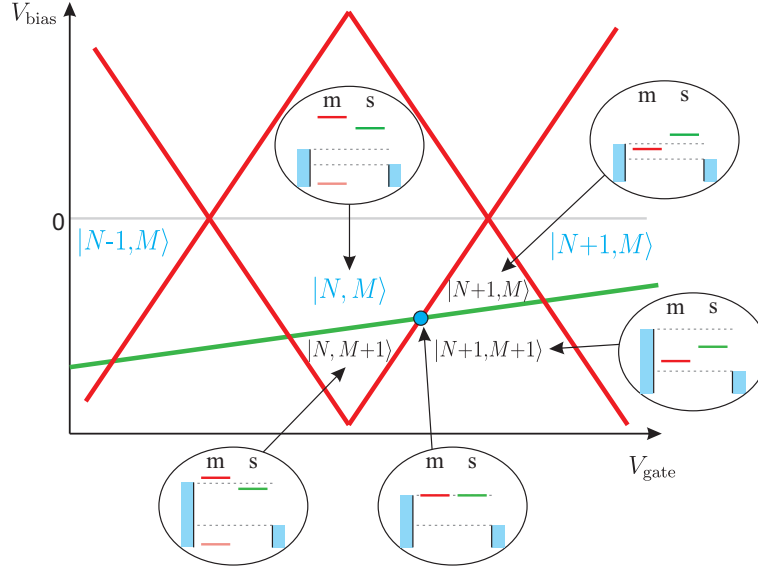


**Figure 4.10:** Sketch of the conductance map for a strongly gate coupled main dot  $m$  (red diamonds) and a weakly gate coupled side dot  $s$  (green secondary resonance). The charge states  $|m, s\rangle$  are indicated, where only those in blue denote equilibrium electron numbers. The level alignment is depicted for particular charge states.

allows for tuning to different configurations of the quantum dot system, including the configurations where states on the dots are at resonance and the hybridization properties can be investigated. Thus, employing differential gating, quantum transport can be used as a spectroscopic tool to probe the interactions between the parallel quantum dots.

## 4.4 Conclusions

This chapter addressed the physics of quantum dots and in particular of carbon nanotube quantum dots. The constant interaction model forms the basis for understanding the stability diagram obtained in quantum transport measurements. Within the framework of master equations, a model was developed containing two quantum dots which are contacted in parallel. Assuming one dot – the side dot – being weakly gate-coupled, the stability diagram shows a Coulomb diamond pattern originating from the main dot and secondary resonances as part of a second diamond pattern originating from the side dot. To account for the molecular nature of carbon nanotubes, the model includes two different kinds of interaction between the parallel

---

#### 4.4. CONCLUSIONS

quantum dots, a capacitive coupling and a tunnel coupling. The manifestations of these interactions in the calculated stability diagrams are not peculiar to carbon nanotubes, but can readily be transferred to any kind of molecular quantum dots. The differential gating effect inherent to our model allows for tuning to particular dot configurations and in that manner probing the molecular interactions by quantum transport spectroscopy.



## 5 Electronic setup for quantum transport measurements

The observation of single electron tunneling in the electron transport through quantum dot devices requires an elaborate electronic setup built in a cryostat, necessary for device cooling. The dot currents depend on the particular tunneling rates of the device and usually demand a current noise level of less than a few picoamperes. Complex noise filtering techniques and an appropriate implementation of voltage sources and sourcemeters are crucial in order to obtain these noise levels.

This chapter describes the setup for electronic measurements of quantum dot devices cooled in a dilution refrigerator, which was improved within the framework of this thesis for the measurements of single electron tunneling shown in chapter 6 and chapter 7.

### 5.1 Electrical characterization at room temperature

At room temperature, carbon nanotubes exhibit either metallic or semiconducting behaviour depending on their chirality. For characterizing the contacted nanotubes at room temperature, an electrical probe station has been set up within this work. The lithographically patterned bonding pads can be contacted via tungsten probes with a  $7\text{ }\mu\text{m}$  tip radius, which are part of a Süss MicroTec DC probe analyzer (EP6). The probe is enclosed within a shielding to reduce external noise coupling into the system and is connected to the sourcemeters (Keithley 2400, Keithley 2420) via triaxial cables. Two probes are connected as source and drain electrodes to apply a bias voltage and measure the current. Additionally, a gate voltage can be applied with a third probe. In this manner, bias and gate voltage sweeps can be performed, which characterize the nanotube devices before cooling down. The noise level of the system is  $\sim 0.2\text{ nA}$  without any noise filtering implemented.



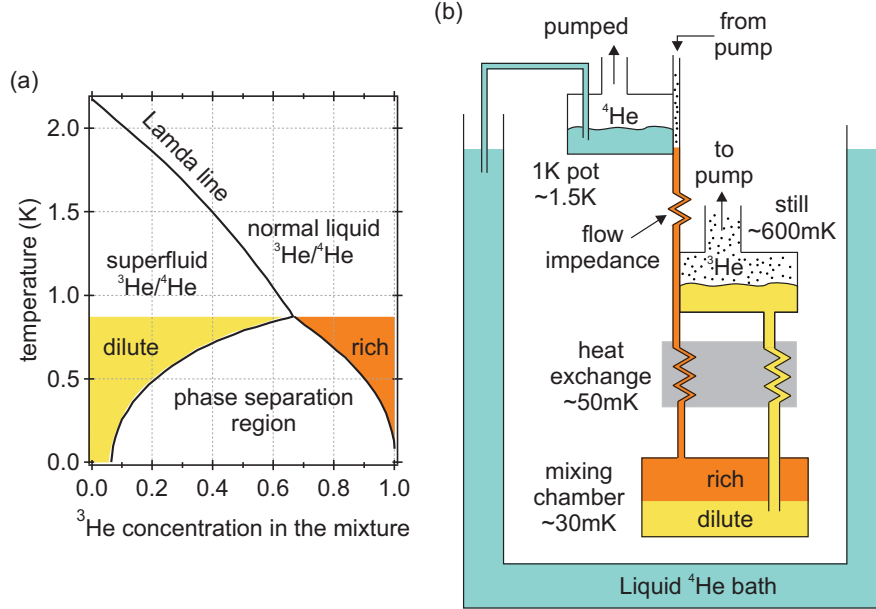


**Figure 5.1:** (a) Phase diagram of a  $^3\text{He}$ - $^4\text{He}$  mixture [Pobell96]. Below  $T \approx 870$  mK, the mixture separates in a  $^3\text{He}$ -rich (orange) and a  $^3\text{He}$ -dilute (yellow) phase. (b) Schematic drawing of the  $^3\text{He}$  pump cycle in a dilution refrigerator. Blue denotes liquid  $^4\text{He}$ .

## 5.2 Low-temperature electrical transport setup

For the observation of quantized charge tunneling, the device has to be cooled down to low temperatures (see section 4.1). Generally, Coulomb blockade in carbon nanotubes can be observed from  $\sim 4$  K downwards. However, in order to resolve individual energy levels, especially excited states, a lower temperature is necessary. A dilution refrigerator provides temperatures in the millikelvin range. In the following, the low-temperature transport setup will be discussed, which was employed and further developed to obtain quantum transport measurements.

### 5.2.1 Device cooling

The refrigeration process of a dilution refrigerator uses a mixture of  $^4\text{He}$  and  $^3\text{He}$ .<sup>1</sup> The mixture of these two isotopes of He undergoes a spontaneous phase separation below  $T \approx 870$  mK into a  $^3\text{He}$ -rich phase and a  $^3\text{He}$ -poor phase (the dilute

<sup>1</sup>An elaborate discussion about dilution refrigerators can be found in [Pobell96].

phase, hence the name dilution refrigerator), as can be seen in the phase diagram in Fig. 5.1a. The mixture is condensed in the mixing chamber of a dilution refrigerator and  $^3\text{He}$  is continuously removed from the  $^3\text{He}$ -poor phase by pumping (see Fig. 5.1b). Consequently,  $^3\text{He}$  atoms are forced to cross the phase boundary and move from the  $^3\text{He}$ -rich into the dilute phase, because this phase contains a minimum amount of  $^3\text{He}$  (6.6%) even at absolute zero temperature. This process is endothermal and hence cools the system. Typically, base temperatures of  $T_b = 8 - 10$  mK can be achieved.

A distinct pumping of  $^3\text{He}$  from the dilute phase is performed in the still at  $\sim 600$  mK and is possible, because of a higher vapour pressure for  $^3\text{He}$  in comparison to  $^4\text{He}$ . Proceeding in the cycle, the vapour phase  $^3\text{He}$ , which has been pumped from the still, is cooled to  $\sim 1.5$  K at the so-called 1K pot and passes a flow impedance, where a sufficient pressure is established to condense it again. The liquified  $^3\text{He}$  flows through two more heat exchangers to be pre-cooled to a low enough temperature, before it enters the mixing chamber again in the  $^3\text{He}$ -rich phase.

We use a Minikelvin 126-TOF dilution refrigerator (MNK126-700) from Leiden Cryogenics B.V. with a cooling power of  $700 \mu\text{W}$  at 120 mK.<sup>2</sup> The base temperature is  $\sim 30$  mK with the coldfinger (containing filters and samples) attached to the mixing chamber. For operation, the components of the dilution refrigerator are surrounded by two radiation shields enclosed within the inner vacuum chamber (IVC) at a pressure  $\sim 10^{-5}$  mbar. The whole insert resides in a liquid  $^4\text{He}$  bath. Superconducting coils surrounding the sample chamber allow for applying magnetic fields up to 12 T.

### 5.2.2 Measurement electronics and filtering

A typical measurement of a quantum dot device involves applying a bias voltage at the source/drain contacts and a voltage to one or more gate contacts while measuring the current across the device (see section 4.1). The electrical diagram of the setup is drawn in Fig. 5.2. In our case, the bias voltage is applied asymmetrically, i. e. the drain electrode is grounded and the full bias voltage is applied to the source electrode. We use an QT-IVVI-rack designed at the Delft University of Technology, containing optical digital-to-analog converters (DACs), a voltage source and a current-to-voltage (IV) converter. The whole electronic setup at the sample side is battery-powered and decoupled from external noise by using optical isolation in the voltage source (source side) as well as in the IV converter (drain side). This way, the sample is galvanically isolated from the environment.

All voltages used in the experiment are generated at the DAC box. The polarity of the DACs is set manually to one of three settings (negative:  $-4 \text{ V} \dots 0 \text{ V}$ ; bipolar:  $-2 \text{ V} \dots +2 \text{ V}$ ; positive:  $0 \text{ V} \dots +4 \text{ V}$ ). DAC values are set via an optical fiber link,

---

<sup>2</sup>The cooling power can be adjusted by heating the still.

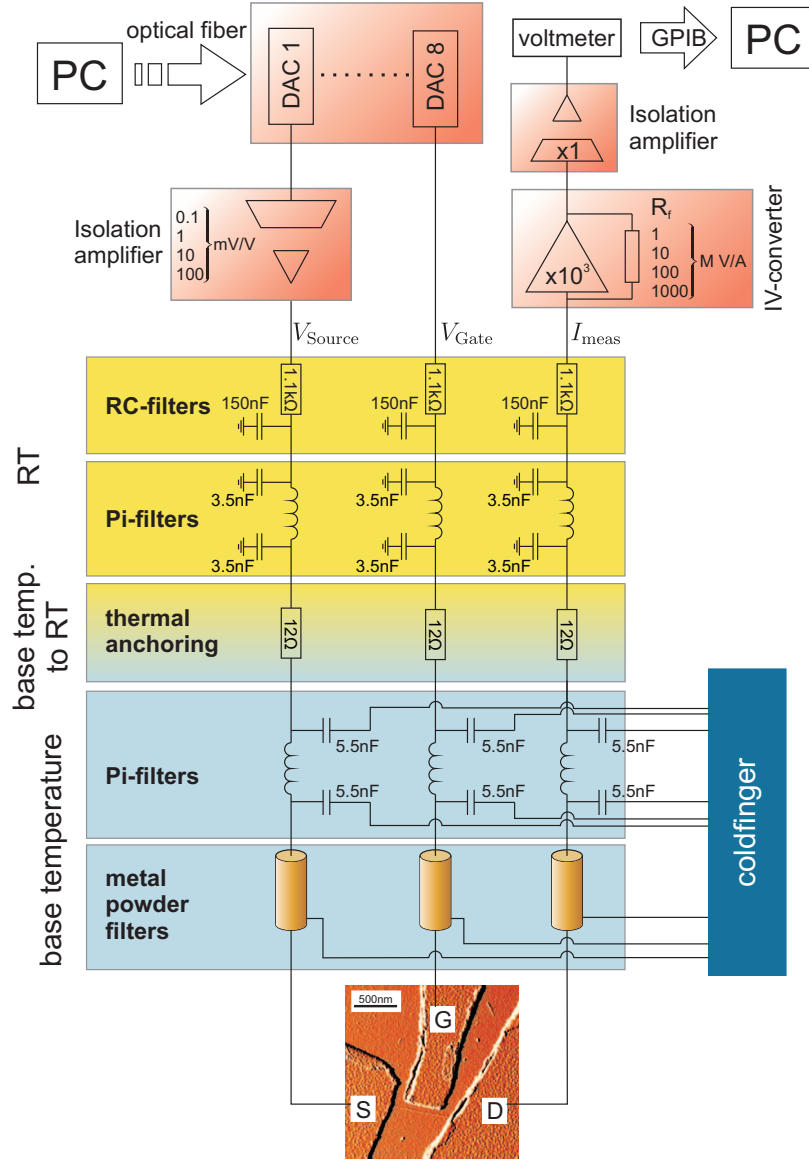


**Figure 5.2:** Electrical circuit for measurements in the dilution refrigerator. Voltages are applied to the gate electrodes, and a voltage-biased current measurement is performed.

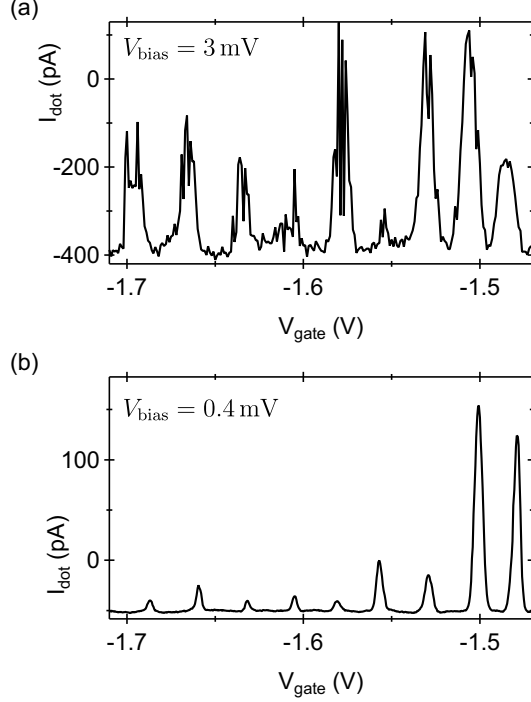
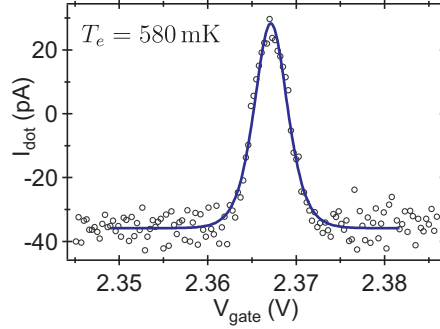


**Figure 5.3:** (a) Current through a carbon nanotube quantum dot with high noise level. A signal is only obtained with high  $V_{\text{bias}}$ . (b) Similar measurement on the same device with improved electronic setup. Coulomb oscillations are visible at low  $V_{\text{bias}}$ .

which is connected to the user computer. The isolation amplifier of the voltage source offers several conversion factors (0.1...100 mV/V) for the bias voltage to be applied at the source. At the drain side of the sample, the current passing through the device is converted to a voltage via a low bandwidth IV converter with an adjustable feedback resistance of  $R_f = 1 \text{ M}\Omega \dots 1 \text{ G}\Omega$ . The amplifier gain  $A$  is chosen to be  $10^3$ , setting the input resistance fixed, but dependent on  $R_f$  to  $R_{\text{in}} = R_f/A$ . The isolation amplifier does not amplify the signal further, but only decouples the sample optically from the measurement devices. The converted voltage is then measured via a digital voltmeter, that is read out by a computer. The general ground is defined at the coldfinger to avoid ground loops as a noise source. Also, the entire dilution refrigerator is electrically disconnected from any other possible ground definition by using plastic pump line connections.

Although the sample is at a base temperature of around 30 mK, the electron temperature in the device is usually higher. Mostly, the electrons are cooled via the DC wires, which are connected to the source and drain contacts. These wires are thermally anchored at several temperature stages (1K pot, still, 50 mK plate, mixing chamber). However, the electrons are heated by the noise, that couples in via the

**Figure 5.4:** Current through a carbon nanotube quantum dot as a function of  $V_{\text{gate}}$  at  $V_{\text{bias}} = 0.15$  mV. The electron temperature  $T_e$  is obtained by a fit of the Coulomb peak according to Eq. 4.6.



DC wires. In order to suppress this noise, several filtering stages are introduced as drawn in Fig. 5.2.

All wires are equally filtered with three types of filters and can be connected to source/drain contacts or gate contacts. Starting at room temperature, the low-frequency noise is removed by an RC-filter with a cut-off at 1 kHz and Pi-filters block noise in the medium-frequency range of 10-100 MHz. Additional Pi-filters are mounted at the coldfinger with an attenuation of 14 dB at 10 MHz and 55 dB at 100 MHz.

At last, there are "home-made" Cu-powder filters mounted at the coldfinger. These consist of  $\sim 3$  m wire, wound around a rod of hardened epoxy mixed with copper powder. This rod is integrated in a copper tube, which is filled with more copper powder/epoxy mixture, thus embedding the wire in uniformly distributed copper powder. Via eddy currents, the high-frequency noise is absorbed in the powder. In literature, an attenuation of -90 dBm at 7 GHz can be found [Lukashenko08]. However, the preparation of these filters is complicated and the reported attenuation levels are difficult to obtain. The major difficulty is to achieve a homogeneous distribution of the copper powder within the epoxy.

Figure 5.3 compares the dot current of the same carbon nanotube quantum dot device for different cooling cycles with changes in the electronic setup. The device geometry is similar to the one shown in Fig. 5.2 where the gate voltage is applied via a side gate. The noise level in Fig. 5.3a is  $\sim 20$  pA high and does not allow for the measurement of Coulomb oscillations at a small bias voltage. Measurements with the improved electronic setup containing the filtering components as described above exhibits a noise level of  $\sim 4$  pA and Coulomb oscillations can be observed at  $V_{\text{bias}} = 0.4$  mV. From the Coulomb oscillations, the electron temperature  $T_e$  can be extracted according to Eq. 4.6. The electron temperature of the electronic setup in the measurements shown in Fig. 5.3b is  $\sim 830$  mK.<sup>3</sup> By a further improvement of the Cu-powder filters, the electron temperature could be lowered to  $\sim 600$  mK

<sup>3</sup>at  $V_{\text{bias}} = 0.1$  mV

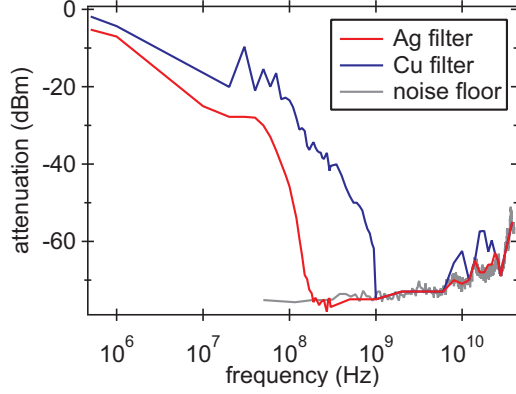


**Figure 5.5:** Attenuation of a copper powder filter (blue) and a silver epoxy filter (red) measured with a Spectrum Analyzer (10 MHz – 50 MHz) and a Network Analyzer (50 MHz – 40 GHz).

(see Fig. 5.4). Although, this is not yet at the desired level, stability diagrams presented in chapter 6 show Coulomb diamonds which close at zero bias voltage and also excited states can be observed as signatures of size quantization.

To further lower the electron temperature, the difficulties in the fabrication of the Cu-powder filters have to be overcome. A different route of making metal powder filters bypasses the issue of an inhomogeneous metal powder by using silver epoxy, which is commercially available with optimized distribution properties. The recent preparation of silver epoxy filters to be implemented into the setup follows a recipe established by C. Scheller at the University of Basel. Silver rods are fabricated from the silver epoxy EPO-TEK<sup>®</sup> E4110 (Epoxy Technology). Subsequently, 3 m of wire are wound around the rod (3 triple-layer coils in series) during which silver epoxy is continuously deposited around the wire. MCX connectors are soldered to each end. Figure 5.5 compares the attenuation of high frequencies of Cu-powder filters with Ag-epoxy filters. The Ag-epoxy filters reach an attenuation of -50 dBm at 110 MHz, while the Cu-powder filters reach the same attenuation at 650 MHz. The Ag-epoxy filters also perform better at very high frequencies above 6 GHz. A second advantage of the silver epoxy is its special application for cryogenic cooling, which is expected to lower the electron temperature significantly ( $T_e = 28 \pm 2.5$  mK have been measured at the University of Basel).



## 6 Interacting parallel quantum dots in a carbon nanotube rope

The ultimate goal in nanotechnology is the fabrication of an electronic device containing a single molecule. The major issue on the way is the assembly of the molecule between two contacts. Sophisticated fabrication techniques [Park99, Ghosh05, Guo06, Guo09] cannot yet prevent an accidental contacting of more than one molecule in parallel [Osorio07, Osorio10]. Molecules are prone to environmental effects and hence also very sensitive to adjacent molecules. Resulting molecular interactions can influence the electronic transport substantially and require a better understanding. However, these interactions also offer interesting effects, as predicted in chapter 4, which may be exploited for the functionality of a device.

This chapter presents low-temperature transport measurements on a carbon nanotube device consisting of several nanotubes bundled together to form a rope. A detailed characterization of the device using Raman spectroscopy in chapter 3, showed that it consists of at least seven nanotubes of different diameters, metallicity and chiralities. Therefore, it represents an ideal system of various molecules to probe molecular interactions. In the beginning, it will be shown that the individual strands of the rope form several parallel quantum dots interacting with each other. Employing the model developed in chapter 4, the molecular interactions between the carbon nanotube strands can be probed by quantum transport spectroscopy exploiting the differential gating effect, which clearly arises in the experiments.



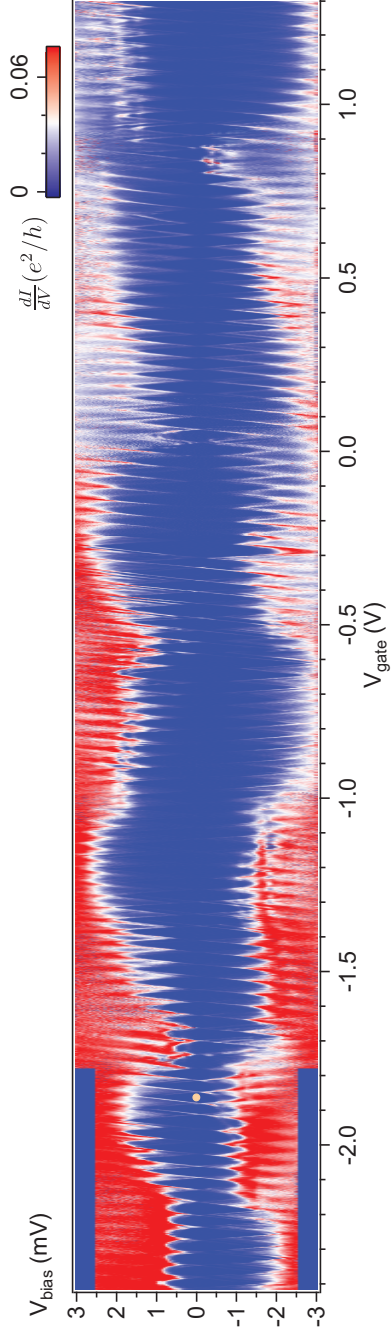


**Figure 6.1:** Differential conductance plot of the device in Fig. 3.6a at low temperatures. The total number of electrons on the dot is arbitrarily set to  $N$  and the white dot marks the  $N$ th diamond. Fluctuations of the diamond sizes appear due to several secondary resonances interfering, which leads to a beating pattern.

## 6.1 Parallel carbon nanotube quantum dots

In order to study molecular interactions between carbon nanotubes, we performed low-temperature transport measurements on the carbon nanotube rope device introduced in chapter 3. Source and drain electrodes (5 nm Ti/60 nm Au) are patterned onto the nanotube rope with a separation of 360 nm and the highly doped Si substrate acts as a back gate. At room temperature, the device shows metallic behavior with a resistance of 290 k $\Omega$  and exhibits no gate dependence in the range of  $V_{\text{gate}} = \pm 2$  V. Low-temperature transport properties were measured in a dilution refrigerator at a base temperature  $T_b \approx 30$  mK as described in chapter 5.

In a differential conductance plot in Fig. 6.1, Coulomb diamonds are observed as typical signatures of Coulomb blockade and show the subsequent addition of electrons to a quantum dot formed in the rope. The Coulomb diamonds close at zero bias voltage and excited states of the quantum dot are observed as resonances starting at the diamond edges, implying size quantization (see close-up in Fig. 6.2). Within a gate voltage region of  $-2.4 \dots +1.3$  V, approximately one hundred charge states are observed showing that the quantum dot is stable over a wide range. The addition energy for the dot varies between 1.4 and 2.4 meV, but no regular pattern of shell-filling, like the fourfold pattern typical for individual single-walled CNTs [Cobden02, Liang02, Sapmaz05], is found.

In the close-up in Fig. 6.2, additional conductance peaks appear within the region of Coulomb blockade (black arrows) and also in the single electron tunneling (SET) regime (blue arrow). These secondary resonances exhibit a weak gate voltage dependence (small slope) and do not appear symmetrically at positive and negative bias voltage. The ones at negative bias voltage are clearly visible within the Coulomb diamonds, whereas those at positive bias voltage are more difficult to distinguish. A high resolution measurement of the same charge states in Fig. 6.3 shows both secondary resonances more distinctly.

The resonances exhibit identical characteristic features to those found in the transport calculations of Fig. 4.9 originating from the interactions between parallel quantum dots. To analyze these characteristics in detail, we concentrate on the resonances appearing at negative bias voltage, which exhibit a small positive slope. First, the conductance of the resonances is enhanced at the meeting points with a main resonance of the Coulomb diamonds. At these meeting points an anticrossing is observed that leads to a gap at the diamond edge. The conductance of the secondary resonance decreases when tuning the gate voltage away from the anticrossing. An identical picture of the conductance is found in the transport calculations at the anticrossing of two resonances due to the hybridization of states on the side dot and the main dot. A second pronounced feature is the jump of the position of the secondary resonances in bias voltage when proceeding from the  $(N - 1)$  to the  $N$  diamond, indicated in Fig. 6.3 by dashed lines. It was found in section 4.3 that such

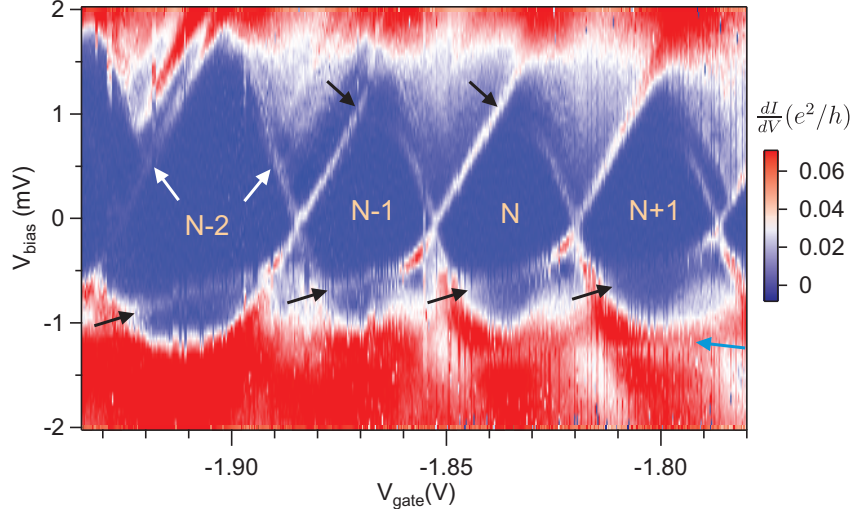


**Figure 6.2:** Close-up of several Coulomb diamonds in Fig. 6.1. Excited states are indicated by white arrows. Black and blue arrows indicate the onset of secondary resonances passing through the Coulomb blocked regions and in the SET regime.

an abrupt energy shift can be modeled by a capacitive coupling of two quantum dots.

Having devised the main features of the secondary resonance at negative bias voltage, the differences to the one at positive bias voltage become apparent. Their positions are not symmetric around zero bias voltage, but the lower one is positioned at  $V_{\text{bias}} = -0.4 \text{ meV}$  while the other appears at  $V_{\text{bias}} = +0.8 \text{ meV}$ . The latter one exhibits a negative slope and the conductance at the meeting points with the main resonance is much less enhanced than before, while it almost disappears moving away from the anticrossing. However, the gap of the anticrossing leading to the missing diamond edge at  $V_{\text{bias}} > +0.8 \text{ mV}$  is clearly observable, evidencing the existence of the secondary resonance. Furthermore, the magnitude of the voltage jump of the secondary resonance between subsequent diamonds is larger than the one before.

Inelastic cotunneling [Averin90, De Franceschi01], which is a coherent tunneling process, cannot explain the combination of these features considering excitations of only a single quantum dot. Coherent tunneling processes can appear in the stability diagram, when the tunnel coupling becomes large enough, so that processes involving more than one tunneling event come into play. Cotunneling involves the tunneling of one electron onto the dot while simultaneously another electron tunnels off the dot. In contrast to elastic cotunneling, the energy state of the dot is changed by inelastic cotunneling. Then, a resonance line is visible in the Coulomb-blockade region at

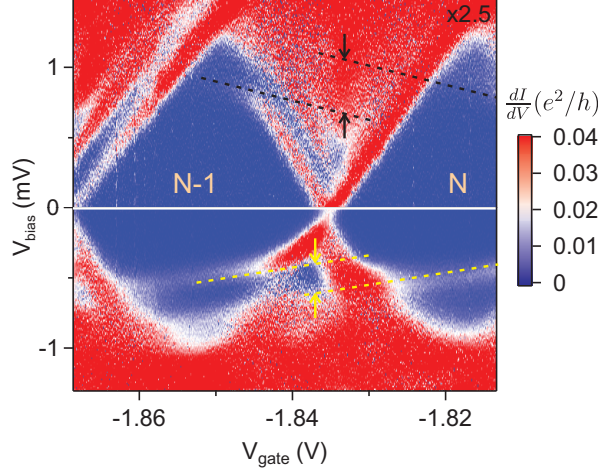


**Figure 6.3:** Differential conductance plot measured with high resolution. Dashed lines indicate the slopes of the secondary resonances and their voltage offset between adjacent Coulomb diamonds  $((N - 1) \rightarrow N)$  is indicated by arrows. Note the multiplied conductance at positive  $V_{\text{bias}}$ .

positive and negative bias voltages, which are equal to the excitation energy. A possible gate dependence of inelastic cotunneling lines has been reported in carbon nanotube quantum dots [Holm08]. However, these always appear symmetrically at positive and negative bias voltages and can therefore not explain the features observed in the device.

Instead, the data indicate that several coupled quantum dots are formed in the rope and contacted in parallel, giving rise to the different resonances in the stability diagram, according to the model developed in section 4.3. The pattern of Coulomb diamonds is ascribed to a main dot formed on one strand and the secondary resonances at negative and positive bias voltage originate from two different side dots formed on different strands of the rope. In contrast to serial double quantum dots [Mason04, Sapmaz06b, Gräber06], transport through the parallel configuration is possible even if one of the dots is in Coulomb blockade resulting in closing diamonds at  $V_{\text{bias}} = 0$  mV as it is observed for the main dot in the nanotube rope device. The distinct coupling between strands of the rope gives rise to the distinct appearance of the secondary resonances in the stability diagram.

Comparing the calculation in Fig. 4.9 with the measurement in Fig. 6.3, the major difference is that a generally higher differential conductance is observed in the experiment. This may have three reasons. First, the resonances in the calculations are only thermally broadened while tunnel broadening is neglected. Second, the particular calculation shown in the Figure includes only one orbital for each dot, while the experiment shows excited states of the main dot which are not in all cases clearly observable, but are broadened. Finally, the calculations account for only one side dot, hence one secondary resonance, whereas the measurement clearly

distinguishes more than one. In Fig. 6.2, a secondary resonance with negative slope, which was not discussed in detail up to now, is marked at the tips of the diamonds (blue arrow). As we will show in the next section, this resonance originates from yet another side dot.

## 6.2 Quantum transport spectroscopy of carbon nanotube interactions

In the previous section, we found secondary resonances originating from at least two side dots contacted in parallel to the main dot on the nanotube rope. Based on the measurement of  $\sim 100$  charge states of the main dot in Fig. 6.1 we will in the following evaluate how many side dots can be found on the rope and how these interact with the main dot. The diamond pattern of the main dot shows an overall fluctuation or beating. These fluctuations appear due to the secondary resonances passing the Coulomb blocked regions and thus blurring the diamond tips. Nevertheless, the diamonds are regular in the sense that the coupling parameters to the leads and the gate are constant over the whole range. According to Eq. 4.8, the parameters are  $\alpha_{\text{gt}} = 0.05$ ,  $\alpha_{\text{sc}} = 0.36$  and  $\alpha_{\text{dr}} = 0.59$ .

For a characterization of the side dots, one would like to determine their coupling parameters from the size of the Coulomb diamonds. However, no complete side dot diamond can be found in the measurements, but always only one slope of it. This is due to an asymmetric coupling of the side dot to the contacts. In the case of a very weak gate coupling, a strong source/drain coupling involves a considerable tilt of the Coulomb diamonds, which leads to one diamond slope being very steep. This slope can hardly be observed within the main diamonds. For  $\alpha_{\text{sc}} \approx 1/2$ , the dot is equally coupled to both contacts ( $C_{\text{sc}} \approx C_{\text{dr}}$ ) and the diamond appears symmetric, as sketched in Fig. 6.4a. Assuming the same gate coupling, but a strong source coupling  $\alpha_{\text{sc}} \gg 1/2$ , the positive diamond slope is much larger than the negative according to Eq. 4.8, and the diamond appears tilted (dotted diamond in Fig. 6.4a). For a strong drain coupling ( $\alpha_{\text{sc}} \ll 1/2$ ), the positive slope is much smaller than the negative and the diamond tilts into the other direction (dashed diamond).

In order to obtain an estimate for the couplings of the side dots, we construct the size of the side dot diamonds from the secondary resonances as sketched in Fig. 6.4b. For this we make two assumptions:

- (i) The addition energy is assumed to be equal to the main dot (1.8 meV). This is a well-justified assumption, since the quantum dots are very similar: The contacts are at the same separations for all CNTs, which defines the charging energy.
- (ii) The missing slope of the side dot diamonds is assumed to be the same as for the main dot, because in this case it is hidden in the main dot diamond pattern. If

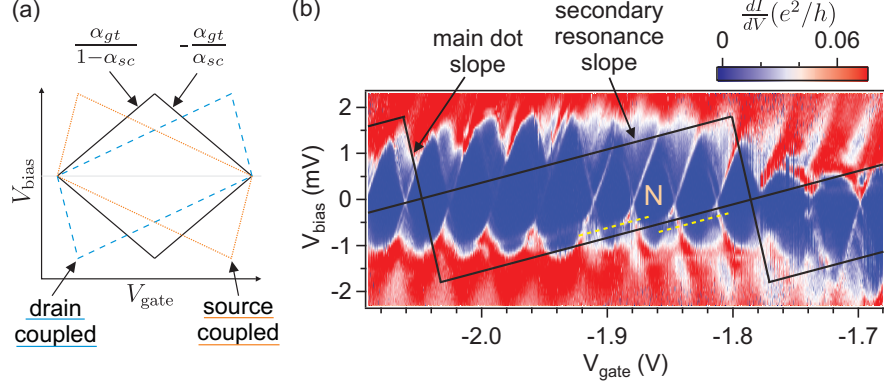


**Figure 6.4:** (a) Sketch of the effect of different source and drain couplings on the shape of the Coulomb diamonds. (b) Constructed Coulomb diamonds for one of the side dots matching the position of the secondary resonance in the  $N$ th diamond. Dashed lines indicate the positions in the two adjacent Coulomb diamonds.

it was smaller, it would be observable as a resonance in the diamond pattern. An evaluation with steeper slopes up to completely vertical did not change the results significantly.

The exact position in  $V_{\text{gate}}$  of the side dot diamonds remains undetermined, because the voltage offset due to the capacitive inter-dot coupling masks this information. In Fig. 6.4b, a  $V_{\text{gate}}$  position is chosen matching the secondary resonance at negative bias voltage in the  $N$ th diamond. In principle, the corresponding diamond edge at positive bias voltage, as drawn in the figure, should also be observable as secondary resonance. However, we never observe this in our measurements. A possible reason for this is an interaction with the other side dots. This can shift the secondary resonances additionally and lead to a complex stability diagram difficult to predict with our model, because it takes into account only two parallel dots.

A different approach to construct the side dot diamonds of a parallel quantum dot setup has been reported by Eliassen *et al.* [Eliassen10]. The authors claim that a side dot is formed by a chain of fullerenes inside a carbon nanotube, which forms the main dot. They draw the  $V_{\text{bias}}$  position of the anticrossings in the various main dot diamonds and construct the side dot diamond edges from these positions. However, this approach neglects the influence of the capacitive inter-dot coupling and consequently results in a distorted estimate for the slope of the diamonds, which should in fact be the slope of the secondary resonance itself.

Having now established a route to estimate the side dot Coulomb diamonds, we have in total four parameters by which the side dots can be distinguished:

- Source or drain coupling ( $\alpha_{\text{sc}}^s, \alpha_{\text{dr}}^s$ ): By observing a negative or a positive slope of the secondary resonance, its coupling to one of the leads can be evaluated.
- Gate coupling ( $\alpha_{\text{gt}}$ ): The magnitude of the slope leads to the coupling strength to the back gate via the construction of the Coulomb diamonds.
- Hybridization ( $t$ ): The magnitude of the gap between the bonding and the anti-bonding state at the anticrossings is given by the strength of the tunnel coupling between the side dot and the main dot.
- Inter-dot charging energy ( $U^{ms}$ ): The capacitive inter-dot coupling between the side dot and the main dot determines the shift of the secondary resonances between adjacent Coulomb diamonds.

These are the parameters, by which the interactions of the quantum dots between each other and with the electronic environment are described. Figures 6.5a-d show close-ups for all secondary resonances observed within the gate voltage range of Fig. 6.1. In the following, the coupling parameters of the side dots are evaluated from these and summarized in Tab. 6.1.

In Fig. 6.5a, a secondary resonance is observable, which crosses the main dot diamonds unperturbed as a straight line with a small positive slope. Therefore, the side dot 1 causing these secondary resonances is strongly coupled to the drain. The back gate coupling of this side dot is extremely small and a comparison of the diamond patterns sketched in Fig. 6.5e illustrates that, while approximately 50 electrons are added to the main dot, only one electron can be charged onto side dot 1 with the same gate voltage. The absence of a voltage offset means that this side dot is not capacitively coupled to the main dot. Although a slightly enhanced conductance can be observed at the meeting points of the secondary resonance with the diamond edge, no gap or anticrossing can be identified, which leads us to the conclusion, that these two dots are also not tunnel coupled. Therefore, the main dot and side dot 1 exhibit no interaction, which could be probed by quantum transport.

The secondary resonance of side dot 2 in Fig. 6.5b again has a positive slope (drain coupling), but it does not pass straight through all the diamonds. It exhibits a voltage offset between subsequent diamonds, indicating a capacitive coupling of the side dot 2 and the main dot, which is found to be  $U_2^{ms} = 0.225 \text{ meV}$ . However, no conductance enhancement or anticrossing can be observed and therefore, the two dots are not tunnel coupled. In addition to the side dot 2, more secondary resonances are visible at negative bias voltages. These are found to have the same properties as the secondary resonances in Fig. 6.5c and are hence ascribed to side dot 3.

The secondary resonances in Fig. 6.5c exhibit the same positive slope as side dot 1. However, a small voltage offset ( $U_3^{ms} \approx 0.075 \text{ meV}$ ) indicates a capacitive coupling, which leads one to the conclusion that it originates from a different side

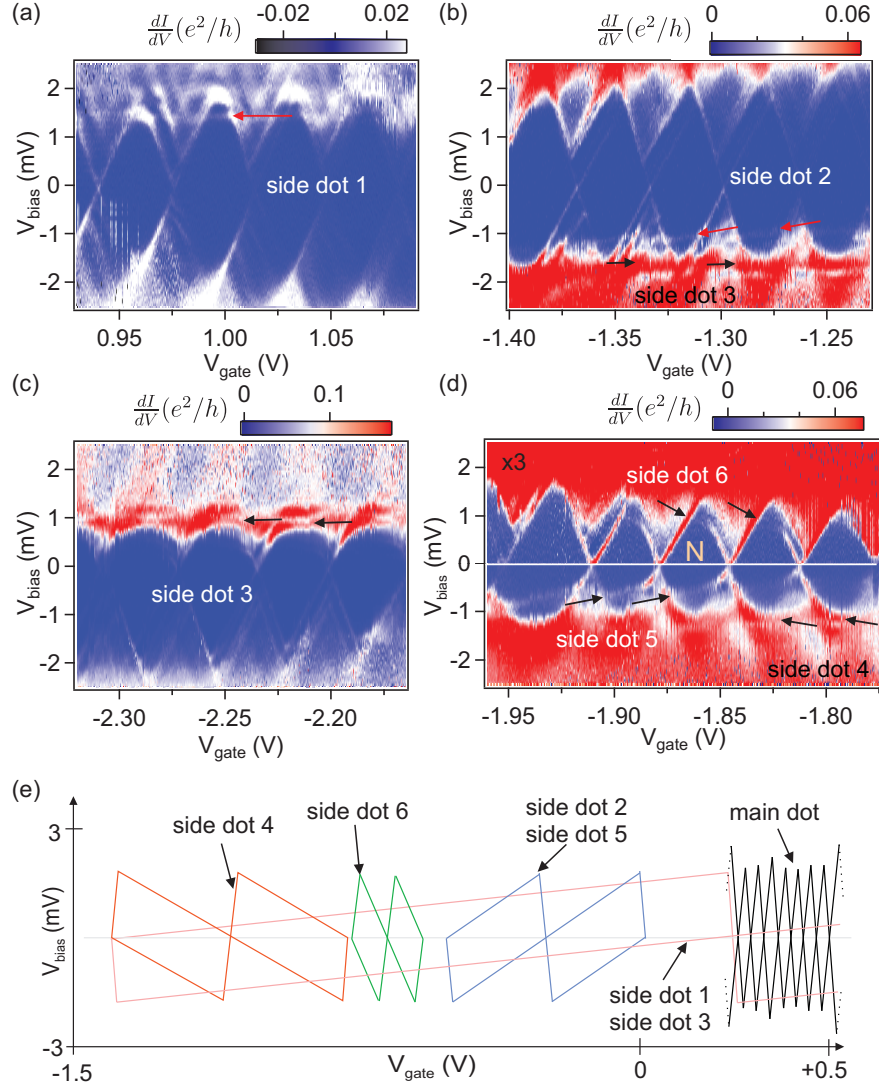


**Figure 6.5:** (a)–(d) Zoom into regions of Fig. 6.1 showing secondary resonances. Arrows indicate their position and energy offset. They are ascribed to side dots 1 to 6, whose coupling parameters and interaction properties are given in Tab. 6.1. Note the multiplied conductance at positive  $V_{\text{bias}}$  in panel (d). (e) Sketch of all side dot diamonds according to the example in Fig. 6.4. The size and tilt of the diamonds is drawn to scale.



dot 3. Additionally, there is a clearly enhanced conductance at the meeting points of the resonance lines. From this enhancement, coming along with curved resonances, we conclude that the resonances exhibit an anticrossing. However, the measurement resolution does not allow for an estimate of the magnitude of the tunnel coupling  $t_3$ . The differences in the interaction parameters of side dot 1 and side dot 3 are not very pronounced and it cannot be ruled out that the resonances originate from the same side dot. The capacitive coupling between two dots should in general not depend on the charge state of main dot, but the tunnel coupling to a side dot state may change for different states of the main dot.

The anticrossings in Fig. 6.5d are more clearly visible, which is the region shown previously in Fig. 6.2 and Fig. 6.3, where several secondary resonances are present within a small region of gate voltage. Three different resonances can be found, all of them exhibiting a strong interaction with the main dot. The one at the tips of the main dot diamonds at negative bias voltages originates from a source coupled side dot 4 (negative slope). Like for side dot 3, a hybridization with the main dot can be argued from the obvious conductance enhancement, but again  $t_4$  cannot be extracted from the anticrossings due to the limited resolution. The secondary resonances at negative bias voltage with positive slope (drain coupled) exhibit the same slope as side dot 2 and a comparable voltage offset ( $U_5^{ms} = 0.2 \text{ meV}$ ). However, the resonances in this gate voltage region do show a hybridization  $t_5 = 0.075 \text{ meV}$  with a clear gap at the diamond edges. Hence, we ascribe the resonances to a different side dot 5. Again, it cannot be ruled out completely that the resonances originate from the same side dot, because the hybridization of side dot states may change for different states of the main dot. For the last side dot 6, a rather strong gate coupling in comparison to the other side dots is found and a comparatively steep negative slope indicates only a slightly stronger coupling to the source electrode. Also the largest hybridization amplitude ( $t_6 = 0.1 \text{ meV}$ ) and inter-dot charging energy ( $U_6^{ms} = 0.4 \text{ meV}$ ) are extracted.

In total, we find a maximum number of six side dots in a region of approximately 100 charge states of the main dot, which can be distinguished by their interactions. In our measurements, the main dot exhibits a gate coupling  $\alpha_{\text{gt}}^m = 0.05$  and a source coupling  $\alpha_{\text{sc}}^m = 0.36$ . This gate coupling is roughly one order of magnitude higher than the one that the weakly gate coupled side dots exhibit ( $\alpha_{\text{gt}}^s$  between 0.001 and 0.007). The main dot does not exhibit a peculiar coupling to one of the contacts, while the side dots are either source or drain coupled, which is sketched in Fig. 6.5e. These different contact couplings can be induced by a structural non-uniformity of the nanotube rope. The nanotube which is lying on top of the rope at the one contact and thus is favourably connected, may change its vertical position within the rope and is only weakly connected at the second contact. This change of vertical positions of the nanotube strands within the rope was confirmed by tip-enhanced Raman spectroscopy in chapter 3.

### 6.3. SHIFTING THE POTENTIAL OF THE MAIN DOT STATES

dot	$\alpha_{gt}$	$\alpha_{sc}$	$\alpha_{dr}$	$t$ (meV)	$U^{ms}$ (meV)
main dot	0.05	0.36	0.59	–	–
side dot 1	0.0011	0.0017	0.9972	0	0
side dot 2	0.0069	0.0739	0.9192	0	0.225
side dot 3	0.0011	0.0017	0.9972	$\neq 0$	0.075
side dot 4	0.0057	0.9394	0.0549	$\neq 0$	0.150
side dot 5	0.0069	0.0739	0.9192	0.075	0.200
side dot 6	0.0189	0.7648	0.2163	0.100	0.400

**Table 6.1:** Coupling parameters and interaction properties of the quantum dots observed as secondary resonances in Fig. 6.1 and Fig. 6.5a-d.

The distinct interaction properties of the side dots imply information about the nanotube strands, where the dots are formed. The closer the strand is to the one of the main dot, the larger its interaction is expected to be. A tunnel coupling is only expected when an overlap of the quantum dot wave functions is possible, i. e. the strands have to be adjacent. A capacitive coupling, however, is also conceivable if the strands are further apart from each other. In that case, its magnitude is expected to be smaller, since the potential may be screened by another strand lying in between. In principle, an interaction between side dots is expected additionally to all the above mentioned couplings. However, the measurements do not allow for an evaluation of these, although meeting points of different secondary resonances are expected, e. g. in Fig. 6.5d.

The coupling parameters of side dot 6 are peculiar. The back gate coupling is more than twice as large as for the rest of the side dots and the coupling to the contacts is not particularly asymmetric. Regarding this aspect, the side dot behaves similar to the main dot. Also concerning the dot interaction properties, side dot 6 exhibits salient parameters. It shows by far the largest interaction values, suggesting it is formed in a strand very close to the main dot strand, which also explains the even coupling to both electrodes. In the following, it will be shown that this side dot is indeed behaving similar to the main dot.

### 6.3 Shifting the potential of the main dot states

Generally, the capacitive coupling between two parallel quantum dots does not only affect the Coulomb diamonds of one dot. In the previous measurements, we found it leading to a voltage offset in the secondary resonances, but it can also influence

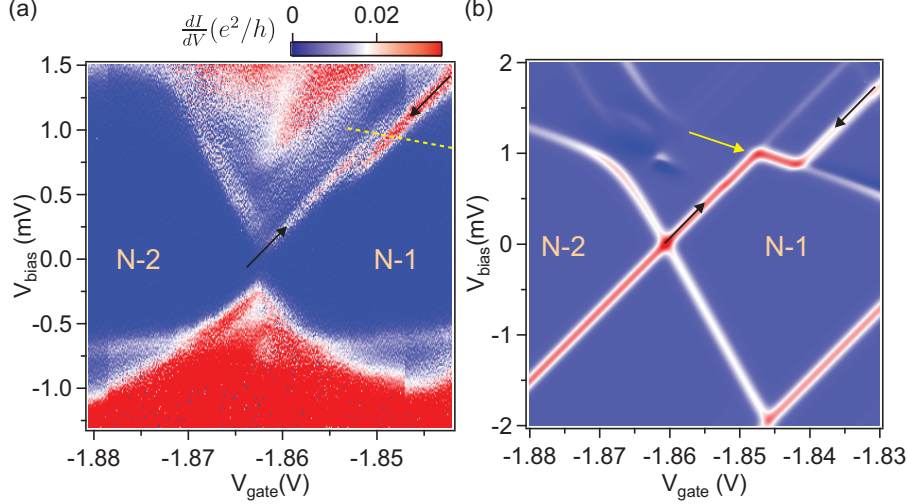


**Figure 6.6:** (a) Differential conductance plot with shifted main dot diamond (arrows). As before, a secondary resonance of side dot 5 is observed at negative bias voltages. A yellow line indicates the position of the secondary resonance of side dot 6. (b) Transport calculations reproducing the shifted diamond edge above the secondary resonance. See text for details on the tunneling rates.

the main resonances, i. e. the main dot diamonds. An additional electron on one of the side dots changes the potential for the electrons on the main dot and a shifted main dot diamond edge should be observable at energies higher than the secondary resonance, i. e. in the SET regime of the side dot. Figure 6.6a shows another measurement of the  $(N-1)$ th main dot diamond. As before in Fig. 6.3, a secondary resonance of side dot 5 is observed at negative bias voltages. The position of the secondary resonance of side dot 6 is marked, although the conductance is too low to be clearly observed in this specific measurement. Remarkably, a shift of the diamond edge can be observed close to the meeting point of the secondary resonance with the main resonance. The effect is clearly distinguishable from jumps due to charge rearrangements, because the rest of the data appears continuous.

Figure 6.6b shows a calculated stability diagram according to our quantum dot model. Similar to the measurement, the diamond edge is shifted. The shift occurs due to the additional potential caused by an electron tunneling onto the side dot, hence the main resonance is shifted where the secondary resonance crosses (yellow arrow). In the calculations, the shifted main dot diamond edge becomes visible only when the tunneling rates for the side dot are assumed to be  $\Gamma_{\text{sc}}^s > \Gamma_{\text{dr}}^s$ , while  $\Gamma_{\text{sc}}^m = \Gamma_{\text{dr}}^m > \Gamma_{\text{sc}}^s$  is assumed for the main dot. This leads to a situation, where

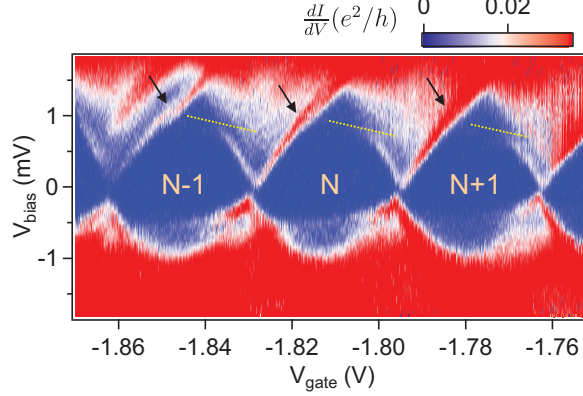


**Figure 6.7:** Differential conductance plot with a voltage offset for the main resonance. Yellow dashed lines indicate the positions of the secondary resonances of side dot 6 with a voltage offset of  $U_6^{ms} = 0.4$  meV. Arrows indicate the shifted diamond edges.

the energy level of the side dot is mainly occupied, and transport predominantly takes place via the energy level on the main dot. Then the original diamond edge (side dot not occupied) is suppressed, whereas the shifted diamond edge (side dot occupied) appears enhanced. This configuration of tunneling rates also suppresses the conductance through the side dot, hence the secondary resonance is less visible. This is consistent with the experimentally found weak conductance of the secondary resonance of side dot 6.

We find the magnitude of the shift of the diamond edge to be  $\Delta V \approx 0.2$  meV, whereas  $U_6^{ms} = 0.4$  meV was obtained by the voltage offset of the secondary resonance. The discrepancy can be explained by considering the different bias couplings of side dot 6 and the main dot. In fact, the voltage offsets due to a capacitive inter-dot coupling and also the magnitude of the anticrossing gap depend on the bias coupling. A large  $\alpha_{sc}$  will lead to a large  $V_{bias}$  offset, because  $\Delta V = U^{ms}/(1 - \alpha_{sc})$ , where  $\alpha_{sc}$  is the source coupling of the dot corresponding to the shifting resonance. The estimates in Tab. 6.1 for  $t$  and  $U^{ms}$  are thus upper bounds, but within the right order of magnitude. Considering the source couplings of the main dot and the side dot 6 from Tab. 6.1, the observed shift in the diamond edge fits with an expected shift of

$$\Delta V^m = \Delta V^{s6} \frac{1 - \alpha_{sc}^{s6}}{1 - \alpha_{sc}^m} = 0.15 \text{ meV}. \quad (6.1)$$

In principle, the source coupling of the main dot is more reliable than the ones of the side dots, because no assumptions had to be made for obtaining them. Evaluating the capacitive inter-dot coupling from the shifted diamond edge,  $U_m^{ms} = 0.13$  meV is obtained. Considering the smaller voltage offsets of the other side dots, a shifted main dot diamond edge due to the charging of these is not resolved in our measurements.

Figure 6.7 plots three subsequent Coulomb diamonds where the impact of the capacitive inter-dot coupling is observed for both the side dot and the main dot. Arrows mark the positions where shifted diamond edges are expected. Due to the low resolution of the measurement, the shift is not clearly resolvable, but the diamond edges become very broad, indicating two resonances smeared out to one broad line. The voltage offset of the secondary resonances between subsequent diamonds is identical to the one observed earlier. The question arises, why the shifted main dot diamond is not observable in every measurement for the same secondary resonance passing. As stated above, a certain relation of tunneling rates is necessary for the shift to be observed. The tunneling rates may change depending on the history of the device. For example in between the measurement in Fig. 6.3 and the one in Fig. 6.6a is a time span of three weeks, in which wide gate voltage scans were performed, the device was grounded several times and it was warmed up to 4 K.

Although several side dots are interacting with the main dot, only side dot 6 is coupled strongly enough to shift the main dot resonances in energy. Nevertheless, a regular diamond pattern can be found for the main dot over many charge states as shown in Fig. 6.1. This one main dot amongst all the other parallel contacted ones is dominating the tunneling effects, but which conditions lead to one dot being so distinct from the others remains speculative. One explanation may be significantly higher tunneling rates in comparison to the other dots due to a lower contact resistance for the uppermost carbon nanotube. However, this picture does not completely fit with the main dot's coupling to the back gate, which would be expected to be smaller due to screening of other nanotubes in between. Without the thorough additional characterization of the device properties by Raman spectroscopy presented in chapter 3, the quantum transport data could easily mislead one to the assumption of dealing with a multiwalled nanotube, where the outer shell forms the main dot and the inner shells contribute to the transport as the side dots.

## 6.4 Conclusions

This chapter presented quantum transport through parallel quantum dots, formed in different carbon nanotube strands within a rope, demonstrating a tunable quantum device. Agreement between transport calculations employing the model of chapter 4 and the measurements confirms interacting parallel quantum dots as origin for the observed anomalous features. Using the differential gating effect to tune the quantum dot system to different configurations, we determined the magnitude of the electronic hybridization between the states of the coupled quantum dots and their capacitive inter-dot coupling. A thorough characterization of six observed side dots reveals that the nanotube strands can interact to a very different extent with each other.

Amongst the coupled quantum dots, we also find only capacitively interacting or completely uncoupled quantum dots within the one device. The simultaneous observation of tunnel-coupled and non tunnel-coupled parallel QDs extends previous experiments, where either no hybridization was observed for two molecular quantum dots in parallel [Osorio07], or an anticrossing gap was found at each meeting point of resonances for a  $C_{60}$  fullerene chain inside a nanotube [Eliassen10]. In the latter case, also a capacitive coupling was observed and the magnitude of the anticrossing gap and of the inter-dot charging energy compares well with the values found for side dot 5 and side dot 6 in our case. Our results show that intertube coupling effects in low-temperature transport may be larger than previously assumed [Bockrath97, Grove-Rasmussen08] and should not be neglected when interpreting quantum transport measurements involving carbon nanotubes.

All of the above mentioned publications on molecular quantum dots lack an additional characterization of the devices. In contrast, the interpretation of the results in this chapter is strongly supported by and consistent with a supplementary characterization of the same device by an independent spectroscopic technique shown in chapter 3. There, Raman spectroscopy proved that the device consists of a rope with several carbon nanotube strands which are the only possible origin of the parallel quantum dots. Additionally, first signatures of interactions between the strands were found in a shift of optical transition energies. By exploiting the spatial resolution of the tip-enhanced Raman technique, the changing interface properties for the individual strands have been predicted by monitoring a change of vertical position for particular nanotubes along the rope axis.

The conclusions on molecular interactions drawn here from a system of coupled carbon nanotubes can be transferred to other molecular systems and hence support the interpretation of transport behaviour of single-molecule junctions.



## 7 Hybridization between quantum dot states

The model of interacting parallel quantum dots offers the possibility to investigate the tunnel coupling between states on two different dots. The tunnel coupling, which is an electronic hybridization of quantum dot states, is expected to contain additional information on the involved orbitals of the dots. In principle, the overlapping wave functions of the quantum dot states comprise the molecular orbitals of the carbon nanotubes, where the dots are formed. Hence, quantum transport spectroscopy of hybridized states is especially interesting for molecular quantum dots and may reveal details about the nature of the transport properties of the molecule.

This chapter is focused on the electronic hybridization observed in the same carbon nanotube rope device as in the previous chapter. Several interacting quantum dots have been detected, whereas only few of them exhibit a clear hybridization. These are the strongest coupled quantum dots, which we now investigate in more detail. In the first part of the chapter, the sign, i. e., the phase of the hybridization amplitude is discussed, while the second part concentrates on spin-effects in the hybridizing states.

### 7.1 The hybridization phase

After identifying several coupled parallel quantum dots on the carbon nanotube rope device in the previous chapter, we now want to focus on the two side dots which exhibit a pronounced hybridization with main dot states, i. e. side dot 5 and side dot 6. In the measurement of Fig. 6.3 and also in the transport calculations of Fig. 4.9, the bonding and anti-bonding states at the anticrossings clearly contribute very differently to the conductance. This relates to the sign of  $t$ , as will be shown in the following. We focus on the sub-block of the full Hamiltonian of Eq. 4.20 describing the hybridization of two states  $|m\rangle, |s\rangle$  on the main dot and the side dot, respectively:

$$H = \begin{pmatrix} \epsilon(V_{\text{bias}}, V_{\text{gate}}) & t \\ t & -\epsilon(V_{\text{bias}}, V_{\text{gate}}) \end{pmatrix}, \quad (7.1)$$



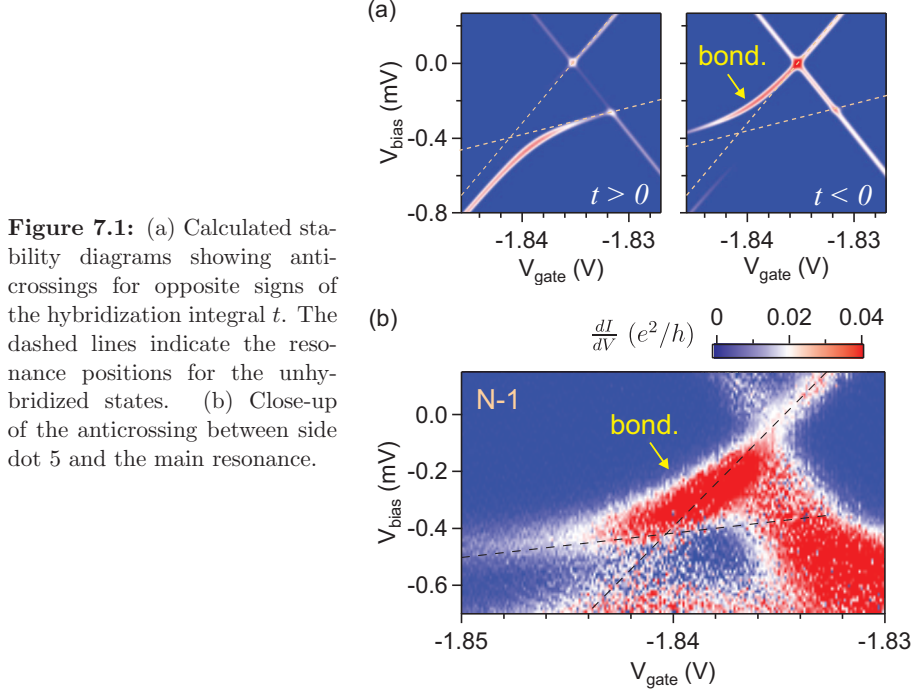


**Figure 7.1:** (a) Calculated stability diagrams showing anticrossings for opposite signs of the hybridization integral  $t$ . The dashed lines indicate the resonance positions for the unhybridized states. (b) Close-up of the anticrossing between side dot 5 and the main resonance.

where the energy of the states  $\epsilon$  is taken relative to the resonance energy. We diagonalize the Hamiltonian for each set of applied voltages ( $V_{\text{bias}}, V_{\text{gate}}$ ) in the stability diagram and obtain the eigenenergies  $\pm\sqrt{\epsilon^2 + t^2}$  for the hybridized states. Here we call the hybridized state with the lower energy bonding  $|-\rangle$  and the one with higher energy anti-bonding  $|+\rangle$ . The hybridized eigenstates of the coupled QDs

$$\begin{aligned} |+\rangle &= \cos\theta|m\rangle + \sin\theta|s\rangle \\ |-\rangle &= -\sin\theta|m\rangle + \cos\theta|s\rangle, \end{aligned} \quad (7.2)$$

depend on the applied voltages through  $\theta$ , where  $\tan\theta = (\sqrt{\epsilon^2 + t^2} - \epsilon)/t$ . At resonance we have by definition  $\epsilon = 0$  and the magnitude of the gap at the anticrossing is  $2|t|$ .

Recalling the notation from section 4.3.1, the tunneling rates  $\Gamma_{\pm \leftarrow i}$  (abbreviated as  $\Gamma_{\pm}$ ) from an initial state  $|i\rangle$  in the leads (we assume now in the left lead) into the bonding  $|-\rangle$  or the anti-bonding  $|+\rangle$  state are proportional to the corresponding tunnel matrix elements  $T_{\pm}$  (see Eq. 4.13):

$$\Gamma_+ \propto |\langle + | H_{TL} | i \rangle|^2 = |T_+|^2 = T_m^2 \cos^2\theta + T_s^2 \sin^2\theta + T_m T_s \cos\theta \sin\theta \quad (7.3)$$

$$\Gamma_- \propto |\langle - | H_{TL} | i \rangle|^2 = |T_-|^2 = T_m^2 \sin^2\theta + T_s^2 \cos^2\theta - T_m T_s \cos\theta \sin\theta. \quad (7.4)$$

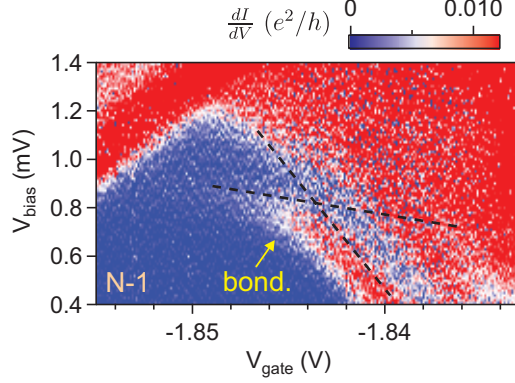


**Figure 7.2:** Close-up of the anticrossing between side dot 6 and the main resonance. The dashed lines indicate the resonance positions for the unhybridized states.

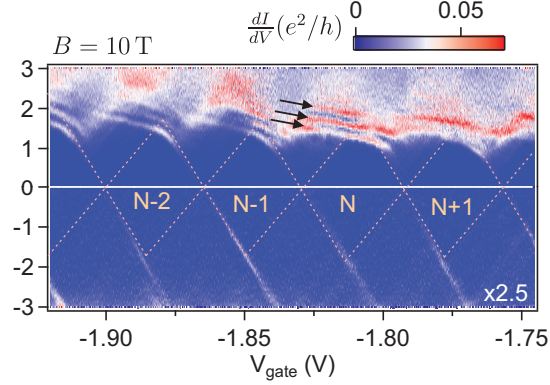
Here  $T_m$  and  $T_s$  are the matrix elements for tunneling into  $|m\rangle$  or  $|s\rangle$ , respectively, whose sign we take to be identical since the strands form a single junction.  $H_{TL}$  is the tunnel Hamiltonian as defined in Eq. 4.11.

The  $\Gamma_{\pm}$  contain an interference term with opposite sign. This term causes either a suppression or an enhancement of the rate to the hybridized state depending on the sign of the hybridization integral  $t$  through  $\theta$ . Hence, the sign or the phase of the hybridization  $t$  determines which tunneling rate (bonding or anti-bonding) will be suppressed or enhanced. The interference effect at the anticrossing is due to an interference of two bound states, both connected to the leads, and is hence distinct from the Fano effect, where one bound state interferes with an unscattered wave.

The left (right) panel in Fig. 7.1a shows a calculated anticrossing of two hybridizing states with a positive (negative) hybridization integral  $t$ , where a clearly enhanced anti-bonding (bonding) state is visible. In both cases, the conductance in the enhanced state exhibits an additional pronounced gate voltage dependence, which is characteristic for the hybridization itself, and does not depend on the sign of  $t$ . In the experiment, we find an enhanced current of the bonding state at the anticrossing of side dot 5 in Fig. 7.1b and also for side dot 6 in Fig. 7.2. For the side dots 3 and 4, where we concluded a finite hybridization amplitude due to the enhanced conductance, we also observe an enhancement of the bonding state in all cases, although the gap between the hybridized states is not clearly resolvable.

Therefore, we conclude that the nanotube strands hybridize with a negative hybridization integral. A negative  $t$  denotes a positive overlap of orbital wavefunctions, which means the concurrence of equal signs of the wavefunctions, as known for the hopping integral in the tight-binding approximation of the formation of molecular bonds. The envelope wavefunction of a carbon nanotube in the ground state has  $s$ -like symmetry and the hybridization integral of two nanotubes brought into each other's vicinity, would thus be expected to be negative. Considering more complex

**Figure 7.3:** Differential conductance plot of identical charge states as in Fig. 6.2 at  $B = 10$  T. Dashed lines indicate the faint main dot diamonds. Arrows indicate parallel secondary resonances.



molecules as interacting quantum dots, the sign of the hybridization may depend on the nature of the molecular orbitals. Hence, the investigation of the conductance in the hybridized states may lead to the observation of new properties.

## 7.2 Spin-dependent hybridization

In order to investigate a possible influence of the spin degrees of freedom on the hybridization within the rope, the transport spectrum was measured in a magnetic field. Figure 7.3 presents the same charge states of the main dot at  $B = 10$  T, which were shown in Fig. 6.2 for zero magnetic field, and reveals substantial differences. Compared to the measurements at  $B = 0$  T, the transport through the main dot is strongly suppressed at  $B = 10$  T, secondary resonances of side dot 5 are not visible at negative  $V_{\text{bias}}$  and the secondary resonances at positive bias voltage (side dot 6) appear as the most prominent feature. The alteration of the dominant strand for the transport is reversible by sweeping the magnetic field. However, the mechanism leading to the competing transport channels is unclear.

The anticrossings of the resonances again show an enhancement of the bonding state. The energy offset, hybridization integral, and gate coupling are the same as in zero field, evidencing that these resonances indeed originate from the same CNT strand as the ones at  $B = 0$  T. The stability diagram shows additional resonances involving excited states of the side dot (marked by arrows), which exhibit the same weak gate voltage dependence and anticrossings as the initial secondary resonances. In the following, we will discuss the origin of the different states of the side dot.

Figure 7.4a shows a zoom into the secondary resonances of Fig. 7.3 and reveals a new appearance of this side dot. Amidst the anticrossings of the lowest secondary resonances with the diamond edges (marked (2) and (3)), a clear *crossing* (marked

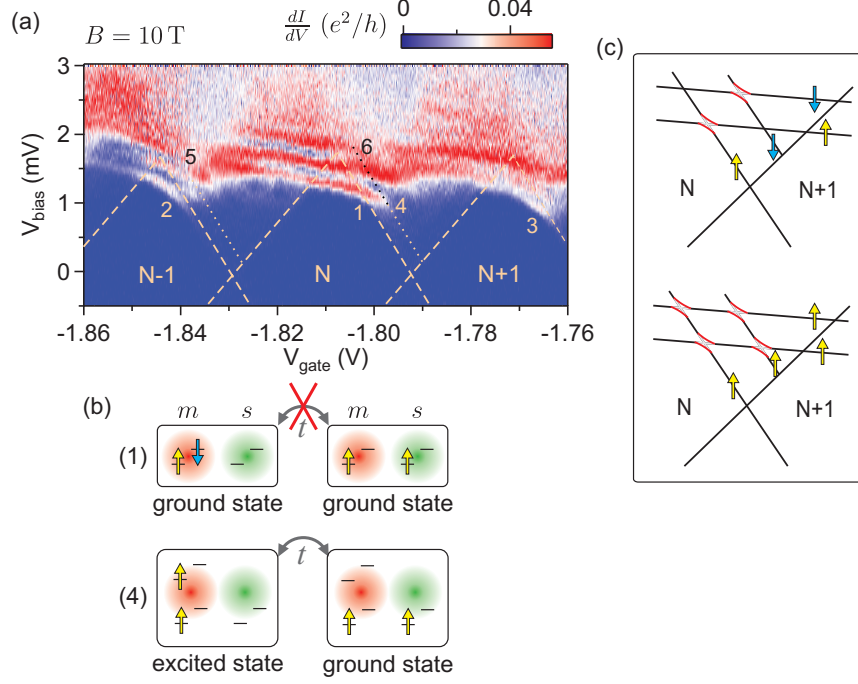


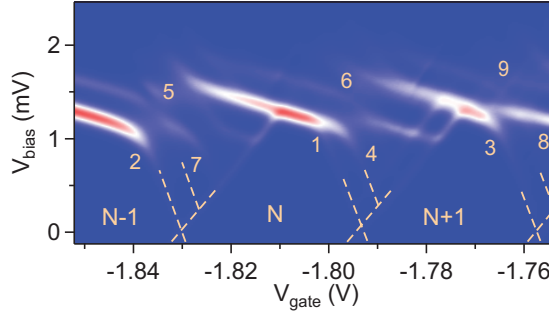
**Figure 7.4:** (a) Close-up of the anticrossings/crossings of Fig. 7.3 at  $B = 10$  T. (b) Schematic of the spin configurations of the non-hybridizing ground states at position (1) and hybridizing configurations with an excited state involved at position (4). Arrows indicate spin-split states, energetically split due to a magnetic field. (c) Schematic stability diagram for different state configurations of the dots.

(1)) appears, when the chemical potential  $\mu^s$  for adding an electron to the ground state of the side dot is at resonance with the chemical potential of the main dot  $\mu^m$  for the ground state transition from  $N$  to  $N+1$  electrons. This crossing reveals that the resonant states of the coupled QD system containing in total  $N+1$  electrons have different quantum numbers, preventing the states from hybridizing. We propose that the hybridization is prevented due to a different spin of the two states.

Figure 7.4b sketches the spin configurations of the coupled quantum dot system that are involved in the crossing at position (1). Due to the magnetic field, the spin states are split by the Zeeman energy. With the assumption that  $N = 1$ <sup>1</sup>, the diamond edge of the  $N$ th diamond indicates tunneling of a spin-down electron across the main dot, which is occupied by one spin-up electron (ground state).

<sup>1</sup>This is suggested by transport calculations shown in Fig. 7.5.

**Figure 7.5:** Calculated stability diagram with  $N = 1$  according to a model with two states on the main dot and one on the side dot, all of which are additionally spin-split. Coupling parameters are taken from the experiment and tunneling rates are adjusted accordingly.



The side dot diamond is assumed to be in the charge state  $M = 0$  and thus the secondary resonance with lowest energy (ground state) involves the tunneling of a spin-up electron. These two spin configurations of the quantum dot system can not be transferred one into the other by the hopping of one electron. Therefore, they cannot hybridize and a crossing instead of an anticrossing is observed at the meeting point of the resonances. On the other hand, considering the first excited state of the main dot, the tunneling electron has spin-up and the total spin configuration of the quantum dot setup is identical to the ground state with one spin-up electron on each dot. Thus, these two configurations do hybridize due to the possible hopping of one electron and an anticrossing of the two resonance lines is observed at position (4).

In the stability diagram, the consideration of spin-split states on both quantum dots leads to alternating crossings and anticrossings for ground states and excited states, as it is depicted in the top panel of Fig. 7.4c. This picture matches the observations in Fig. 7.4a. In contrast, assuming all states having identical spin configurations (bottom panel of Fig. 7.4b), and the excited states differ only by their orbital quantum number, no crossings are expected. Assuming that the electron wave functions hybridize for different bands, as one expects for different CNTs, this scenario results in four anticrossings. This is very different from what is observed in the measurements. Therefore, we conclude that we do observe spin-split states in Fig. 7.4a.

For the transport calculations shown in Fig. 7.5, one spin-split state is taken into account for the side dot and two for the main dot. The tunneling rates are adjusted according to the observation of an overall suppressed transport through the main dot. The selective suppression of the hybridization at position (1) and the hybridization of the ground state transitions marked (2) and (3) are reproduced very well, assuming  $N = 1$ . Similarly, both the calculation and the measurement show that the transition involving excited states at position (6) also exhibits a crossing,

in contrast to the anticrossing excitations at positions (4) and (5). The agreement of two anticrossings together with two crossings is most clearly seen at the  $N - 1$  diamond edge with the anticrossings (2) and (5).

A guide to the measurements and calculations is sketched in the central part of Fig. 7.6 where the positions of the crossings and anticrossings are marked again. Above and below the guide, the spin configurations for particular positions are sketched. The charge state of the main dot changes from zero in the  $N - 1 = 0$  diamond to two in the  $N + 1 = 2$  diamond, while the charge state on the side dot stays constantly  $M = 0$ . Along the resonance lines, one additional electron can tunnel via the quantum dot system and depending on the particular spin configuration, hopping of this electron between the two dots is possible or not, leading to anticrossings and crossings.

### 7.3 Conclusions

This chapter presented a detailed analysis of the electronic hybridization between states on parallel carbon nanotube quantum dots. We find that the transport is enhanced when electrons tunnel via the bonding states, which comes along with a negative hybridization amplitude. Furthermore, this denotes the overlap of quantum dot wavefunctions with the same sign, which is a reasonable observation considering their  $s$ -wave like nature. However, this may not be the case for every quantum dot system and, in principle, a positive hybridization amplitude is conceivable, e. g. in complex molecules.

In a magnetic field, the hybridization between the many-body states is found to be selectively suppressed by spin effects. Hence, the electronic hybridization between parallel quantum dots can be manipulated by magnetic fields. Exploiting the differential gating effect discussed in section 4.3.3, spin configurations which do or do not hybridize can be accessed by tuning the gate and bias voltages. This offers the possibility to investigate spin relaxation times of hybridized quantum dot states in comparison to non-hybridized states.

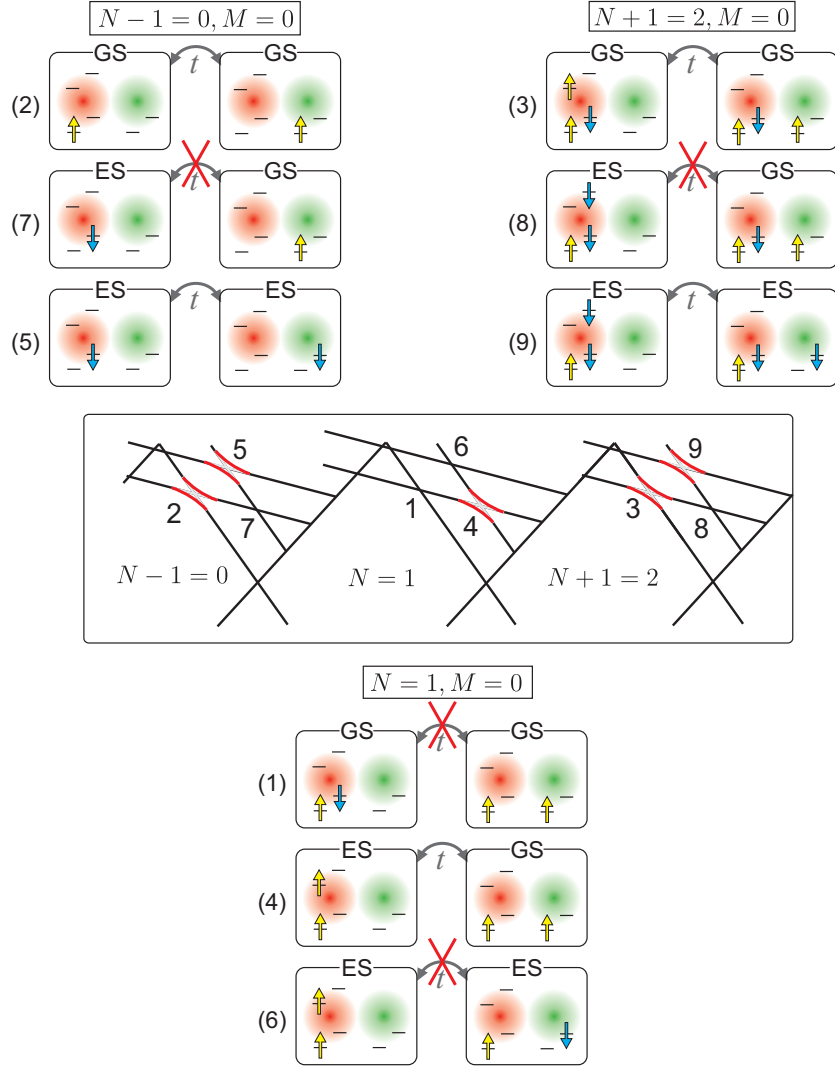


**Figure 7.6:** Center: Guide to the calculation and the measurement at  $B = 10$  T. The anti-bonding states are drawn for completeness, although not observed in the measurement. For each meeting position of resonance lines marked in the guide, the spin configurations of the quantum dot system are sketched. Arrows indicate spin-split states.

## 8 Conclusions and Outlook

This thesis presents a thorough characterization of molecular interactions between carbon nanotubes in a rope. The metallicity, diameter and chirality of the nanotubes incorporated in the rope are identified via vibrational modes observed by tip-enhanced Raman spectroscopy (TERS). These characterized strands of the rope form parallel quantum dots at low temperatures and interaction properties have been probed by quantum transport spectroscopy. The results of quantum transport are strongly supported by and consistent with the additional characterization by TERS representing a novel combination of two independent experimental techniques with great potential in the field of molecular electronics.

A clear resonance effect in tip-enhanced Raman scattering processes, not considered in literature so far, allows for the detection of seven individual nanotubes by their diameter-dependent phonon modes and an assignment to nanotube branches and chiralities. Besides supporting the interpretation of electronic transport phenomena, Raman spectroscopy can directly probe environmental effects on the molecules. Here, the interactions between the strands induce a redshift of the optical transition energies. Furthermore, two of the identified nanotubes can consistently be interpreted as forming a double-walled carbon nanotube. The high spatial resolution of the employed spectroscopic method is a crucial feature to ensure a correct correlation of the two techniques. Furthermore, our results on the structural changes along the rope prove the potential of the tip-enhanced technique to detect single functionalizing molecules connected to a carbon nanotube within a transport device, where standard confocal Raman spectroscopy lacks the necessary local character.

Employing master equation modeling, a model is developed describing two quantum dots contacted in parallel. The model includes two different kinds of interactions between the quantum dots: a capacitive coupling and a tunnel coupling. The manifestations of these interactions in the calculated stability diagrams are not specific to carbon nanotubes, but can be readily transferred to any kind of molecular quantum dots. Energy shifts of resonances in the calculated stability diagram indicate a capacitive coupling between quantum dots. On the other hand, a tunnel coupling, i. e., a hybridization between states of different dots is indicated by anticrossings of resonance lines.



The agreement between transport calculations employing this model and the measured quantum transport of the carbon nanotube rope confirms the formation of interacting parallel quantum dots. The results obtained by the Raman characterization strongly suggest different strands of the rope as the origin of these parallel dots. A differential gating effect inherent to our model is clearly identified in the device and allows for tuning to particular dot configurations and in that manner probing the molecular interactions by quantum transport spectroscopy. A thorough characterization of the magnitude of the electronic hybridization and the capacitive inter-dot coupling of seven parallel quantum dots reveals that the nanotube strands can interact to a very different extent with each other. Amongst the coupled quantum dots, we also find only capacitively interacting or completely uncoupled quantum dots within the one device. Our results show that intertube coupling effects in low-temperature transport may be larger than previously assumed and substantially affect the transport through a device.

Importantly, the hybridization offers the possibility to access the orbitals of contacted molecules via the quantum dot states. The sign of the hybridization amplitude depends on the overlapping wave functions of the quantum dot states which, in principal, comprise the molecular orbitals. For carbon nanotube quantum dots, we find a negative hybridization amplitude denoting the overlap of quantum dot wavefunctions with the same sign, which is a reasonable observation considering their *s*-wave like nature. The hybridization of quantum dot states offers the possibility to detect new physical effects in complex molecules, where a deviation of the negative hybridization amplitude is conceivable. In addition, the combination of two characterization techniques established here, offers a great potential for ropes with only two nanotubes. Then, a direct correlation of one particular carbon nanotube and one quantum dot can be performed, where Raman spectroscopy can determine the atomic structure of the nanotubes and interactions between the quantum dots are probed by quantum transport, as shown here. Calculating the coupling between two specific carbon nanotubes employing atomistic modeling and comparing this with the coupling of the formed parallel quantum dots may provide the link between the quantum dot orbitals and the molecular orbitals. With this knowledge, the hybridization can be used as a direct probe for the orbitals participating in the electronic transport of molecular devices.

The results in this thesis show that the hybridization between parallel quantum dots can be manipulated by magnetic fields leading to a selective suppression of electron tunneling between states of different spin configurations. Again, the differential gating effect can be exploited to tune to different dot configurations and in this case, it allows one to selectively access different spin configurations. The identification of spin states is a crucial prerequisite for spin relaxation experiments, where the gate voltage is pulsed between states of different spins. In a complex system of several interacting quantum dots like the one investigated, however, the discrimination of states with different spin is difficult and the spin-dependent hybridization provides

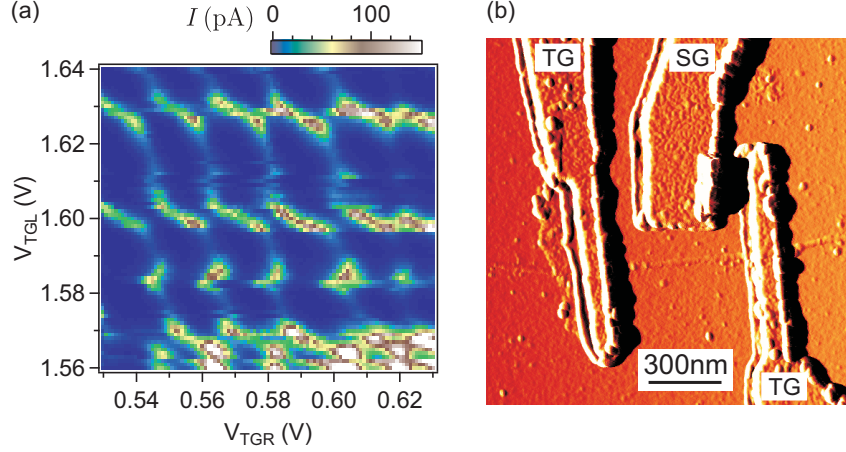


**Figure 8.1:** (a) Current through a device (not shown) with three top gates and two leads. The voltage of the central gate is constant,  $V_{\text{bias}} = 0.3 \text{ mV}$  and the voltage of the two outer top gates ( $TG_L$  and  $TG_R$ ) is varied. The nanotube in this device is covered with gate oxide in the complete gate region. (b) Atomic force micrograph of a carbon nanotube quantum dot defined by two top gates (TG) to tune the tunnel barriers and one side gate (SG) to tune the dot potential. The contacts to the nanotube are further away and not shown. 15 nm  $\text{Al}_2\text{O}_3$  gate oxide separates the nanotube from the gate metal (2 nm Ti/50 nm Pd).

a possibility for the identification. Furthermore, the investigation of spin relaxation times of hybridized quantum dot states in comparison to non-hybridized states, is expected to reveal interesting phenomena.

A crucial prerequisite for such spin relaxation experiments are tunable tunnel barriers of the quantum dots to adjust the electron tunneling rates [Fujisawa03, Elzerman04]. The tunability can be achieved by defining the quantum dot via top gate structures, which also allows for the design of serial multiple quantum dots [Mason04, Biercuk05, Sapmaz06b, Gräber06]. First steps towards top gate defined quantum dots have been performed within this work and are the subject of ongoing research.

In contrast to the fabrication of the gate oxide by thermal evaporation or atomic layer deposition, we deposit  $\text{Al}_2\text{O}_3$  on top of a carbon nanotube by pulsed laser deposition. One fabrication route involves the complete coverage of the nanotube in the gate region with square shaped structures of the oxide and a subsequent patterning of contact and gate structures on top. The current as a function of the gate voltage in Fig. 8.1a shows the good tunability of the device via the top gates. However, charge rearrangements disturb the transport measurements. This

indicates the presence of various disorder potentials, probably due to the coverage of the nanotube, inhibiting the formation of a defined quantum dot. Instead, device structures, where the nanotube is left uncovered in the region where the quantum dot is expected to form (see Fig. 8.1b), promise decreased disorder potentials interfering with transport measurements. Such a device pattern for a carbon nanotube rope offers the possibility to perform voltage pulse experiments in order to obtain spin relaxation times in a system of coupled quantum dots connected in parallel.

For the chiral index assignment in this work, the nanotube diameters are determined via the diameter-dependent phonon modes in the Raman spectrum. Although this leads already to only a small group of possible chiralities, one may like to narrow the possible chiral indices even further to one particular  $(n, m)$  index pair. This requires more information about the effect of the tip-enhancement on the resonance window for the investigated Raman modes. As mentioned above, knowing the exact chiral indices is a prerequisite for the atomistic modeling of the nanotubes which may provide the link between the quantum dot orbitals and the molecular orbitals.

Recently, interactions between the shells of a multiwalled carbon nanotube have been found to strongly affect the energy of the particular radial breathing modes in the Raman spectrum [Spudat10]. The experiments presented in this thesis show the feasibility to investigate these interactions from two different physical viewpoints on the same device by probing the same mode of a particular nanotube in a three-terminal device setup using Raman spectroscopy and quantum transport measurements. It has been shown that phonon excitations can be observed in quantum transport [Sapmaz06a, Leturcq09, Hüttel09b] and, in principle, the radial breathing mode is in the energy range accessible with electrical transport, as shown in a scanning tunneling microscope setup [LeRoy04].

Such a correlation of phonon modes requires an independent determination of the atomic structure of the carbon nanotubes. This can be achieved by transmission electron microscopy and electron diffraction, if the sample geometry is appropriate. This involves device patterning on thin  $\text{Si}_3\text{N}_4$  membranes, where the nanotubes span across etched holes in the membrane. The feasibility of the combination of the three experimental techniques – room temperature electronic transport, Raman spectroscopy and transmission electron microscopy – has recently been shown by our group [Frielinghaus11]. The upcoming experiments in low-temperature transport using this sample geometry pursue the results of this thesis.

# Appendix

## A Supplementary information for Raman spectroscopy

### Parameters for the diameter dependence of the RBM

Figure 2.10 gives borders for the diameter dependence of the radial breathing mode (RBM) according to different parameters  $A$  and  $B$  in Eq. 2.15. Publications taken into account for the estimate of the border are given in Tab. A.1. These parameters are also employed for the evaluation of possible nanotube diameters in Fig. 3.9 in section 3.3.2.

### Indexing the carbon nanotubes

To follow the assignment of particular  $(n, m)$  chiral indices to carbon nanotubes within the nanotube rope in section 3.3.3, the Kataura plot in Fig. A.1 is extended by one specific  $(n, m)$  for each branch, which are not given in the plot in the chapter (see Fig. 3.12). The remaining chiral indices can be calculated using Eq. 2.14.

The discussion about the chiral index assignment in section 3.3.3 includes a large error for the resonance energy in the Kataura plot. For the diameter evaluation, however, only the systematic error due to the spectral resolution is taken into account. Figure A.2 plots minimal and maximal diameters obtained from the observed RBM frequencies, considering different values for the parameters  $A$  and  $B$ . Although, the assignment to one specific chiral index pair  $(n, m)$  may change for a particular nanotube, the branch index is generally maintained.

## APPENDIX

reference	sample	$A$ ( $\text{cm}^{-1}\text{nm}$ )	$B$ ( $\text{cm}^{-1}$ )
[Bandow98]	laser ablation bundled SWNTs	223.75	0
[Alvarez00]	solar radiation <sup>a</sup> bundled SWNTs	215	18
[Jorio01a]	CVD isolated SWNTs on Si/SiO <sub>2</sub>	248	0
[Bachilo02]	HiPCO SWNTs SDS-wrapped in solution	223.5	12.5
[Kramberger03]	annealing of peapods inner nanotubes of DWNTs	233	14
[Fantini04]	HiPCO SWNTs SDS-wrapped in solution semiconducting	223	10
[Fantini04]	HiPCO SWNTs SDS-wrapped in solution metallic	218	17
[Telg04]	HiPCO SWNTs SDS/SDBS-wrapped in solution	215	18
[Jorio05]	HiPCO SWNTs SDS-wrapped in solution	218.3	15.9
[Meyer05]	CVD freestanding, individual CNTs	204	27
[Araujo08]	water assisted CVD vertical, isolated SWNTs	227	0

**Table A.1:** The parameters  $A$  and  $B$  for the diameter dependence of the RBM frequency  $\omega^{\text{R}} = A/d + B$  from different references. These were used to evaluate the diameters in Fig. 3.9. SDS = sodium dodecyl sulfate; SDBS = sodium dodecylbenzene sulfonate

<sup>a</sup> see [Guillard99] for synthesis method

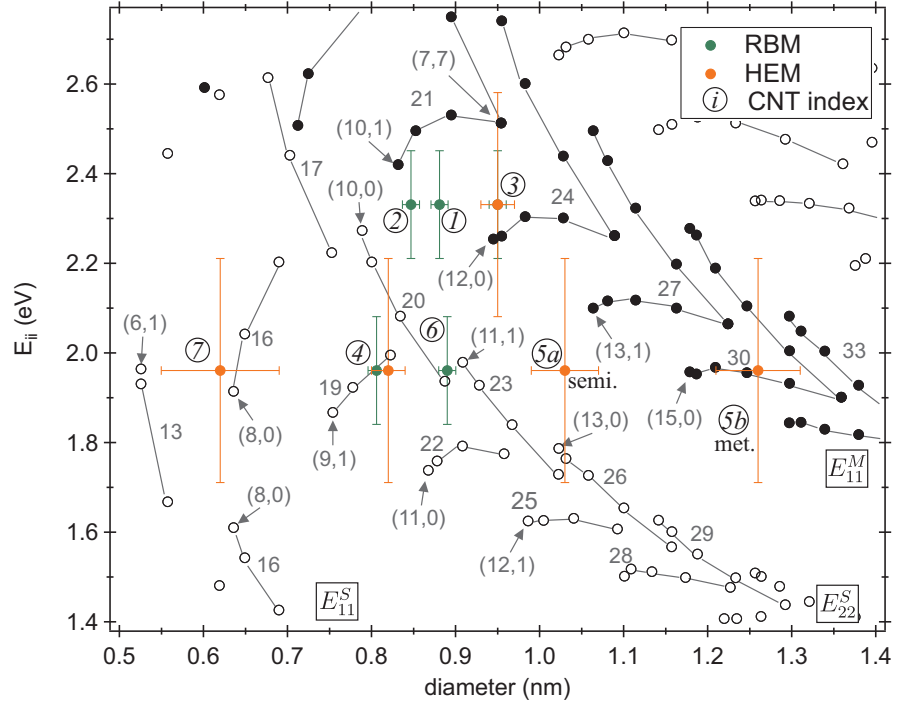


**Figure A.1:** Kataura plot. Optical transition energies  $E_{ii}^{M/S}$  as a function of the diameter of  $(n, m)$  nanotubes [Popov04]. Solid circles denote metallic nanotubes, open circles denote semiconducting ones. Solid lines indicate nanotubes belonging to one branch index  $b = (2n + m) = \text{const}$  given by the numbers. Experimental values are indicated by the CNT index  $i$ . For each branch one specific  $(n, m)$  value is given.

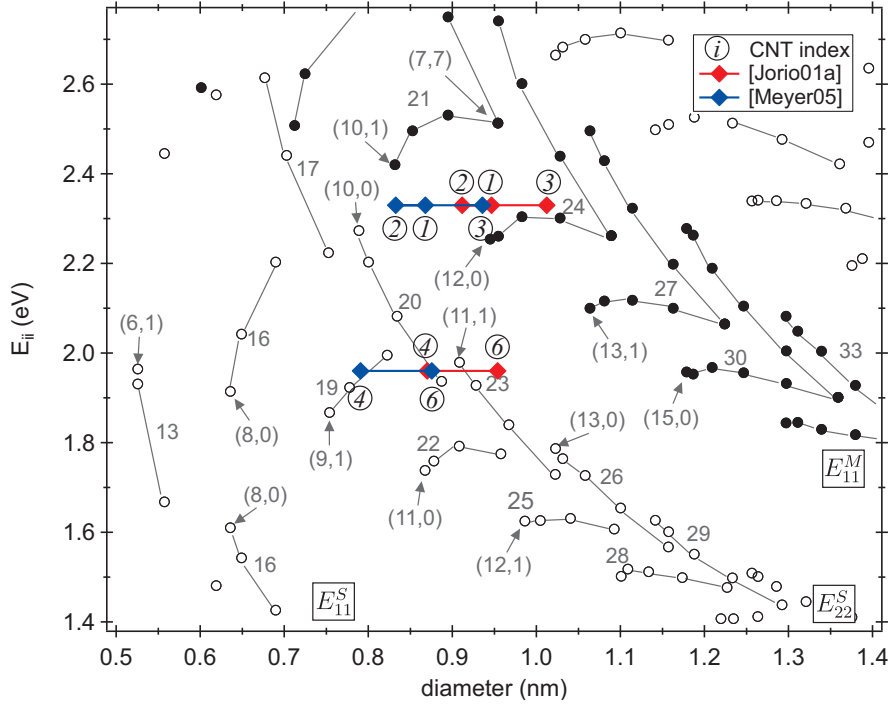


**Figure A.2:** Kataura plot. Optical transition energies  $E_{ii}^{M/S}$  as a function of the diameter of  $(n, m)$  nanotubes [Popov04]. Solid circles denote metallic nanotubes, open circles denote semiconducting ones. Solid lines indicate nanotubes belonging to one branch index  $b = (2n + m) = \text{const}$  given by the numbers. Experimental values obtained from the RBMs are indicated by the CNT index  $i$ . Blue and red indicate the minimal and maximal diameters, respectively, obtained employing different parameters  $A$  and  $B$  in Eq. 2.15. Parameters are given in Tab. A.1.

structure size	beam step size (nm)	current (nA)	dose ( $\mu\text{C}/\text{cm}^2$ )
20-800 $\mu\text{m}$	12.5	10	265
0.5-1.0 $\mu\text{m}$	12.5	10	345
6-200 $\mu\text{m}$	50	150	280
0.2-4 $\mu\text{m}$	2.5	1	500
35-200 nm	2.5	1	750

**Table B.2:** Process parameters for electron beam writing for structures of different size and resolution.

## B Supplementary information for the device fabrication

For establishing the electron beam lithography (EBL) process, dose tests were carried out with metal test structures of different sizes. The resulting ideal parameters are given in Tab. B.2. Larger structures (20-800  $\mu\text{m}$ ), which require a good precision, e.g. alignment markers, are written with a beam step size of 12.5 nm, but require the smallest dose. Smaller marker structures such as the AFM markers with a size of 0.5-1.0  $\mu\text{m}$  are written with the same resolution, but need a higher dose. In order to save writing time, large structures which do not need a high resolution, can be written with 50 nm beam step size. The fine contacts and gates running to the carbon nanotube have to be precisely written with respect to each other and to the nanotube. Hence, a small beam step size of 2.5 nm is chosen. Structure sizes down to 200 nm require a higher dose of  $500 \mu\text{C}/\text{cm}^2$ , and the smallest structures possible with our process (lines with a width of 35 nm) require an even higher dose. In all cases, the current is adjusted according to the beam step size. However, a value for the beam size can only be estimated from the current. Roughly, a 1 nA beam exhibits a beam size around  $\sim 4$  nm and 150 nA have a beam size of  $\sim 50$  nm.





# Bibliography

- [Ajiki95] H. Ajiki and T. Ando. *Carbon Nanotubes: Optical Absorption in Aharonov-Bohm Flux*. Japanese Journal of Applied Physics, Supplement **34-1**, 107 (1995).
- [Alvarez00] L. Alvarez, A. Righi, T. Guillard, S. Rols, E. Anglaret, D. Laplaze, and J.-L. Sauvajol. *Resonant Raman study of the structure and electronic properties of single-wall carbon nanotubes*. Chemical Physics Letters **316**, 186 (2000).
- [Anderson05] N. Anderson, A. Hartschuh, S. Cronin, and L. Novotny. *Nanoscale vibrational analysis of single-walled carbon nanotubes*. Journal of the American Chemical Society **127**, 2533 (2005).
- [Anderson07] N. Anderson, A. Hartschuh, and L. Novotny. *Chirality Changes in Carbon Nanotubes Studied with Near-Field Raman Spectroscopy*. Nano Letters **7**, 577 (2007).
- [Araujo08] P. T. Araujo, I. O. Maciel, P. B. C. Pesce, M. A. Pimenta, S. K. Doorn, H. Qian, A. Hartschuh, M. Steiner, L. Grigorian, K. Hata, and A. Jorio. *Nature of the constant factor in the relation between radial breathing mode frequency and tube diameter for single-wall carbon nanotubes*. Physical Review B **77**, 241403 (2008).
- [Ashoori96] R. C. Ashoori. *Electrons in artificial atoms*. Nature **379**, 413 (1996).
- [Atatüre06] M. Atatüre, J. Dreiser, A. Badolato, A. Högele, K. Karrai, and A. Imamoglu. *Quantum-Dot Spin-State Preparation with Near-Unity Fidelity*. Science **312**, 551 (2006).
- [Averin90] D. V. Averin and Yu. V. Nazarov. *Virtual electron diffusion during quantum tunneling of the electric charge*. Physical Review Letters **65**, 2446 (1990).

## BIBLIOGRAPHY

---

- [Averin91] D. V. Averin, A. N. Korotkov, and K. K. Likharev. *Theory of single-electron charging of quantum wells and dots*. Physical Review B **44**, 6199 (1991).
- [Bachilo02] S. M. Bachilo, M. S. Strano, C. Kittrell, R. H. Hauge, R. E. Smalley, and R. B. Weisman. *Structure-Assigned Optical Spectra of Single-Walled Carbon Nanotubes*. Science **298**, 2361 (2002).
- [Bandow98] S. Bandow, S. Asaka, Y. Saito, A. M. Rao, L. Grigorian, E. Richter, and P. C. Eklund. *Effect of the Growth Temperature on the Diameter Distribution and Chirality of Single-Wall Carbon Nanotubes*. Physical Review Letters **80**, 3779 (1998).
- [Beenakker91] C. W. J. Beenakker. *Theory of Coulomb-blockade oscillations in the conductance of a quantum dot*. Physical Review B **44**, 1646 (1991).
- [Benjamin06] S. C. Benjamin, A. Ardavan, G. A. D. Briggs, D. A. Britz, D. Gunlycke, J. Jefferson, M. A. G. Jones, D. F. Leigh, B. W. Lovett, A. N. Khlobystov, S. A. Lyon, J. J. L. Morton, K. Porfyrakis, M. R. Sambrook, and A. M. Tyryshkin. *Towards a fullerene-based quantum computer*. Journal of Physics - Condensed Matter **18**, S867 (2006).
- [Bethune93] D. S. Bethune, C. H. Kiang, M. S. Devries, G. Gorman, R. Savoy, J. Vazquez, and R. Beyers. *Cobalt-catalysed growth of carbon nanotubes with single-atomic-layer walls*. Nature **363**, 605 (1993).
- [Biercuk05] M. J. Biercuk, S. Garaj, N. Mason, J. M. Chow, and C. M. Marcus. *Gate-Defined Quantum Dots on Carbon Nanotubes*. Nano Letters **5**, 1267 (2005).
- [Björk04] M. T. Björk, C. Thelander, A. E. Hansen, L. E. Jensen, M. W. Larsson, L. R. Wallenberg, and L. Samuelson. *Few-electron quantum dots in nanowires*. Nano Letters **4**, 1621 (2004).
- [Bockrath97] M. Bockrath, D. H. Cobden, P. L. McEuen, N. G. Chopra, A. Zettl, A. Thess, and R. E. Smalley. *Single-electron transport in ropes of carbon nanotubes*. Science **275**, 1922 (1997).
- [Bogani08] L. Bogani and W. Wernsdorfer. *Molecular spintronics using single-molecule magnets*. Nature Materials **7**, 179 (2008).

- 
- [Bogani10] L. Bogani, R. Maurand, L. Marty, C. Sangregorio, C. Altavilla, and W. Wernsdorfer. *Effect of sequential grafting of magnetic nanoparticles onto metallic and semiconducting carbon-nanotube devices: towards self-assembled multi-dots*. Journal of Materials Chemistry **20**, 2099 (2010).
- [Bose05] S. M. Bose, S. Gayen, and S. N. Behera. *Theory of the tangential G-band feature in the Raman spectra of metallic carbon nanotubes*. Physical Review B **72**, 153402 (2005).
- [Bronikowski01] M. J. Bronikowski, P. A. Willis, D. T. Colbert, K. A. Smith, and R. E. Smalley. *Gas-phase production of carbon single-walled nanotubes from carbon monoxide via the HiPco process: A parametric study*. Journal of Vacuum Science & Technology A – Vacuum Surfaces and Films **19**, 1800 (2001).
- [Brown01] S. D. M. Brown, A. Jorio, P. Corio, M. S. Dresselhaus, G. Dresselhaus, R. Saito, and K. Kneipp. *Origin of the Breit-Wigner-Fano lineshape of the tangential G-band feature of metallic carbon nanotubes*. Physical Review B **63**, 155414 (2001).
- [Bruus04] H. Bruus and K. Flensberg. *Many-Body Quantum Theory in Condensed Matter Physics*. Oxford University Press, New York, (2004).
- [Büttiker86] M. Büttiker. *Four-Terminal Phase-Coherent Conductance*. Physical Review Letters **57**, 1761 (1986).
- [Cançado09a] L. G. Cançado, A. Hartschuh, and L. Novotny. *Tip-enhanced Raman spectroscopy of carbon nanotubes*. Journal of Raman Spectroscopy **40**, 1420 (2009).
- [Cançado09b] L. G. Cançado, A. Jorio, A. Ismach, E. Joselevich, A. Hartschuh, and L. Novotny. *Mechanism of Near-Field Raman Enhancement in One-Dimensional Systems*. Physical Review Letters **103**, 186101 (2009).
- [Cantone08] A. L. Cantone, M. R. Buitelaar, C. G. Smith, D. Anderson, G. A. C. Jones, S. J. Chorley, C. Casiraghi, A. Lombardo, A. C. Ferrari, H. Shinohara, A. Ardavan, J. Warner, A. A. R. Watt, K. Porfyrakis, and G. A. D. Briggs. *Electronic transport characterization of Sc @ C-82 single-wall carbon nanotube peapods*. Journal of Applied Physics **104**, 083717 (2008).

## BIBLIOGRAPHY

---

- [Chen03] B. Chen, M. Gao, J. M. Zuo, S. Qu, B. Liu, and Y. Huang. *Binding energy of parallel carbon nanotubes*. Applied Physics Letters **83**, 3570 (2003).
- [Cobden02] D. H. Cobden and J. Nygård. *Shell Filling in Closed Single-Wall Carbon Nanotube Quantum Dots*. Physical Review Letters **89**, 046803 (2002).
- [Dabbousi95] B. O. Dabbousi, M. G. Bawendi, O. Onitsuka, and M. F. Rubner. *Electroluminescence from CdSe Quantum-Dot Polymer Composites*. Applied Physics Letters **66**, 1316 (1995).
- [Dai96] H. J. Dai, J. H. Hafner, A. G. Rinzler, D. T. Colbert, and R. E. Smalley. *Nanotubes as nanoprobe in scanning probe microscopy*. Nature **384**, 147 (1996).
- [Damnjanović99] M. Damnjanović, I. Miloscaronević, T. Vuković, and R. Sredanović. *Full symmetry, optical activity, and potentials of single-wall and multiwall nanotubes*. Physical Review B **60**, 2728 (1999).
- [De Franceschi01] S. De Franceschi, S. Sasaki, J. M. Elzerman, W. G. van der Wiel, S. Tarucha, and L. P. Kouwenhoven. *Electron Cotunneling in a Semiconductor Quantum Dot*. Physical Review Letters **86**, 878 (2001).
- [Débarre08] A. Débarre, M. Kobylko, A. M. Bonnot, A. Richard, V. N. Popov, L. Henrard, and M. Kociak. *Electronic and Mechanical Coupling of Carbon Nanotubes: A Tunable Resonant Raman Study of Systems with Known Structures*. Physical Review Letters **101**, 197403 (2008).
- [Dekker99] C. Dekker. *Carbon nanotubes as molecular quantum wires*. Physics Today **52**, 22 (1999).
- [Dresselhaus05] M. S. Dresselhaus, G. Dresselhaus, R. Saito, and A. Jorio. *Raman spectroscopy of carbon nanotubes*. Physics Reports **409**, 47 (2005).
- [Dubay02] O. Dubay, G. Kresse, and H. Kuzmany. *Phonon Softening in Metallic Nanotubes by a Peierls-like Mechanism*. Physical Review Letters **88**, 235506 (2002).
- [Ebbesen92] T. W. Ebbesen and P. M. Ajayan. *Large-scale synthesis of carbon nanotubes*. Nature **358**, 220 (1992).

- [Eliassen10] A. Eliassen, J. Paaske, K. Flensberg, S. Smerat, M. Leijnse, M. R. Wegewijs, H. I. Jørgensen, M. Monthieux, and J. Nygård. *Transport via coupled states in a C60 peapod quantum dot*. Physical Review B **81**, 155431 (2010).
- [Elzerman04] J. M. Elzerman, R. Hanson, L. H. Willems van Beveren, B. Witkamp, L. M. K. Vandersypen, and L. P. Kouwenhoven. *Single-shot read-out of an individual electron spin in a quantum dot*. Nature **430**, 431 (2004).
- [Esconjauregui10] S. Esconjauregui, M. Fouquet, B. C. Bayer, C. Ducati, R. Smajda, S. Hofmann, and J. Robertson. *Growth of Ultrahigh Density Vertically Aligned Carbon Nanotube Forests for Interconnects*. ACS Nano **4**, 7431 (2010).
- [Fantini04] C. Fantini, A. Jorio, M. Souza, M. S. Strano, M. S. Dresselhaus, and M. A. Pimenta. *Optical Transition Energies for Carbon Nanotubes from Resonant Raman Spectroscopy: Environment and Temperature Effects*. Physical Review Letters **93**, 147406 (2004).
- [Fantini07] C. Fantini, M. L. Usrey, and M. S. Strano. *Investigation of electronic and vibrational properties of single-walled carbon nanotubes functionalized with diazonium salts*. Journal of Physical Chemistry C **111**, 17941 (2007).
- [Fouquet09] M. Fouquet, H. Telg, J. Maultzsch, Y. Wu, B. Chandra, J. Hone, T. F. Heinz, and C. Thomsen. *Longitudinal Optical Phonons in Metallic and Semiconducting Carbon Nanotubes*. Physical Review Letters **102**, 075501 (2009).
- [Frielinghaus11] R. Frielinghaus, K. Goß, S. Trellenkamp, L. Houben, C. M. Schneider, and C. Meyer. *Comprehensive characterization of an individual carbon nanotube transport device*. arXiv:1105.4244, (2011).
- [Fujisawa03] T. Fujisawa, D. G. Austing, Y. Tokura, Y. Hirayama, and S. Tarucha. *Electrical pulse measurement, inelastic relaxation, and non-equilibrium transport in a quantum dot*. Journal of Physics - Condensed Matter **15**, R1395 (2003).
- [Geim07] A. K. Geim and K. S. Novoselov. *The rise of graphene*. Nature Materials **6**, 183 (2007).

## BIBLIOGRAPHY

---

- [Geim09] A. K. Geim. *Graphene: Status and Prospects*. Science **324**, 1530 (2009).
- [Georgi10] C. Georgi and A. Hartschuh. *Tip-enhanced Raman spectroscopic imaging of localized defects in carbon nanotubes*. Applied Physics Letters **97**, 143117 (2010).
- [Ghosh05] S. Ghosh, H. Halimun, A. K. Mahapatro, J. Choi, S. Lodha, and D. Janes. *Device structure for electronic transport through individual molecules using nanoelectrodes*. Applied Physics Letters **87**, 233509 (2005).
- [Girifalco00] L. A. Girifalco, Miroslav Hodak, and Roland S. Lee. *Carbon nanotubes, buckyballs, ropes, and a universal graphitic potential*. Physical Review B **62**, 13104 (2000).
- [Gräber06] M. R. Gräber, W. A. Coish, C. Hoffmann, M. Weiss, J. Furer, S. Oberholzer, D. Loss, and C. Schönenberger. *Molecular states in carbon nanotube double quantum dots*. Physical Review B **74**, 075427 (2006).
- [Grove-Rasmussen08] K. Grove-Rasmussen, H. I. Jørgensen, T. Hayashi, P. E. Lindelof, and T. Fujisawa. *A Triple Quantum Dot in a Single-Wall Carbon Nanotube*. Nano Letters **8**, 1055 (2008).
- [Grove-Rasmussen09] K. Grove-Rasmussen, H. I. Jørgensen, B. M. Andersen, J. Paaske, T. S. Jespersen, J. Nygård, K. Flensberg, and P. E. Lindelof. *Superconductivity-enhanced bias spectroscopy in carbon nanotube quantum dots*. Physical Review B **79**, 134518 (2009).
- [Guillard99] T. Guillard, S. Cetout, L. Alvarez, J. L. Sauvajol, E. Anglaret, P. Bernier, G. Flamant, and D. Laplaze. *Production of carbon nanotubes by the solar route*. European Physical Journal – Applied Physics **5**, 251 (1999).
- [Guo06] X. F. Guo, J. P. Small, J. E. Klare, Y. L. Wang, M. S. Purewal, I. W. Tam, B. H. Hong, R. Caldwell, L. M. Huang, S. O'Brien, J. M. Yan, R. Breslow, S. J. Wind, J. Hone, P. Kim, and C. Nuckolls. *Covalently bridging gaps in single-walled carbon nanotubes with conducting molecules*. Science **311**, 356 (2006).
- [Guo07] X. Guo, A. Whalley, J. E. Klare, L. Huang, S. O'Brien, M. Steigerwald, and C. Nuckolls. *Single-molecule devices as*

- scaffolding for multicomponent nanostructure assembly. *Nano Letters* **7**, 1119 (2007).
- [Guo09] X. Guo and C. Nuckolls. *Functional single-molecule devices based on SWNTs as point contacts*. *Journal of Materials Chemistry* **19**, 5470 (2009).
- [Hanson07] R. Hanson, L. P. Kouwenhoven, J. R. Petta, S. Tarucha, and L. M. K. Vandersypen. *Spins in few-electron quantum dots*. *Reviews of Modern Physics* **79**, 1217 (2007).
- [Hartschuh03] A. Hartschuh, E. J. Sánchez, X. S. Xie, and L. Novotny. *High-Resolution Near-Field Raman Microscopy of Single-Walled Carbon Nanotubes*. *Physical Review Letters* **90**, 095503 (2003).
- [Hartschuh08] A. Hartschuh. *Tip-Enhanced Near-Field Optical Microscopy*. *Angewandte Chemie – International Edition* **47**, 8178 (2008).
- [Heersche06] H. B. Heersche, Z. de Groot, J. A. Folk, H. S. J. van der Zant, C. Romeike, M. R. Wegewijs, L. Zobbi, D. Barreca, E. Tondello, and A. Cornia. *Electron transport through single Mn-12 molecular magnets*. *Physical Review Letters* **96**, 206801 (2006).
- [Heinze02] S. Heinze, J. Tersoff, R. Martel, V. Derycke, J. Appenzeller, and Ph. Avouris. *Carbon Nanotubes as Schottky Barrier Transistors*. *Physical Review Letters* **89**, 106801 (2002).
- [Henrard99] L. Henrard, E. Hernández, P. Bernier, and A. Rubio. *van der Waals interaction in nanotube bundles: Consequences on vibrational modes*. *Physical Review B* **60**, R8521 (1999).
- [Holm08] J. V. Holm, H. I. Jørgensen, K. Grove-Rasmussen, J. Paaske, K. Flensberg, and P. E. Lindelof. *Gate-dependent tunneling-induced level shifts observed in carbon nanotube quantum dots*. *Physical Review B* **77**, 161406 (2008).
- [Hüttel08] A. K. Hüttel, M. Poot, B. Witkamp, and H. S. J. van der Zant. *Nanoelectromechanics of suspended carbon nanotubes*. *New Journal of Physics* **10**, 095003 (2008).
- [Hüttel09a] A. K. Hüttel, G. A. Steele, B. Witkamp, M. Poot, L. P. Kouwenhoven, and H. S. J. van der Zant. *Carbon Nanotubes as Ultrahigh Quality Factor Mechanical Resonators*. *Nano Letters* **9**, 2547 (2009).



## BIBLIOGRAPHY

---

- [Hüttel09b] A. K. Hüttel, B. Witkamp, M. Leijnse, M. R. Wegewijs, and H. S. J. van der Zant. *Pumping of Vibrational Excitations in the Coulomb-Blockade Regime in a Suspended Carbon Nanotube*. Physical Review Letters **102**, 225501 (2009).
- [Iijima91] S. Iijima. *Helical microtubules of graphitic carbon*. Nature **354**, 56 (1991).
- [Ilani06] S. Ilani, L. A. K. Donev, M. Kindermann, and P. L. McEuen. *Measurement of the quantum capacitance of interacting electrons in carbon nanotubes*. Nature Physics **2**, 687 (2006).
- [Javey03] A. Javey, J. Guo, Q. Wang, M. Lundstrom, and H. J. Dai. *Ballistic carbon nanotube field-effect transistors*. Nature **424**, 654 (2003).
- [Jishi93] R. A. Jishi, L. Venkataraman, M. S. Dresselhaus, and G. Dresselhaus. *Phonon modes in carbon nanotubes*. Chemical Physics Letters **209**, 77 (1993).
- [Johnson92] A. T. Johnson, L. P. Kouwenhoven, W. de Jong, N. C. van der Vaart, C. J. P. M. Harmans, and C. T. Foxon. *Zero-dimensional states and single electron charging in quantum dots*. Physical Review Letters **69**, 1592 (1992).
- [Jorio01a] A. Jorio, R. Saito, J. H. Hafner, C. M. Lieber, M. Hunter, T. McClure, G. Dresselhaus, and M. S. Dresselhaus. *Structural (n, m) Determination of Isolated Single-Wall Carbon Nanotubes by Resonant Raman Scattering*. Physical Review Letters **86**, 1118 (2001).
- [Jorio01b] A. Jorio, A. G. Souza Filho, G. Dresselhaus, M. S. Dresselhaus, R. Saito, J. H. Hafner, C. M. Lieber, F. M. Matinaga, M. S. S. Dantas, and M. A. Pimenta. *Joint density of electronic states for one isolated single-wall carbon nanotube studied by resonant Raman scattering*. Physical Review B **63**, 245416 (2001).
- [Jorio02a] A. Jorio, C. Fantini, M. S. S. Dantas, M. A. Pimenta, A. G. Souza Filho, Ge. G. Samsonidze, V. W. Brar, G. Dresselhaus, M. S. Dresselhaus, A. K. Swan, M. S. Ünlü, B. B. Goldberg, and R. Saito. *Linewidth of the Raman features of individual single-wall carbon nanotubes*. Physical Review B **66**, 115411 (2002).

- [Jorio02b] A. Jorio, A. G. Souza Filho, G. Dresselhaus, M. S. Dresselhaus, A. K. Swan, M. S. Ünlü, B. B. Goldberg, M. A. Pimenta, J. H. Hafner, C. M. Lieber, and R. Saito. *G-band resonant Raman study of 62 isolated single-wall carbon nanotubes*. Physical Review B **65**, 155412 (2002).
- [Jorio03a] A. Jorio, M. A. Pimenta, A. G. Souza, R. Saito, G. Dresselhaus, and M. S. Dresselhaus. *Characterizing carbon nanotube samples with resonance Raman scattering*. New Journal of Physics **5**, 139 (2003).
- [Jorio03b] A. Jorio, M. A. Pimenta, A. G. Souza Filho, Ge. G. Samsonidze, A. K. Swan, M. S. Ünlü, B. B. Goldberg, R. Saito, G. Dresselhaus, and M. S. Dresselhaus. *Resonance Raman Spectra of Carbon Nanotubes by Cross-Polarized Light*. Physical Review Letters **90**, 107403 (2003).
- [Jorio05] A. Jorio, C. Fantini, M. A. Pimenta, R. B. Capaz, Ge. G. Samsonidze, G. Dresselhaus, M. S. Dresselhaus, J. Jiang, N. Kobayashi, A. Grüneis, and R. Saito. *Resonance Raman spectroscopy  $(n,m)$ -dependent effects in small-diameter single-wall carbon nanotubes*. Physical Review B **71**, 075401 (2005).
- [Kaasbjerg08] K. Kaasbjerg and K. Flensberg. *Strong Polarization-Induced Reduction of Addition Energies in Single-Molecule Nanojunctions*. Nano Letters **8**, 3809 (2008).
- [Kastner93] M. A. Kastner. *Artificial Atoms*. Physics Today **46**, 24 (1993).
- [Ke07] S.-H. Ke, H. U. Baranger, and W. Yang. *Contact transparency of nanotube-molecule-nanotube junctions*. Physical Review Letters **99**, 146802 (2007).
- [Kempa02] K. Kempa. *Gapless plasmons in carbon nanotubes and their interactions with phonons*. Physical Review B **66**, 195406 (2002).
- [Kiang98] C.-H. Kiang, M. Endo, P. M. Ajayan, G. Dresselhaus, and M. S. Dresselhaus. *Size Effects in Carbon Nanotubes*. Physical Review Letters **81**, 1869 (1998).
- [Kim05] W. Kim, A. Javey, R. Tu, J. Cao, Q. Wang, and H. J. Dai. *Electrical contacts to carbon nanotubes down to 1 nm in diameter*. Applied Physics Letters **87**, 173101 (2005).

## BIBLIOGRAPHY

---

- [Kneipp00] K. Kneipp, H. Kneipp, P. Corio, S. D. M. Brown, K. Shafer, J. Motz, L. T. Perelman, E. B. Hanlon, A. Marucci, G. Dresselhaus, and M. S. Dresselhaus. *Surface-Enhanced and Normal Stokes and Anti-Stokes Raman Spectroscopy of Single-Walled Carbon Nanotubes*. Physical Review Letters **84**, 3470 (2000).
- [Kong98] J. Kong, H. T. Soh, A. M. Cassell, C. F. Quate, and H. J. Dai. *Synthesis of individual single-walled carbon nanotubes on patterned silicon wafers*. Nature **395**, 878 (1998).
- [Kong01] J. Kong, E. Yenilmez, T. W. Tombler, W. Kim, H.J. Dai, R. B. Laughlin, L. Liu, C. S. Jayanthi, and S. Y. Wu. *Quantum Interference and Ballistic Transmission in Nanotube Electron Waveguides*. Physical Review Letters **87**, 106801 (2001).
- [Kouwenhoven97] L. P. Kouwenhoven, C. M. Marcus, P. L. McEuen, S. Tarucha, R. M. Westervelt, and N. S. Wingreen. *Mesoscopic Electron Transport*, chapter Electron Transport in Quantum Dots. Kluwer Academic Publishers, (1997).
- [Kouwenhoven01] L. P. Kouwenhoven, D. G. Austing, and S. Tarucha. *Few-electron quantum dots*. Reports on Progress in Physics **64**, 701 (2001).
- [Kramberger03] Ch. Kramberger, R. Pfeiffer, H. Kuzmany, V. Zólyomi, and J. Kürti. *Assignment of chiral vectors in carbon nanotubes*. Physical Review B **68**, 235404 (2003).
- [Kürti02] J. Kürti, V. Zólyomi, A. Grüneis, and H. Kuzmany. *Double resonant Raman phenomena enhanced by van Hove singularities in single-wall carbon nanotubes*. Physical Review B **65**, 165433 (2002).
- [Landauer57] R. Landauer. *Spatial Variation of Currents and Fields due to Localized Scatterers in Metallic Conduction*. IBM Journal of Research and Development **1**, 223 (1957).
- [Lazzeri06] M. Lazzeri, S. Piscanec, F. Mauri, A. C. Ferrari, and J. Robertson. *Phonon linewidths and electron-phonon coupling in graphite and nanotubes*. Physical Review B **73**, 155426 (2006).

- [Lemay01] S. G. Lemay, J. W. Janssen, M. van den Hout, M. Mooij, M. J. Bronikowski, P. A. Willis, R. E. Smalley, L. P. Kouwenhoven, and C. Dekker. *Two-dimensional imaging of electronic wavefunctions in carbon nanotubes*. Nature **412**, 617 (2001).
- [LeRoy04] B. J. LeRoy, S. G. Lemay, J. Kong, and C. Dekker. *Electrical generation and absorption of phonons in carbon nanotubes*. Nature **432**, 371 (2004).
- [Leturcq09] R. Leturcq, C. Stampfer, K. Inderbitzin, L. Durrer, C. Hierold, E. Mariani, M. G. Schultz, F. von Oppen, and K. Ensslin. *Franck-Condon blockade in suspended carbon nanotube quantum dots*. Nature Physics **5**, 327 (2009).
- [Liang01] W. Liang, M. Bockrath, D. Bozovic, J. H. Hafner, M. Tinkham, and H. Park. *Fabry - Perot interference in a nanotube electron waveguide*. Nature **411**, 665 (2001).
- [Liang02] W. Liang, M. Bockrath, and H. Park. *Shell Filling and Exchange Coupling in Metallic Single-Walled Carbon Nanotubes*. Physical Review Letters **88**, 126801 (2002).
- [Lukashenko08] A. Lukashenko and A. V. Ustinov. *Improved powder filters for qubit measurements*. Review of Scientific Instruments **79**, 014701 (2008).
- [Mann03] D. Mann, A. Javey, J. Kong, Q. Wang, and H. J. Dai. *Balistic transport in metallic nanotubes with reliable Pd ohmic contacts*. Nano Letters **3**, 1541 (2003).
- [Martel98] R. Martel, T. Schmidt, H. R. Shea, T. Hertel, and P. Avouris. *Single- and multi-wall carbon nanotube field-effect transistors*. Applied Physics Letters **73**, 2447 (1998).
- [Mason04] N. Mason, M. J. Biercuk, and C. M. Marcus. *Local Gate Control of a Carbon Nanotube Double Quantum Dot*. Science **303**, 655 (2004).
- [Maultzsch05] J. Maultzsch, H. Telg, S. Reich, and C. Thomsen. *Radial breathing mode of single-walled carbon nanotubes: Optical transition energies and chiral-index assignment*. Physical Review B **72**, 205438 (2005).
- [Meyer05] J. C. Meyer, M. Paillet, T. Michel, A. Moreac, A. Neumann, G. S. Duesberg, S. Roth, and J. L. Sauvajol. *Raman modes of*

## BIBLIOGRAPHY

---

- index-identified freestanding single-walled carbon nanotubes*. Physical Review Letters **95**, 217401 (2005).
- [Michel09] T. Michel, M. Paillet, D. Nakabayashi, M. Picher, V. Jourdain, J. C. Meyer, A. A. Zahab, and J.-L. Sauvajol. *Indexing of individual single-walled carbon nanotubes from Raman spectroscopy*. Physical Review B **80**, 245416 (2009).
- [Misewich03] J. A. Misewich, R. Martel, Ph. Avouris, J. C. Tsang, S. Heinze, and J. Tersoff. *Electrically Induced Optical Emission from a Carbon Nanotube FET*. Science **300**, 783 (2003).
- [Moisala03] A. Moisala, A. G. Nasibulin, and E. I. Kauppinen. *The role of metal nanoparticles in the catalytic production of single-walled carbon nanotubes - a review*. Journal of Physics - Condensed Matter **15**, S3011 (2003).
- [Nie97] S. M. Nie and S. R. Emery. *Probing single molecules and single nanoparticles by surface-enhanced Raman scattering*. Science **275**, 1102 (1997).
- [Nitzan03] A. Nitzan and M. A. Ratner. *Electron transport in molecular wire junctions*. Science **300**, 1384 (2003).
- [Notingher05] I. Notingher and A. Elfick. *Effect of sample and substrate electric properties on the electric field enhancement at the apex of SPM nanotips*. Journal of Physical Chemistry B **109**, 15699 (2005).
- [O'Connell04] M. J. O'Connell, S. Sivaram, and S. K. Doorn. *Near-infrared resonance Raman excitation profile studies of single-walled carbon nanotube intertube interactions: A direct comparison of bundled and individually dispersed HiPco nanotubes*. Physical Review B **69**, 235415 (2004).
- [Oreg00] Y. Oreg, K. Byczuk, and B. I. Halperin. *Spin Configurations of a Carbon Nanotube in a Nonuniform External Potential*. Physical Review Letters **85**, 365 (2000).
- [Oron-Carl05] M. Oron-Carl, F. Hennrich, M. M. Kappes, H. v. Löhneysen, and R. Krupke. *On the Electron-Phonon Coupling of Individual Single-Walled Carbon Nanotubes*. Nano Letters **5**, 1761 (2005).

- [Osorio07] E. A. Osorio, K. O'Neill, M. R. Wegewijs, N. Stuhr-Hansen, J. Paaske, T. Bjørnholm, and H. S. J. van der Zant. *Electronic Excitations of a Single Molecule Contacted in a Three-Terminal Configuration*. Nano Letters **7**, 3336 (2007).
- [Osorio10] E. A. Osorio, K. Moth-Poulsen, H. S. J. van der Zant, J. Paaske, P. Hedegård, K. Flensberg, J. Bendix, and T. Bjørnholm. *Electrical Manipulation of Spin States in a Single Electrostatically Gated Transition-Metal Complex*. Nano Letters **10**, 105 (2010).
- [Paillet06] M. Paillet, T. Michel, J. C. Meyer, V. N. Popov, L. Henrard, S. Roth, and J. L. Sauvajol. *Raman active phonons of identified semiconducting single-walled carbon nanotubes*. Physical Review Letters **96**, 257401 (2006).
- [Park99] H. Park, A. K. L. Lim, A. P. Alivisatos, J. Park, and P. L. McEuen. *Fabrication of metallic electrodes with nanometer separation by electromigration*. Applied Physics Letters **75**, 301 (1999).
- [Park02] J. Park, A. N. Pasupathy, J. I. Goldsmith, C. Chang, Y. Yaish, J. R. Petta, M. Rinkoski, J. P. Sethna, H. D. Abruna, P. L. McEuen, and D. C. Ralph. *Coulomb blockade and the Kondo effect in single-atom transistors*. Nature **417**, 722 (2002).
- [Peica10] N. Peica, C. Thomsen, and J. Maultzsch. *Tip-enhanced Raman scattering along a single wall carbon nanotubes bundle*. physica status solidi (b) - solid state physics **247**, 2818 (2010).
- [Petta01] J. R. Petta and D. C. Ralph. *Studies of Spin-Orbit Scattering in Noble-Metal Nanoparticles Using Energy-Level Tunneling Spectroscopy*. Physical Review Letters **87**, 266801 (2001).
- [Pichler01] T. Pichler, H. Kuzmany, H. Kataura, and Y. Achiba. *Metallic Polymers of C<sub>60</sub> Inside Single-Walled Carbon Nanotubes*. Physical Review Letters **87**, 267401 (2001).
- [Pimenta07] M. A. Pimenta, G. Dresselhaus, M. S. Dresselhaus, L. G. Cançado, A. Jorio, and R. Saito. *Studying disorder in graphite-based systems by Raman spectroscopy*. Physical Chemistry Chemical Physics **9**, 1276 (2007).

## BIBLIOGRAPHY

---

- [Piscanec07] S. Piscanec, M. Lazzeri, J. Robertson, A. C. Ferrari, and F. Mauri. *Optical phonons in carbon nanotubes: Kohn anomalies, Peierls distortions, and dynamic effects*. Physical Review B **75**, 035427 (2007).
- [Pobell96] Frank Pobell. *Matter and Methods at Low Temperatures*. Springer-Verlag, 2nd edition, (1996).
- [Ponomarenko08] L. A. Ponomarenko, F. Schedin, M. I. Katsnelson, R. Yang, E. W. Hill, K. S. Novoselov, and A. K. Geim. *Chaotic dirac billiard in graphene quantum dots*. Science **320**, 356 (2008).
- [Popov00] V. N. Popov, V. E. Van Doren, and M. Balkanski. *Elastic properties of single-walled carbon nanotubes*. Physical Review B **61**, 3078 (2000).
- [Popov04] V. N. Popov and L. Henrard. *Comparative study of the optical properties of single-walled carbon nanotubes within orthogonal and nonorthogonal tight-binding models*. Physical Review B **70**, 115407 (2004).
- [Quay07] C. H. L. Quay, J. Cumings, S. J. Gamble, A. Yazdani, H. Kataura, and D. Goldhaber-Gordon. *Transport properties of carbon nanotube  $C_{60}$  peapods*. Physical Review B **76**, 073404 (2007).
- [Ralph95] D. C. Ralph, C. T. Black, and M. Tinkham. *Spectroscopic Measurements of Discrete Electronic States in Single Metal Particles*. Physical Review Letters **74**, 3241 (1995).
- [Raman28] C. V. Raman. *A Change of Wave-length in Light Scattering*. Nature **121**, 619 (1928).
- [Reich02a] S. Reich, J. Maultzsch, C. Thomsen, and P. Ordejón. *Tight-binding description of graphene*. Physical Review B **66**, 035412 (2002).
- [Reich02b] S. Reich, C. Thomsen, and P. Ordejón. *Electronic band structure of isolated and bundled carbon nanotubes*. Physical Review B **65**, 155411 (2002).
- [Reich04] S. Reich, C. Thomsen, and J. Maultzsch. *Carbon nanotubes: basic concepts and physical properties*. Wiley-VCH, (2004).

- [Rintala09] J. Rintala, O. Herranen, A. Johansson, M. Ahlskog, and M. Pettersson. *Raman Spectroscopy and Low-Temperature Transport Measurements of Individual Single-Walled Carbon Nanotubes with Varying Thickness*. Journal of Physical Chemistry C **113**, 15398 (2009).
- [Roth06] R. M. Roth, N. C. Panoiu, M. M. Adams, R. M. Osgood, C. C. Neacsu, and M. B. Raschke. *Resonant-plasmon field enhancement from asymmetrically illuminated conical metallic-probe tips*. Optics Express **14**, 2921 (2006).
- [Sahoo05] S. Sahoo, T. Kontos, J. Furer, C. Hoffmann, M. Gräber, A. Cottet, and C. Schönenberger. *Electric field control of spin transport*. Nature Physics **1**, 99 (2005).
- [Saito98] R. Saito, T. Takeya, T. Kimura, G. Dresselhaus, and M. S. Dresselhaus. *Raman intensity of single-wall carbon nanotubes*. Physical Review B **57**, 4145 (1998).
- [Salvetat99] J.-P. Salvetat, G. A. D. Briggs, J.-M. Bonard, R. R. Bacsa, A. J. Kulik, Thomas Stöckli, N. A. Burnham, and L. Forró. *Elastic and Shear Moduli of Single-Walled Carbon Nanotube Ropes*. Physical Review Letters **82**, 944 (1999).
- [Sapmaz05] S. Sapmaz, P. Jarillo-Herrero, J. Kong, C. Dekker, L. P. Kouwenhoven, and H. S. J. van der Zant. *Electronic excitation spectrum of metallic carbon nanotubes*. Physical Review B **71**, 153402 (2005).
- [Sapmaz06a] S. Sapmaz, P. Jarillo-Herrero, Ya. M. Blanter, C. Dekker, and H. S. J. van der Zant. *Tunneling in Suspended Carbon Nanotubes Assisted by Longitudinal Phonons*. Physical Review Letters **96**, 026801 (2006).
- [Sapmaz06b] S. Sapmaz, C. Meyer, P. Beliczynski, P. Jarillo-Herrero, and L. P. Kouwenhoven. *Excited State Spectroscopy in Carbon Nanotube Double Quantum Dots*. Nano Letters **6**, 1350 (2006).
- [Sauvajol02] J. L. Sauvajol, E. Anglaret, S. Rols, and L. Alvarez. *Phonons in single wall carbon nanotube bundles*. Carbon **40**, 1697 (2002).
- [Shimada02] T. Shimada, T. Okazaki, R. Taniguchi, T. Sugai, H. Shinohara, K. Suenaga, Y. Ohno, S. Mizuno, S. Kishimoto, and T. Mizutani. *Ambipolar field-effect transistor behavior of*



## BIBLIOGRAPHY

---

- Gd@C-82 metallofullerene peapods*. Applied Physics Letters **81**, 4067 (2002).
- [Sloan00] J. Sloan, R. E. Dunin-Borkowski, J. L. Hutchison, K. S. Coleman, V. C. Williams, J. B. Claridge, A. P. E. York, C. G. Xu, S. R. Bailey, G. Brown, S. Friedrichs, and M. L. H. Green. *The size distribution, imaging and obstructing properties of C60 and higher fullerenes formed within arc-grown single walled carbon nanotubes*. Chemical Physics Letters **316**, 191 (2000).
- [Smerat11] Sebastian Smerat. *Ground state and dynamical properties of the finite Kondo lattice model and transport through carbon based nanodevices - a numerical study*. PhD thesis, Ludwig-Maximilians-Universität München, (2011).
- [Smith98] B. W. Smith, M. Monthieux, and D. E. Luzzi. *Encapsulated C60 in carbon nanotubes*. Nature **396**, 323 (1998).
- [Souza03] A. G. Souza, A. Jorio, G. G. Samsonidze, G. Dresselhaus, R. Saito, and M. S. Dresselhaus. *Raman spectroscopy for probing chemically/physically induced phenomena in carbon nanotubes*. Nanotechnology **14**, 1130 (2003).
- [Spudat08] C. Spudat, C. Meyer, and C. M. Schneider. *Oxidation induced shifts of Raman modes of carbon nanotubes*. physica status solidi (b) - solid state physics **245**, 2205 (2008).
- [Spudat09] C. Spudat, C. Meyer, K. Goss, and C. M. Schneider. *Peapod synthesis depending on the number of nanotube sidewalls*. physica status solidi (b) - solid state physics **246**, 2498 (2009).
- [Spudat10] C. Spudat, M. Mueller, L. Houben, J. Maultzsch, K. Goss, C. Thomsen, C. M. Schneider, and C. Meyer. *Observation of Breathing-like Modes in an Individual Multiwalled Carbon Nanotube*. Nano Letters **10**, 4470 (2010).
- [Stampfer08] C. Stampfer, E. Schurtenberger, F. Molitor, J. Guettinger, T. Ihn, and K. Ensslin. *Tunable graphene single electron transistor*. Nano Letters **8**, 2378 (2008).
- [Talapatra06] S. Talapatra, S. Kar, S. K. Pal, R. Vajtai, L. Ci, P. Victor, M. M. Shaijumon, S. Kaur, O. Nalamasu, and P. M. Ajayan. *Direct growth of aligned carbon nanotubes on bulk metals*. Nature Nanotechnology **1**, 112 (2006).

- [Tans97] S. J. Tans, M. H. Devoret, H. J. Dai, A. Thess, R. E. Smalley, L. J. Geerligs, and C. Dekker. *Individual single-wall carbon nanotubes as quantum wires*. Nature **386**, 474 (1997).
- [Tans98a] S. J. Tans, M. H. Devoret, R. J. A. Groeneveld, and C. Dekker. *Electron-electron correlations in carbon nanotubes*. Nature **394**, 761 (1998).
- [Tans98b] S. J. Tans, A. R. M. Verschueren, and C. Dekker. *Room-temperature transistor based on a single carbon nanotube*. Nature **393**, 49 (1998).
- [Tao06] N. J. Tao. *Electron transport in molecular junctions*. Nature Nanotechnology **1**, 173 (2006).
- [Tarucha96] S. Tarucha, D. G. Austing, T. Honda, R. J. van der Hage, and L. P. Kouwenhoven. *Shell Filling and Spin Effects in a Few Electron Quantum Dot*. Physical Review Letters **77**, 3613 (1996).
- [Telg04] H. Telg, J. Maultzsch, S. Reich, F. Hennrich, and C. Thomsen. *Chirality Distribution and Transition Energies of Carbon Nanotubes*. Physical Review Letters **93**, 177401 (2004).
- [Telg05] H. Telg, J. Maultzsch, S. Reich, and C. Thomsen. *Chirality dependence of the high-energy Raman modes in carbon nanotubes*. In *Electronic Properties of Novel Nanostructures*, volume 786 of *AIP*, page 162, (2005).
- [Telg09] Hagen Telg. *Raman studies on individual nanotubes and nanotube ensembles - vibrational properties and scattering efficiencies*. PhD thesis, Technische Universität Berlin, (2009).
- [Thess96] A. Thess, R. Lee, P. Nikolaev, H. J. Dai, P. Petit, J. Robert, C. H. Xu, Y. H. Lee, S. G. Kim, A. G. Rinzler, D. T. Colbert, G. E. Scuseria, D. Tomanek, J. E. Fischer, and R. E. Smalley. *Crystalline ropes of metallic carbon nanotubes*. Science **273**, 483 (1996).
- [Thomsen00] C. Thomsen and S. Reich. *Double Resonant Raman Scattering in Graphite*. Physical Review Letters **85**, 5214 (2000).
- [Thomsen07] C. Thomsen and S. Reich. *Topics in Applied Physics (108): Light Scattering in Solid IX*, chapter Raman Scattering in Carbon Nanotubes, pages 115–232. Springer-Verlag, (2007).

## BIBLIOGRAPHY

---

- [Tuinstra70] F. Tuinstra and J. L. Koenig. *Raman spectrum of graphite*. Journal of Chemical Physics **53**, 1126 (1970).
- [Utko06] P. Utko, J. Nygård, M. Monthieux, and L. Noe. *Sub-Kelvin transport spectroscopy of fullerene peapod quantum dots*. Applied Physics Letters **89**, 233118 (2006).
- [van Houten92] H. van Houten, C. W. J. Beenakker, and A. A. M. Staring. *Single Charge Tunneling*, volume 294 of *NATO Advanced Studies Institutes, Series B: Physics*, chapter Coulomb-Blockade Oscillations in Semiconductor Nanostructures. Plenum, New York, (1992).
- [Wallace47] P. R. Wallace. *The Band Theory of Graphite*. Physical Review **71**, 622 (1947).
- [Walters99] D. A. Walters, L. M. Ericson, M. J. Casavant, J. Liu, D. T. Colbert, K. A. Smith, and R. E. Smalley. *Elastic strain of freely suspended single-wall carbon nanotube ropes*. Applied Physics Letters **74**, 3803 (1999).
- [Wang06] F. Wang, M. Y. Sfeir, L. Huang, X. M. H. Huang, Y. Wu, J. Kim, J. Hone, S. O'Brien, L. E. Brus, and T. F. Heinz. *Interactions between Individual Carbon Nanotubes Studied by Rayleigh Scattering Spectroscopy*. Physical Review Letters **96**, 167401 (2006).
- [Wei01] B. Q. Wei, R. Vajtai, and P. M. Ajayan. *Reliability and current carrying capacity of carbon nanotubes*. Applied Physics Letters **79**, 1172 (2001).
- [Wildöer98] J. W. G. Wildöer, L. C. Venema, A. G. Rinzler, R. E. Smalley, and C. Dekker. *Electronic structure of atomically resolved carbon nanotubes*. Nature **391**, 59 (1998).
- [Wu07] Y. Wu, J. Maultzsch, E. Knoesel, B. Chandra, M. Huang, M. Y. Sfeir, L. E. Brus, J. Hone, and T. F. Heinz. *Variable Electron-Phonon Coupling in Isolated Metallic Carbon Nanotubes Observed by Raman Scattering*. Physical Review Letters **99**, 027402 (2007).
- [Yang99] L. Yang, M. P. Anantram, J. Han, and J. P. Lu. *Band-gap change of carbon nanotubes: Effect of small uniaxial and torsional strain*. Physical Review B **60**, 13874 (1999).

- [Yano06] T. Yano, P. Verma, S. Kawata, and Y. Inouye. *Diameter-selective near-field Raman analysis and imaging of isolated carbon nanotube bundles*. Applied Physics Letters **88**, 093125 (2006).
- [Yao00] Z. Yao, C. L. Kane, and C. Dekker. *High-Field Electrical Transport in Single-Wall Carbon Nanotubes*. Physical Review Letters **84**, 2941 (2000).
- [Yokoyama07] D. Yokoyama, T. Iwasaki, T. Yoshida, H. Kawarada, S. Sato, T. Hyakushima, M. Nihei, and Y. Awano. *Low temperature grown carbon nanotube interconnects using inner shells by chemical mechanical polishing*. Applied Physics Letters **91**, 263101 (2007).
- [Zhang00] Y. Zhang, N. W. Franklin, R. J. Chen, and H. J. Dai. *Metal coating on suspended carbon nanotubes and its implication to metal-tube interaction*. Chemical Physics Letters **331**, 35 (2000).
- [Zou07] Yo. Zou, B. Liu, M. Yao, Y. Hou, L. Wang, S. Yu, P. Wang, B. Li, B. Zou, T. Cui, G. Zou, T. Wågberg, and B. Sundqvist. *Raman spectroscopy study of carbon nanotube peapods excited by near-IR laser under high pressure*. Physical Review B **76**, 195417 (2007).



# List of Figures

2.1	Graphene and carbon nanotube lattice. . . . .	6
2.2	TEM image of multiwalled nanotube and carbon nanotube ropes. . .	7
2.3	Electronic band structure of graphene. . . . .	8
2.4	Band structure of a (7, 7) and a (8, 0) nanotube. . . . .	11
2.5	Density of states for a (7, 7) nanotube. . . . .	12
2.6	Calculated Kataura plot: Transition energy vs tube diameter. . . .	13
2.7	Phonon band structure of carbon nanotubes. . . . .	15
2.8	Resonant Raman spectroscopy. . . . .	17
2.9	Carbon nanotube Raman spectrum. . . . .	18
2.10	Radial breathing mode frequency as function of nanotube diameter. .	19
2.11	High energy modes of a metallic and a semiconducting nanotube. . .	21
2.12	Diameter dependence of the high energy mode. . . . .	22
3.1	Tip-enhanced Raman spectroscopy schematic. . . . .	27
3.2	Schematic three-terminal carbon nanotube device. . . . .	28
3.3	AFM image of CVD-grown carbon nanotubes and schematic EBL process. . . . .	30
3.4	Sample pattern. . . . .	31
3.5	AFM image of a contacted CNT and photograph of a wire-bonded sample. . . . .	32
3.6	AFM images of a CNT rope device for TERS. . . . .	33
3.7	Near-field and far-field Raman spectra of a CNT rope device. . . .	34
3.8	Radial breathing modes of the CNT rope device. . . . .	35
3.9	Comparison of CNT diameters taking different literature values. . . .	36
3.10	High energy modes of the CNT rope device. . . . .	37
3.11	Diameter dependence of the HEM for metallic and semiconducting CNTs. . . . .	38
3.12	Kataura plot including experimental data points. . . . .	40
3.13	Evolution of Raman modes with changing tip position. . . . .	43
4.1	Circuit diagram of a quantum dot. . . . .	49
4.2	Schematic of Coulomb oscillations. . . . .	50

## LIST OF FIGURES

---

4.3	Schematic of non-linear transport with a high bias voltage. . . . .	52
4.4	Schematic stability diagram of a quantum dot. . . . .	53
4.5	Excited state spectroscopy with a $dI/dV$ stability diagram. . . . .	54
4.6	Characteristics of carbon nanotube quantum dots. . . . .	55
4.7	Model of two interacting parallel quantum dots. . . . .	58
4.8	Circuit diagram of interacting parallel quantum dots. . . . .	59
4.9	Calculated stability diagram of two interacting parallel quantum dots. . . . .	61
4.10	Sketch on the differential gating effect of two parallel quantum dots. . . . .	62
5.1	$^3\text{He}$ - $^4\text{He}$ phase diagram and principle of a dilution refrigerator. . . . .	66
5.2	Measurement electronics and filtering in the dilution refrigerator. . . . .	68
5.3	Noise level for the dot current before and after improved electronic setup. . . . .	69
5.4	Electron temperature extracted from a Coulomb peak. . . . .	70
5.5	Attenuation of Cu and Ag metal powder filters. . . . .	71
6.1	Differential conductance measured for a carbon nanotube rope device. . . . .	74
6.2	Differential conductance plot with four diamonds and secondary resonances. . . . .	76
6.3	High resolution differential conductance plot. . . . .	77
6.4	Construction of the side dot diamonds. . . . .	79
6.5	Stability diagrams of all secondary resonances and resulting side dot diamonds. . . . .	81
6.6	Measurement and calculation of a shifted main dot diamond edge. . . . .	84
6.7	Differential conductance plot with several shifted diamond edges. . . . .	85
7.1	Anticrossings with changing sign of $t$ . . . . .	90
7.2	Anticrossing of side dot 6. . . . .	91
7.3	Differential conductance plot at $B = 10$ T. . . . .	92
7.4	Close-up of the anticrossings/crossings at $B = 10$ T. Schematics on non-hybridizing spin-split states. . . . .	93
7.5	Calculated stability diagram with spin-split states. . . . .	94
7.6	Spin configurations of the parallel quantum dots. . . . .	96
8.1	AFM image and transport measurement of nanotube devices with top gate structures. . . . .	99
A.1	Kataura plot including experimental data points with particular $(n, m)$ indicated. . . . .	103
A.2	Kataura plot including error of the RBM-determined diameters. . . . .	104

# List of Tables

3.1	Raman shifts, diameters and chiral indices for the nanotubes in the rope. . . . .	39
6.1	Coupling parameters and interaction properties of the parallel QDs. .	83
A.1	Reference list of the parameters for the RBM formula. . . . .	102
B.2	Process parameters for electron beam writing. . . . .	105





# List of Own Publications

(in chronological order)

## Papers

- M. Sing, G. Berner, **K. Goß**, A. Müller, A. Ruff, A. Wetscherek, S. Thiel, J. Mannhart, S. A. Pauli, C. W. Schneider, P. R. Willmott, M. Gorgoi, F. Schäfers, and R. Claessen  
"Profiling the Interface Electron Gas of LaAlO<sub>3</sub>/SrTiO<sub>3</sub> Heterostructures with Hard X-Ray Photoelectron Spectroscopy"  
*Physical Review Letters* **102**, 176805 (2009).
- **K. Goß**, A. Kamra, C. Spudat, C. Meyer, P. Kögerler, and C. M. Schneider  
"CVD growth of carbon nanotubes using molecular nanoclusters as catalyst"  
*physica status solidi (b)* **11-12**, 2494 (2009).
- C. Spudat, C. Meyer, **K. Goß**, and C. M. Schneider  
"Peapod synthesis depending on the number of nanotube sidewalls"  
*physica status solidi (b)* **11-12**, 2498 (2009).
- C. Spudat, M. Müller, L. Houben, J. Maultzsch, **K. Goß**, C. Thomsen, C. M. Schneider, and C. Meyer  
"Observation of Breathing-like Modes in an Individual Multiwalled Carbon Nanotube"  
*Nano Letters* **10** (11), 4470 (2010).
- M. Sing, S. Glawion, M. Schlachter, M. R. Scholz, **K. Goß**, J. Heidler, G. Berner, and R. Claessen  
"Photoemission of a Doped Mott Insulator: Spectral Weight Transfer and a Qualitative Mott-Hubbard Description"  
*Physical Review Letters* **106**, 056403 (2011).
- **K. Goß**, S. Smerat, M. Leijnse, M. R. Wegewijs, C. M. Schneider, and C. Meyer

#### LIST OF OWN PUBLICATIONS

---

- "Spin-dependent electronic hybridization in a rope of carbon nanotubes"  
*Physical Review B* **83**, 201403(R) (2011).
- **K. Goß**, N. Peica, C. Thomsen, J. Maultzsch, C. M. Schneider, and C. Meyer  
"Tip-enhanced Raman spectroscopy of a contacted carbon nanotube rope"  
submitted for publication, *arXiv:1105.4427* (2011).
  - R. Frielinghaus, **K. Goß**, S. Trellenkamp, L. Houben, C. M. Schneider, and C. Meyer  
"Comprehensive characterization of an individual carbon nanotube transport device"  
submitted for publication, *arXiv:1105.4244* (2011).

## Poster Contributions

- C. Spudat, **K. Goß**, C. Meyer, C. M. Schneider  
 "Carbon Nanotube Peapods for Spintronics"  
 International Workshop on Spin Phenomena in Reduced Dimension 24-26.09.2008,  
 Regensburg (Germany).
- **K. Goß**, A. Kamra, C. Spudat, C. Meyer, P. Kögerler, C. M. Schneider  
 "CVD Growth of Carbon Nanotubes Using Molecular Nanoclusters as Catalyst"  
 International Winterschool on Electronic Properties of Novel Materials, 07.-  
 14.03.2009, Kirchberg (Austria).
- **K. Goß**, A. Kamra, C. Spudat, C. Meyer, P. Kögerler, C. M. Schneider  
 "CVD Growth of Carbon Nanotubes Using Molecular Nanoclusters as Catalyst"  
 Frühjahrstagung SKM 2009 der DPG in Dresden (Germany).
- C. Spudat, C. Meyer, **K. Goß**, M. Müller, C. Thomsen, C. M. Schneider  
 "Characterization of On-Chip Filling of CVD-grown Carbon Nanotubes"  
 International Winterschool on Electronic Properties of Novel Materials (IWEPNM)  
 2009, Kirchberg (Austria).
- S. Wegscheider, C. Spudat, **K. Goß**, C. Meyer, C. M. Schneider  
 "Characterization of carbon nanotubes by correlation of electron microscopy  
 and Raman spectroscopy"  
 JARA-FIT Science Days 2009, Schleiden (Germany).
- C. Morgan, **K. Goß**, C. Meyer, C. M. Schneider  
 "CNT-based devices for transport measurements and characterization"  
 16th International Winterschool on New Developments in Solid State Physics:  
 Low Dimensional Systems, 2010, Mauterndorf (Austria).
- **K. Goß**, C. Meyer, M. R. Wegewijs, S. Smerat, C. M. Schneider  
 "Competing transport channels of quantum dots within a carbon nanotube  
 rope"  
 International Winterschool on Electronic Properties of Novel Materials, 06.-  
 13.03.2010, Kirchberg (Austria).
- C. Meyer, C. Spudat, M. Müller, L. Houben, **K. Goß**, S. Wegscheider, J. Maultzsch,  
 C. Thomsen, C. M. Schneider  
 "Low-frequency phonon coupling in an individual multi-walled carbon nano-  
 tube"

#### LIST OF OWN PUBLICATIONS

---

- International Winterschool on Electronic Properties of Novel Materials, 06.-13.03.2010, Kirchberg (Austria).
- **K. Goß**, S. Smerat, C. Meyer, M. R. Wegewijs, C. M. Schneider  
"Competing transport channels of quantum dots within a carbon nanotube rope"  
School and Conference on Spin-based quantum information processing, 16.-20.8.2010, Konstanz (Germany).
  - **K. Goß**, S. Smerat, M. Leijnse, M. R. Wegewijs, C. M. Schneider, C. Meyer  
"Spin dependent electronic hybridization between carbon nanotube quantum dots"  
Nanoelectronic Days 2010, 4.-7.10.2010, Aachen (Germany).
  - P. Weber, **K. Goß**, N. Peica, C. Thomsen, J. Maultzsch, S. Trellenkamp, J. Schubert, C. Stampfer, C. Meyer, C. M. Schneider  
"Correlation of quantum transport and tip-enhanced Raman spectroscopy on carbon nanotubes"  
Nanoelectronic Days 2010, 4.-7.10.2010, Aachen (Germany).
  - R. Frielinghaus, **K. Goß**, C. Spudat, L. Houben, C. Morgan, S. Trellenkamp, M. Müller, C. Thomsen, C. Meyer, C. M. Schneider  
"Correlating different characterization methods on individual carbon nanotubes"  
Nanoelectronic Days 2010, 4.-7.10.2010, Aachen (Germany).
  - **K. Goß**, N. Peica, S. Smerat, M. Leijnse, M. R. Wegewijs, C. Thomsen, J. Maultzsch, C. M. Schneider, C. Meyer  
"Correlation of quantum transport and tip-enhanced Raman spectroscopy on carbon nanotubes"  
International Winterschool on Electronic Properties of Novel Materials, 2011, Kirchberg (Austria).
  - P. Weber, S. Engels, **K. Goß**, C. M. Schneider, C. Meyer, C. Stampfer  
"Carbon nanotube quantum dots with graphene leads"  
International Winterschool on Electronic Properties of Novel Materials, 2011, Kirchberg (Austria).
  - R. Frielinghaus, **K. Goß**, C. Spudat, L. Houben, M. Müller, C. Thomsen, S. Trellenkamp, C. Meyer, C. M. Schneider  
"Correlating different characterization methods on individual carbon nanotubes"  
International Winterschool on Electronic Properties of Novel Materials, 2011, Kirchberg (Austria).

## Talks

- "CVD Growth of Carbon Nanotubes Using Different Types of Catalyst"  
Deutsche Physikerinnentagung, 2008, Münster
- "Single Electron Tunneling in a Carbon Nanotube Quantum Dot"  
Deutsche Physikerinnentagung, 2009, Frankfurt
- "Competing carbon nanotube quantum dots with different screening properties"  
2010 Frühjahrstagung SKM der DPG in Regensburg
- "Quantum transport and tip-enhanced Raman spectroscopy on carbon nanotubes"  
2010, seminar talk at the University of Regensburg, AG Prof. Dr. S. D. Ganichev, together with Graduiertenkolleg GRK 1570 (Electronic Properties of Carbon Based Nanostructures)
- "Correlation of quantum transport and tip-enhanced Raman spectroscopy on carbon nanotubes"  
2011 Frühjahrstagung SKM der DPG in Dresden



# Acknowledgements

There are many people who contributed in one way or the other to this thesis and accompanied me on the way towards the thesis during the last three years.

I acknowledge **Prof. Dr. Claus M. Schneider** for providing the possibility to do my PhD studies at his institute, the PGI-6, and forgiving me, that I did not turn to photoemission studies but rather stayed with the transport during the last three years.

I thank **Prof. Dr. Christoph Strunk** for accepting the enquiry of co-reporting on this thesis.

I am very grateful to **Dr. Carola Meyer**, the head of the nanotube group, for all her advice and support during the process of this work. It was a very valuable experience to work in a young and strongly growing group. Moreover, it was great to experience the conference atmosphere at the IWEPM in Kirchberg each year.

It was always fun to work with my fellow PhD students in the nanotube group with whom I shared emotional situations of working or non-working experiments, lab equipment, samples and clean room processes. I thank **Dr. Christian Spudat** for establishing the CVD process and the AFM. I am grateful to **Cate Morgan** for sharing her knowledge about material sciences and the English grammar and most of all, for being an invaluable office mate and friend. To **Robert Frielinghaus** I am very grateful for joining in small experiments aside and I highly appreciate his friendship. I acknowledge the work of the diploma student, **Peter Weber**, who always was highly motivated. Additionally, I want to thank all the **colleagues and PhD students** from our institute for the enjoyable time during everyday-work at the institute, but also at the excursions and on Spiekeroog.

I am very grateful to the Kin-Eq group, **Dr. Sebastian Smerat**, **Prof. Dr. Maarten R. Wegewijs**, **Dr. Martin Leijnse**, who never got tired of explaining me the details of their calculations. I am especially grateful to Sebastian for sitting



## ACKNOWLEDGEMENTS

---

in front of the plots together and discussing for hours and hours.

I acknowledge the collaboration with the Raman group at the TU Berlin. Here, I want to especially thank **Dr. Niculina Peica, Prof. Dr. Janina Maultzsch, Prof. Dr. Christian Thomsen and Dr. Matthias Müller**, for sharing their Raman expertise and equipment.

I acknowledge **Prof. Dr. Thomas Schäpers** for welcoming me in his lab and providing necessary equipment. Nothing would be running in the magnet lab, if there was not **Herbert Kertz**. I thank him very much for the patience not only with overpressured cryostats and warmed Helium cans, but also during leakage hunts and for winding hundreds of meters of wire onto epoxy rods. Also, I thank him for subletting his office to me during the writing time. I am very grateful to **Dr. Sergio Estévez Hernández** for introducing the dilution fridge and its peculiarities to me.

I thank **Heinz Pfeifer, Jürgen Lauer and Norbert Schnitzler** for their assistance concerning the electronic setup and the computer programming and their help when I "just quickly" needed something.

I thank **Dr. Stefan Trellenkamp** for e-beam writing and his extraordinarily organized system of files and in handling samples. I am grateful to **Christoph Krause and Hans Wingens** for metal evaporation, **Dr. Jürgen Schubert** for pulsed laser deposition and **Thomas Jansen** for molecular beam epitaxy.

I acknowledge the staff from the IFF-cleanroom, especially **Holger John and René Borowski** for sharing their experience in sample processing. Additionally, I thank **Dr. Lothar Houben** for his work at the transmission electron microscope.

At last I want to thank my **family and friends** for their companionship, support and friendship.

# Curriculum Vitae

## Personal Data

Karin Goß  
born 13.03.1983 in Straubing  
german

## Education

09/1993 – 06/2002  
06/2002

LUDWIGSGYMNASIUM STRAUBING  
Abitur

10/2002 – 05/2008  
05/2008

JULIUS-MAXIMILIANS-UNIVERSITÄT WÜRZBURG  
Diplom Physik  
Supervisor:  
Prof. Dr. R. Claessen, Experimentelle Physik IV

09/2005 – 07/2006  
07/2006

HERIOT-WATT UNIVERSITY EDINBURGH  
Master of Physics in Physical Science

since 07/2008

PETER GRÜNBERG INSTITUT  
FORSCHUNGSZENTRUM JÜLICH  
Ph.D. in physics  
Supervisor:  
Prof. Dr. C. M. Schneider

## Work Experience

07/2005 – 09/2005

NEUE MATERIALIEN WÜRZBURG GMBH  
Internship on electrorheological fluids

Jülich, June 29th 2011



1. **Soft Matter**  
From Synthetic to Biological Materials  
Lecture manuscripts of the 39th IFF Spring School March 3 – 14, 2008  
Jülich, Germany  
edited by J.K.G. Dhont, G. Gompper, G. Nägele, D. Richter, R.G. Winkler (2008),  
c. 1000 pages  
ISBN: 978-3-89336-517-3
2. **Structural analysis of diblock copolymer nanotemplates using grazing incidence scattering**  
by D. Korolkov (2008), III, 167 pages  
ISBN: 978-3-89336-522-7
3. **Thermal Nonequilibrium**  
Thermal forces in fluid mixtures  
Lecture Notes of the 8th International Meeting on Thermodiffusion,  
9 – 13 June 2008, Bonn, Germany  
edited by S. Wiegand, W. Köhler (2008), 300 pages  
ISBN: 978-3-89336-523-4
4. **Synthesis of CMR manganites and ordering phenomena in complex transition metal oxides**  
by H. Li (2008), IV, 176 pages  
ISBN: 978-3-89336-527-2
5. **Neutron Scattering**  
Lectures of the JCNS Laboratory Course held at the Forschungszentrum Jülich  
and the research reactor FRM II of TU Munich  
edited by R. Zorn, Th. Brückel, D. Richter (2008), ca. 500 pages  
ISBN: 978-3-89336-532-6
6. **Ultrafast Magnetization Dynamics**  
by S. Woodford (2008), 130 pages  
ISBN: 978-3-89336-536-4
7. **Role of Surface Roughness in Tribology: from Atomic to Macroscopic Scale**  
by C. Yang (2008), VII, 166 pages  
ISBN: 978-3-89336-537-1
8. **Strahl- und Spindynamik von Hadronenstrahlen in Mittelenergie-Ringbeschleunigern**  
von A. Lehrach (2008), II, 171 Seiten  
ISBN: 978-3-89336-548-7
9. **Phase Behaviour of Proteins and Colloid-Polymer Mixtures**  
by C. Gögelein (2008), II, 147 pages  
ISBN: 978-3-89336-555-5

10. **Spintronics – From GMR to Quantum Information**  
Lecture Notes of the 40<sup>th</sup> IFF Spring School March 9 – 20, 2009  
Jülich, Germany  
edited by St. Blügel, D. Bürgler, M. Morgenstern, C. M. Schneider,  
R. Waser (2009), c. 1000 pages  
ISBN: 978-3-89336-559-3
11. **ANKE / PAX Workshop on SPIN Physics**  
JINR, Dubna, Russia / June 22. – 26, 2009  
Org. Committee: A. Kacharava, V. Komarov, A. Kulikov, P. Lenisa, R. Rathmann,  
H. Ströher (2009), CD-ROM  
ISBN: 978-3-89336-586-9
12. **Entwicklung einer Nanotechnologie-Plattform für die Herstellung  
Crossbar-basierter Speicherarchitekturen**  
von M. Meier (2009), 135 Seiten  
ISBN: 978-3-89336-598-2
13. **Electronic Oxides –  
Correlation Phenomena, Exotic Phases and Novel Functionalities**  
Lecture Notes of the 41<sup>st</sup> IFF Spring School March 8 – 19, 2010  
Jülich, Germany  
edited by St. Blügel, T. Brückel, R. Waser, C.M. Schneider (2010), ca. 1000  
pages  
ISBN: 978-3-89336-609-5
14. **4<sup>th</sup> Georgian-German School and Workshop in Basic Science**  
Tbilisi, Georgia / May 3 – 7, 2010  
Org. Committee: E. Abrosimova, R. Botchorishvili, A. Kacharava, M. Nioradze,  
A. Prangishvili, H. Ströher (2010); CD-ROM  
ISBN: 978-3-89336-629-3
15. **Neutron Scattering**  
Lectures of the JCNS Laboratory Course held at Forschungszentrum Jülich and  
the research reactor FRM II of TU Munich  
edited by Th. Brückel, G. Heger, D. Richter, G. Roth and R. Zorn (2010),  
ca 350 pages  
ISBN: 978-3-89336-635-4
16. **Ab initio investigations of magnetic properties of ultrathin transition-metal  
films on 4d substrates**  
by A. Al-Zubi (2010), II, 143 pages  
ISBN: 978-3-89336-641-5
17. **Investigation of a metal-organic interface realization and understanding of  
a molecular switch**  
by O. Neucheva (2010), 134 pages  
ISBN: 978-3-89336-650-7

18. **Reine Spinströme in lateralen Spinventilen, *in situ* Erzeugung und Nachweis**  
von J. Mennig (2010), V, 95 Seiten  
ISBN: 978-3-89336-684-2
  
19. **Nanoimprint Lithographie als Methode zur chemischen Oberflächenstrukturierung für Anwendungen in der Bioelektronik**  
von S. Gilles (2010), II, 169 Seiten  
ISBN: 978-3-89336-686-6
  
20. **Macromolecular Systems in Soft- and Living-Matter**  
Lecture Notes of the 42<sup>nd</sup> IFF Spring School 2011 February 14 – 25, 2011  
Jülich, Germany  
edited by Jan K.G. Dhont, Gerhard Gompfer, Peter R.Lang, Dieter Richter, Marisol Ripoll, Dieter Willbold, Reiner Zorn (2011), ca. 1000 pages  
ISBN: 978-3-89336-688-0
  
21. **The spin structure of magnetic nanoparticles and in magnetic nanostructures**  
by S. Disch (2011), V, 342 pages  
ISBN: 978-3-89336-704-7
  
22. **Element-selective and time-resolved magnetic investigations in the extreme ultraviolet range**  
by P. Grychtol (2011), xii, 144 pages  
ISBN: 978-3-89336-706-1
  
23. **Spin-Transfer Torque Induced Dynamics of Magnetic Vortices in Nanopillars**  
by V. Sluka (2011), 121 pages  
ISBN: 978-3-89336-717-7
  
24. **Adsorption von Phthalocyaninen auf Edelmetalloberflächen**  
von I. Kröger (2011), vi, 206 Seiten  
ISBN: 978-3-89336-720-7
  
25. **Time-Resolved Single Molecule FRET Studies on Folding/Unfolding Transitions and on Functional Conformational Changes of Phosphoglycerate Kinase**  
by T. Rosenkranz (2011), III, 139 pages  
ISBN: 978-3-89336-721-4
  
26. **NMR solution structures of the MloK1 cyclic nucleotide-gated ion channel binding domain**  
by S. Schünke (2011), VI, (getr. pag.)  
ISBN: 978-3-89336-722-1

**27. Neutron Scattering**

Lectures of the JCNS Laboratory Course held at Forschungszentrum Jülich and the research reactor FRM II of TU Munich

edited by Th. Brückel, G. Heger, D. Richter, G. Roth and R. Zorn (2011),  
ca 350 pages

ISBN: 978-3-89336-725-2

**28. Neutron Scattering**

Experiment Manuals of the JCNS Laboratory Course held at Forschungszentrum Jülich and the research reactor FRM II of TU Munich

edited by Th. Brückel, G. Heger, D. Richter, G. Roth and R. Zorn (2011),  
ca. 180 pages

ISBN: 978-3-89336-726-9

**29. Silicon nanowire transistor arrays for biomolecular detection**

by X.T.Vu (2011), vii, 174 pages

ISBN: 978-3-89336-739-9

**30. Interactions between parallel carbon nanotube quantum dots**

by K. Goß (2011), viii, 139 pages

ISBN: 978-3-89336-740-5





